

**RECORDS OF NOW-EXTINCT SHORT-LIVED NUCLIDES IN
EARLY SOLAR SYSTEM OBJECTS: AN ION MICROPROBE
STUDY**

RITESH KUMAR MISHRA

Ph.D THESIS

DECEMBER 2009

PHYSICAL RESEARCH LABORATORY

NAVRANGPURA, AHMEDABAD, 380009

INDIA

**RECORDS OF NOW-EXTINCT SHORT- LIVED NUCLIDES IN
EARLY SOLAR SYSTEM OBJECTS: AN ION MICROPROBE
STUDY**

A Thesis submitted to

**GUJARAT UNIVERSITY,
AHMEDABAD-38009**

For the degree of
DOCTOR OF PHILOSOPHY IN PHYSICS
by
RITESH KUMAR MISHRA

**PHYSICAL RESEARCH LABORATORY,
NAVRANGPURA, AHMEDABAD, 380009
INDIA**

DECEMBER 2009

CERTIFICATE

I hereby declare that the work presented in this thesis is original and has not formed the basis for award of any degree or diploma by any University or Institution.

Author

Ritesh Kumar Mishra

Certified by:

Prof. J.N. Goswami (Thesis Supervisor)

Director,

Physical Research Laboratory,

Navrangpura, Ahmedabad, 380009

India

*Dedicated to my Loving &
Reverend Parents*

Contents

Acknowledgement

List of figures

List of tables

1 Introduction	1
1.1 Early Solar System and Short-Lived Nuclides	1
1.2 The Early Solar System Objects	2
1.2.1 Calcium Aluminium Rich Inclusions	2
1.2.2 Chondrules	3
1.3 Now-Extinct Short-Lived Nuclides (SLNs)	4
1.4 Sources of Now-Extinct Short-Lived Nuclides	7
1.5 Scope of the Present Study	9
2 Experimental Techniques	13
2.1 Electron Probe Micro Analyser (EPMA)	13
2.2 Secondary Ion Mass Spectrometer	15
2.2.1 Primary column	16
2.2.2 Secondary sector	19
2.2.3 Vacuum system	23
2.3 Ion microprobe Studies of Fe-Ni & Al-Mg isotope system	24
2.3.1 Fe-Ni isotope system	24
2.3.2 Al-Mg isotope system	29
3 Sample description	32
3.1 Semarkona	33
3.2 Lewis Hill 86134	34
3.3 Yamato Hill Y791324	34
3.4 EPMA Studies of UOC Chondrules	40
4 Results	47
4.1 Fe-Ni Isotope Systematics	47
4.1.1 Semarkona	47
4.1.2 LEW 86134 (L 3.0)	56

4.2 Al-Mg Isotope Systematics	58
4.2.1 Semarkona, LEW86134 & Y791324	58
5 Discussion	66
5.1 Solar System Initial Abundance of ^{60}Fe	66
5.2 Plausible Source(s) of ^{60}Fe	70
5.3 Stellar Nucleosynthesis and ^{60}Fe	72
5.3.1 Production of ^{60}Fe in Asymptotic Giant Branch (AGB) Star	72
5.3.2 Production of ^{60}Fe in Massive ($>10\text{M}_\odot$) Star	74
5.4 Sources of ^{26}Al	76
5.5 Stellar Source(s) of SLNs ^{60}Fe and ^{26}Al	77
5.6 Co-injection of ^{26}Al & ^{60}Fe into Solar System	80
5.7 Revision in Half-Life of ^{60}Fe	82
6 Summary and Future perspective	84
7 References	87

List of Figures:

Fig. 1.1 Evolution of Fe-Ni isotope system in solar system objects	6
Fig. 2.1 Schematic diagram of Electron Probe Micro Analyser (Cameca SX100) ...	14
Fig. 2.2 Schematic diagram of secondary ion mass spectrometer (Make Cameca ims-4f)	16
Fig. 2.3 Schematic diagram of Duoplasmatron	17
Fig. 2.4 Schematic diagram of the Caesium Source	18
Fig. 2.5 Schematic diagram of the primary sector which consisting of source and the primary column hosting lenses, apertures and deflectors	18
Fig. 2.6 Schematic diagram of the secondary sector which constituting the analyser and detectors	20
Fig. 2.7 Schematic diagram showing trajectory of secondary ions emitted from the surface	21
Fig. 2.8 High mass resolution spectrum at mass 57	25
Fig. 2.9 High mass resoultion spectra at mass 60	25
Fig. 2.10 High mass resoultion spectra at mass 62	26
Fig. 2.11 Instrument mass fractionation inferred from studies of Terrestrial standard over the entire duration of this study	29
Fig. 2.12 High mass resolution ($M/\Delta M \sim 4000$) spectra of ^{24}Mg , ^{25}Mg , ^{26}Mg , ^{27}Al .	31
Fig.3.1 Back scattered electron images of selected Semarkona chondrules. Red circles indicate regions analysed for Fe-Ni isotope systematics while green circles indicate regions analysed for Al-Mg isotope systematics in this study	36
Fig.3.2 Back scattered electron images of selected Semarkona chondrules. Red circles indicate regions analysed for Fe-Ni isotope systematics while green circles indicate regions analysed for Al-Mg isotope systematics in this study	37
Fig.3.3 Back scattered electron images of selected Semarkona chondrules. Red circles indicate regions analysed for Fe-Ni isotope systematics while green circles indicate regions analysed for Al-Mg isotope systematics in this study	38

Fig. 3.4 Back scattered electron images of selected chondrules from LEW 86134 and Y791324 analysed in the present study. Red and green circles indicate regions analysed for Fe-Ni and Al-Mg isotope systematics respectively	39
Fig. 3.5 Fe, Al, and Ca, X-ray elemental map for LEW 86314 Ch#36	40
Fig. 4.1 Three isotope Fe-Ni plots for Semarkona chondrule # 1 and #3. The inferred initial $^{60}\text{Fe}/^{56}\text{Fe}$ is also shown. The dotted line is the reference value of $^{60}\text{Ni}/^{62}\text{Ni}$. Error bars 2σ	50
Fig. 4.2 Three isotope Fe-Ni diagram for Semarkona chondrule # 18 and #20. The inferred initial $^{60}\text{Fe}/^{56}\text{Fe}$ is also shown. The dotted line is the reference value of $^{60}\text{Ni}/^{62}\text{Ni}$. Error bars 2σ	51
Fig. 4.3 Three isotope Fe-Ni diagram for Semarkona chondrule # 21 and # 29. The inferred initial $^{60}\text{Fe}/^{56}\text{Fe}$ is also shown. The dotted line is the reference value of $^{60}\text{Ni}/^{62}\text{Ni}$. Error bars 2σ	52
Fig. 4.4 Three isotope Fe-Ni diagram for Semarkona chondrule # 36 and LEW chondrule #36. The inferred initial $^{60}\text{Fe}/^{56}\text{Fe}$ is also shown. The dotted line is the reference value of $^{60}\text{Ni}/^{62}\text{Ni}$. Error bars 2σ	53
Fig. 4.5 Three isotope Fe-Ni diagram for Semarkona chondrule # 40 and LEW chondrule #37. The inferred initial $^{60}\text{Fe}/^{56}\text{Fe}$ is also shown. The dotted line is the reference value of $^{60}\text{Ni}/^{62}\text{Ni}$. Error bars 2σ	54
Fig. 4.6 Three isotope Fe-Ni diagram for Semarkona chondrule #8 and Y 791324 chondrule #6. The inferred initial $^{60}\text{Fe}/^{56}\text{Fe}$ is also shown. The dotted line is the reference value of $^{60}\text{Ni}/^{62}\text{Ni}$. Error bars 1σ	55
Fig. 4.7 Three isotope Al-Mg plots of Semarkona (LL 3.0) chondrules: Ch#1 top; Ch#3 bottom. Error bars 1σ	59
Fig. 4.8. Three isotope Al-Mg plots of Semarkona (LL 3.0) chondrules: Ch#8 top; Ch#18 bottom. Error bars 1σ	60
Fig. 4.9 Three isotope Al-Mg plots of Semarkona (LL 3.0) Ch 21A chondrule. Error bars 1σ	61
Fig. 4.10 Three isotope Al-Mg plot of Y791324 (L 3.0) chondrule #8. Error bars 1σ	63
Fig. 4.11 Count rate data from repeat runs on the given spot in Semarkona chondrules (#39, #21). The dynamic background monitored at mass 56.5 is also plotted in the upper panel	65
Fig. 5.1 Structure of 1M_\odot and 5M_\odot star during AGB phase	72

Fig. 5.2 ^{60}Fe yield (in solar mass) from model calculations for various stellar masses with solar metallicity. Results from Limongi & Chieffi are for two different stability criterion (\ast , \bullet) and mass loss rate (\bullet)	75
Fig. 5.3 Contribution from various shells to the total yield of ^{60}Fe for stars of solar metallicity	76
Fig. 5.4 Nucleosynthesis yields in various zones of a 25 M_\odot star based on one of the model (s25a31d) output from Rauscher et al. (2002)	78
Fig. 5.5 SSI abundances for a set of SLNs, including ^{26}Al and ^{60}Fe , based on a model yields from a 25M_\odot star (Rauscher et al. 2002) compared with observed values. A good fit is obtained for ^{26}Al , ^{60}Fe and a few other SLNs	79
Fig. 5.6 A plot of inferred $[^{60}\text{Fe}/^{56}\text{Fe}]_i$ vs. $[^{26}\text{Al}/^{27}\text{Al}]_i$ in UOC chondrules analyzed in this study. One data point from Tachibana et al. (2007) is also included. The expected correlation if ^{60}Fe and ^{26}Al were co-injected from the same source is shown for two SSI $^{60}\text{Fe}/^{56}\text{Fe}$ values of 10^{-6} and 5×10^{-7} . Time of formation of the chondrules, relative to CAIs is also shown in the top panel	81
Fig. 5.7 A plot of inferred $[^{60}\text{Fe}/^{56}\text{Fe}]_i$ vs. $[^{26}\text{Al}/^{27}\text{Al}]_i$ in UOC chondrules. Trend lines for two values of SSI $^{60}\text{Fe}/^{56}\text{Fe}$ are based on ^{60}Fe half-life of 2.6 Ma	83

List of Tables:

Table 1.1 Short-lived nuclides in the early solar system	5
Table 2.1 Stable isotopes of Fe and Ni and their abundances	24
Table 3.1 Chondrules selected for isotope studies	36
Table 3.2 Chemical composition of Semarkona (LL 3.0) chondrule	42
Table 3.3 Chemical composition of Semarkona (LL 3.0) chondrule	43
Table 3.4 Chemical composition of Semarkona (LL 3.0) chondrule	44
Table 3.5 Chemical composition of Semarkona (LL 3.0) chondrule	45
Table 3.6 Chemical composition of LEW 86134 (L 3.0) chondrule	45
Table 3.7 Chemical composition of LEW 86134 (L 3.0) chondrule	46
Table 3.8 Chemical composition of Y791324 (L 3.1) chondrule	46
Table 3.9 Chemical composition of Y791324 (L 3.1) chondrule	47
Table 4.1 Fe-Ni isotope data for chondrules from Semarkona (LL 3.0)	49
Table 4.2 Fe-Ni isotope data for chondrules from LEW 86134 (L 3.0)	57
Table 4.3 Fe-Ni isotope data for chondrules from Y791324 (L 3.1)	57
Table 4.4 Results obtained from Fe-Ni isotope systematics in UOCs chondrules ...	58
Table 4.5 Al-Mg isotope data for chondrules from Semarkona (LL 3.0)	59
Table 4.6 Al-Mg isotope data for analysed chondrules	63
Table 4.7 Al-Mg isotope data for chondrules from LEW 86134 (L 3.0)	64
Table 4.8 Al-Mg isotope data for chondrules from Y791324 (L 3.1)	64
Table 4.9 Data for Fe-Ni and Al-Mg isotope systematics for UOC chondrules	65
Table 5.1 Initial $^{60}\text{Fe}/^{56}\text{Fe}$ and $^{26}\text{Al}/^{27}\text{Al}$ at the time of formation of UOC chondrules and inferred SSI $^{60}\text{Fe}/^{56}\text{Fe}$	70

Acknowledgement:

The long walk down the aisle till the destination (Ph.D) could only be possible because of whole hearted encouragement and support from a few people. First and foremost my parents whose support, encouragement and love saw me through difficult times. I have been blessed to have such parents and this thesis is dedicated to them.

The scientific journey could not have been possible without the guidance and advices from Prof. J.N. Goswami, who not only had the patience to track the mistakes but forewarned of many pitfalls, which made all this come true in the shape it is today. The words of criticism and genuine pats kept me focussed on the job and I am in debt a lot of my scientific knowledge and understanding to him. I would also like to express my gratitude to all my teachers at various stages of life for their guidance.

Friends, remained unthanked all during this time while they kept the jive, peace and mirth in life. I thank them for their support, advice, and criticism.

Last but not the least, my family members, my Parents, Bhaiya, Bhabhi and my niece, my younger brother, who remained supportive for all these years and help me have peace with life, persistently giving, unmindful of my responsibility to them.

A few have made more difference to my life than others have, and my sincere and heartfelt thanks to them, long overdue in amount and time.

CHAPTER 1: INTRODUCTION

Our understanding of the origin and early evolution of the Solar system has increased significantly due to recent advances in both computational and experimental capabilities. Formation of a Sun like star associated with a planetary system is now considered as a coupled system. The solar system formed due to the collapse of a dense interstellar molecular cloud fragment about 4.6 billion years ago, that led to the formation of the proto-Sun at the centre and a protoplanetary disk surrounding it. The protoplanetary disk consisting of interstellar dust and gas gradually evolved under the influence of the gravitational and radiation fields of the proto-Sun that finally led to the formation of the solar system objects.

1.1 Early Solar System and Short-Lived Nuclides

The events and processes occurring during the early stages (first few tens of million years) of the birth of the solar system are responsible in determining the overall nature of the planetary objects and their general properties. Pristine records of events taking place during this era can be obtained from a study of mineralogy and petrography as well as elemental and isotopic compositions of early solar system objects that have not experienced secondary processing that could alter such records. Studies of stable isotope records provide information about the environment and processes, while studies of suitable radionuclides provide time scales of such events and processes. Absolute ages of the early solar system events can be obtained by studying records of the long-lived isotope systematics (e.g. ^{235}U - ^{207}Pb : $t_{1/2} = 704 \text{ Ma}$; ^{40}K - ^{40}Ar : $t_{1/2} = 1.3 \text{ Ga}$; ^{238}U - ^{206}Pb : $t_{1/2} = 4.47 \text{ Ga}$; ^{87}Rb - ^{87}Sr : $t_{1/2} = 48.6 \text{ Ga}$; ^{147}Sm - ^{143}Nd : $t_{1/2} = 106 \text{ Ga}$), in various early solar system objects. Amongst these, only studies of ^{206}Pb - ^{207}Pb systematics can provide time resolution of less than a million year under favourable conditions (Amelin 2006). The other long-lived isotope systematics, in general, provide time resolution at the level of ten million years or more that is not sufficient to demarcate events taking place in shorter (a few million years or less) time interval during the early history of the solar system.

The discovery of fossil records of the now-extinct Short-Lived Nuclide (SLN) ^{129}I , (half life = 15.7 Ma) in Richardton meteorite (Reynolds 1960; Jeffery & Reynolds 1961) was followed by continuing efforts over the last few decades that provided

conclusive evidence for the presence of close to a dozen such SLNs with half-life varying from 0.1 to 100 Ma, in early solar system objects. Studies of these SLNs have now made it possible to infer relative time scales of events in early solar system history with a time resolution of less than a million year (Bizzarro et al., 2005; Villeneuve et al., 2009). Study of records of SLNs is an active area of current research in meteoritics that led to the estimates of the duration of several important epochs during the evolution of the early solar system. These include, duration of formation of the first solar system solids, the Calcium-Aluminium-rich Inclusions (CAIs), the time interval between the formation of CAIs and the chondrules, an ubiquitous component in chondrites, as well as the duration of formation of chondrules and the differentiated meteorites (Amelin et al., 2002; Kleine et al., 2002; Yin et al., 2002; Kita et al., 2005; Thrane et al., 2006; Connelly et al., 2008). In addition, combining data from absolute dating, using long-lived radionuclides, and relative chronology based on SLNs, in various solar system objects, it is possible to delineate the evolutionary history of the solar system. The presently available data suggest that the formation of the first solar system solid, the CAIs, was complete within a short duration of less than 100,000 years (Amelin et al., 2002; Young et al., 2005; Thrane et al., 2006), the formation of chondrules started about a million year after the CAIs and continued for a few million years and the formation of some of the differentiated meteorites was also complete within a couple of million years (Kita et al., 2000; Kleine et al., 2002; Yin et al., 2002; Bizzarro et al., 2005; Thrane et al., 2006; Rudraswami & Goswami 2007; Kurahashi et al., 2008; Rudraswami et al., 2008; Hutcheon et al., 2009; Villeneuve et al., 2009).

1.2 The Early Solar System Objects

1.2.1 Calcium Aluminium rich Inclusions

The collapse of the protosolar cloud led to the formation of the proto-Sun at the centre that was surrounded by residual interstellar gas and dust. This gas and dust complex slowly settled to a disk around the proto-Sun, the so-called solar nebula, under the influence of solar gravitational field. The highly active proto-Sun radiated a large amount of energy and the temperature in the midplane of the nebular disk could have reached values >1500 K (Boss 1998; D'Alessio et al., 2005). Thus, the first solar system solids to form in such an environment are the refractory oxides of calcium,

aluminium, titanium and magnesium, having very high condensation temperatures (Grossman 1972; Grossman 1980). Such refractory phases were indeed identified in carbonaceous chondrites (Christophe Michel-Levy 1968) and they are termed as Calcium-Aluminum-rich Inclusions (CAIs). CAIs are irregular shaped objects of up to a few centimetres in size and are predominantly found in carbonaceous chondrites where they constitute up to a maximum 12% by volume (Scott & Krot 2005). They are, however, rare in ordinary, enstatite and other (K, R) types of chondrites. The CAIs are classified based on their mineral constituents and morphology and are non igneous (evaporative residues or gas-solid condensates) or igneous objects (possibly melted condensates) composed of refractory oxides and silicates. Variations in their primary mineral assemblages (spinel \pm Melilite \pm Anorthite \pm forsterite) form the basis of classification of CAIs into several types (Hutchison 2004; MacPherson et al., 2005). Many CAIs preserve nucleosynthetic stable isotope anomalies in O, Ca, Ti, Cr, Ni and several other elements, indicating incomplete homogenization of multiple stellar nucleosynthesis products introduced into the protosolar cloud during its lifetime. The mineralogical, chemical and isotopic data for the CAIs suggest that they formed by evaporation-condensation processes in high-temperature nebular region(s) at or above the condensation temperature of forsterite (>1400 K) under variable, but generally low total pressure ($<10^{-4}$ bar), and in the presence of isotopically (^{16}O) enriched gas, and mostly in a reduced environment (Scott & Krot 2005). CAIs host fossil records of a large number of SLNs and the initial abundances of SLNs in CAIs are also considered as the Solar System Initial (SSI) abundance as the half-lives of the SLNs are much longer than the inferred duration of formation of CAIs (MacPherson et al., 2005; Krot et al., 2009).

1.2.2 Chondrules

Chondrules are igneous, spherical objects, 0.01-10 mm in size, and are ubiquitous in chondritic meteorites (except CI) constituting 15-80% by volume in different chondrites (Scott & Krot 2005). They are composed of ferromagnesian olivine and pyroxene, Fe-Ni metal, sulphides, and glassy or microcrystalline mesostasis. Their ubiquity in chondritic meteorites suggests that their formation was a major event in the early history of the solar system. Chondrules are considered to be products of melting of pre-existing nebular solids, aggregates of fine-grained matrix like material and coarse grained components including fragments of CAIs, during high temperature

transient events in the nebula, followed by rapid cooling (Ciesla 2005). Chondrule precursors were heated at 10^4 - 10^6 K/h (Desch et al., 2005; Tachibana & Huss 2005), reached peak temperatures of 1650-1850 K, and cooled at 10-1000 K/h (Desch & Connolly 2002; Hewins et al., 2005; Hood et al., 2005). Studies of fossil records of the SLN ^{26}Al present in chondrules from unequilibrated ordinary chondrites and carbonaceous chondrites suggest that, chondrule formation was episodic and started \sim 1Ma after the formation of CAIs and continued for at least a million year or more (Kita et al., 2000; Huss et al., 2001; Rudraswami & Goswami 2007; Kurahashi et al., 2008; Rudraswami et al., 2008; Hutcheon et al., 2009; Villeneuve et al., 2009). Chondrules show significant variations in their texture, size and mineralogy. They are classified into two types, porphyritic and non-porphyritic, based on their texture and are further classified into type I and II based on FeO content ($>10\%$: type II) and into type A and B based on the abundance of the major mineral phase, olivine/pyroxene (>80 vol% pyroxene: type B), constituting the chondrule.

Most chondrules are devoid of large magnitude nucleosynthetic isotope anomalies seen in CAIs. They are depleted in ^{16}O ($\Delta^{17}\text{O} > -10\%$) relative to CAIs ($\Delta^{17}\text{O} > -40\%$) (Krot et al., 2006), and show small magnitude ($< 1\%/\text{amu}$) mass dependent isotopic fractionation effects (Davis et al., 2005). Formation of chondrules is proposed to have taken place in isotopically distinct regions, at lower ambient temperature (< 1000 K), under more oxidizing conditions, and at higher total pressure and/or dust/gas ratio than during formation of the CAIs (Scott & Krot 2005b; Cuzzi & Alexander 2006; Alexander et al., 2008).

1.3 Now-Extinct Short-Lived Nuclides (SLNs)

The former presence of now-extinct short-lived nuclides in early solar system objects is inferred from the observed excess in the abundance of their daughter nuclides. A list of now-extinct short-lived nuclides present in the early solar system along with their half lives, daughter products and inferred solar system initial abundance based on analyses of various early solar system objects are shown in Table 1.1.

A correlation between the observed excess in the daughter nuclide abundance with the abundance of the parent element provides a conclusive proof of in-situ decay of the SLN in the analyzed object and rules out preservation of fossil excess or

nucleosynthetic anomaly leading to the observed excess. As an example, the SLN ^{60}Fe , the nuclide of primary interest in this study, decays to ^{60}Ni with its characteristic

Table 1.1 Short-lived nuclides in the early solar system

Short-lived radionuclide	Half life (Ma)	Daughter nuclides	Initial abundance (w.r.t. Ref. isotope)	Analyzed objects
^{41}Ca	0.1	^{41}K	1.5×10^{-8} (^{40}Ca) ¹	CAIs
^{36}Cl	0.3	^{36}S , ^{36}Ar	$\sim 4 \times 10^{-6}$ (^{35}Cl) ²	CAIs, Chondrules
^{26}Al	0.72	^{26}Mg	5×10^{-5} (^{27}Al) ³	CAIs, Chondrules, Achondrites
^{60}Fe	1.5*	^{60}Ni	$(\sim 0.2-1) \times 10^{-6}$ (^{56}Fe) ⁴	Chondrites, Achondrites
^{10}Be	1.5	^{10}B	8.8×10^{-4} (^{9}Be) ⁵	CAIs
^{53}Mn	3.7	^{53}Cr	9×10^{-6} (^{55}Mn) ⁶	CAIs, Chondrules, Achondrites
^{107}Pd	6.5	^{107}Ag	6×10^{-5} (^{108}Pd) ⁷	Iron meteorites, Pallasites, Chondrites
^{182}Hf	9	^{182}W	10^{-4} (^{180}Hf) ⁸	CAIs, Planetary differentiates
^{129}I	15.7	^{129}Xe	10^{-4} (^{127}I) ⁹	Chondrites, Chondrule, Secondary minerals
^{92}Nb	36	^{92}Zr	10^{-4} (^{93}Nb) ¹⁰	Chondrites, Mesosiderites
^{244}Pu	82	Fission	7×10^{-3} (^{238}U) ¹¹	CAIs, Chondrites
^{146}Sm	103	^{142}Nd	9×10^{-4} (^{147}Sm) ¹²	Chondrites

¹Srinivasan et al., 1994, 1996; ²Murty et al., 1997; Lin et al., 2005; ³Lee et al., 1976, 1977; ⁴Shukolyukov and Lugmair, 1993; Mostefaoui et al., 2005; Tachibana et al., 2006; ⁵McKeegan et al., 2000; Chaussidon et al. 2006; ⁶Trinquier et al., 2008; Moynier et al. 2008; Nyquist et al. 2009; Brick and Allègre, 1985; ⁷Chen and Wasserburg, 1990; Schonbachler et al., 2008; ⁸Kleine et al., 2002; Yin et al., 2002; ⁹Jeffery and Reynold, 1961; ¹⁰Schönbächler et al., 2002; ¹¹Hudson et al., 1988; ¹²Lugmair et al., 1983.

half-life of 1.5 Ma*. If live ^{60}Fe was present in the early solar system, it will get incorporated into early solar system objects at the time of their formation along with the stable isotopes of iron. In-situ decay of ^{60}Fe in such objects (e.g., CAIs or chondrules) will lead to excess in ^{60}Ni . If such objects acted as a isotopically close system throughout their evolution, the present abundance of ^{60}Ni in the object,

* A recent report suggests that the half-life of ^{60}Fe be revised to 2.62 Ma (Rugel et al., 2009). We use the existing value here and consider the implications of the new value while discussing our results in Chapter-6.

designated as “(^{60}Ni)_{now}” in the following relations, can be written as:

$$(^{60}\text{Ni})_{\text{now}} = (^{60}\text{Ni})_{\text{initial}} + (^{60}\text{Fe})_{\text{initial}}$$

Considering stable isotopes of Fe and Ni that have no radiogenic progenitor (e.g. ^{56}Fe and ^{62}Ni), we can write:

$$(^{60}\text{Ni}/^{62}\text{Ni})_{\text{now}} = (^{60}\text{Ni}/^{62}\text{Ni})_{\text{initial}} + (^{60}\text{Fe})_{\text{initial}} / (^{62}\text{Ni})_{\text{now}}$$

$$(^{60}\text{Ni}/^{62}\text{Ni})_{\text{now}} = (^{60}\text{Ni}/^{62}\text{Ni})_{\text{initial}} + (^{60}\text{Fe}/^{56}\text{Fe})_{\text{initial}} \times (^{56}\text{Fe}/^{62}\text{Ni})_{\text{now}}$$

where the term “initial” refers to the abundance at the time of formation of the analyzed object. Since the ratio of isotope abundance marked as “now” can be obtained from laboratory measurements, the “initial” value of ($^{60}\text{Fe}/^{56}\text{Fe}$) at the time of formation of the early solar system object can be inferred using the above linear

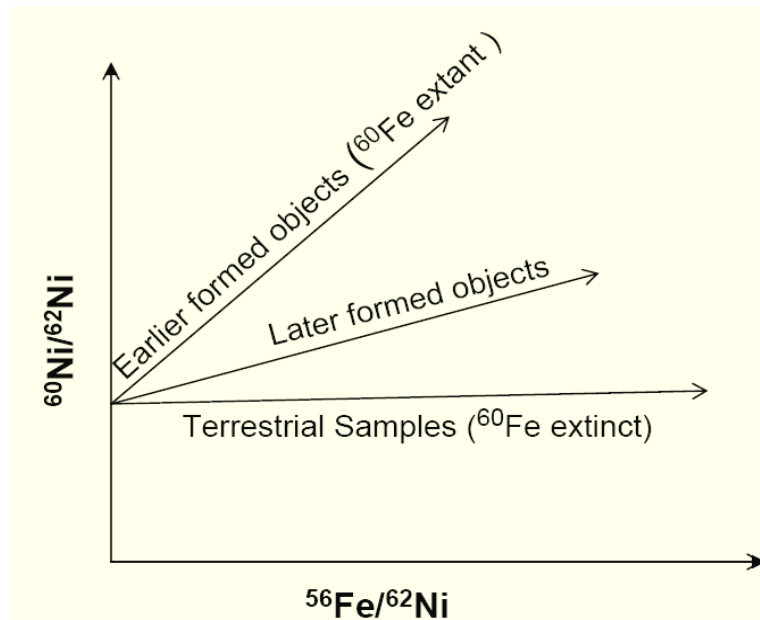


Fig. 1.1 Evolution of Fe-Ni isotope system in solar system objects

relation if one analyzes phases with varying ($^{56}\text{Fe}/^{62}\text{Ni}$) ratio present in the object. A plot of measured $^{60}\text{Ni}/^{62}\text{Ni}$ ratio vs. $^{56}\text{Fe}/^{62}\text{Ni}$ ratio for such an object will yield a straight line, often termed as an isochron, whose slope provides the value of initial ($^{60}\text{Fe}/^{56}\text{Fe}$) and the intercept initial ($^{60}\text{Ni}/^{62}\text{Ni}$) at the time of its formation. Objects that formed after ^{60}Fe became extinct (e.g. late forming solar system objects and terrestrial samples) will be devoid of ^{60}Ni excess and $^{60}\text{Ni}/^{62}\text{Ni}$ ratios will remain constant and

plot along the horizontal arrow (Fig 1.1). Early solar system objects in which ^{60}Fe was extant at the time of their formation will define correlation lines in this diagram with different slopes, the higher the slope (higher initial $^{60}\text{Fe}/^{56}\text{Fe}$), earlier the age of formation. Thus, the SLNs can serve as high-resolution relative chronometer for objects formed during the early evolution of the solar system. This approach is strictly valid only if the analyzed early solar system objects behaved as “close” system with no secondary events affecting the isotope records since the time of formation of the objects. Another intrinsic assumption in this approach is that the now-extinct SLNs were uniformly distributed in the early solar system in the region of formation of the analysed objects. Experimental data for individual SLNs (e.g., ^{26}Al) support this assumption (Thrane et al., 2006; Villeneuve et al., 2009). In addition, consistency between relative chronology, based on studies of records of now-extinct short-lived nuclides, and that obtained from absolute dating, using long-lived nuclides, in various early solar system objects support the validity of this assumption (Nyquist et al., 2009).

Studies of fossil records of SLNs in CAIs, chondrules and differentiated meteorites have provided new insights for understanding the origin and early evolution of the solar system. It is now believed that most of the SLNs were produced in a stellar source and injected into the protosolar cloud and this injection process itself could have triggered the collapse of the protosolar cloud leading to the formation of the solar system (Cameron & Truran 1977; Boss & Vanhala 2000; Goswami et al., 2005; Boss et al., 2008; Ouellette et al., 2009). However, alternate views that many of the SLNs could be products of interactions of high fluence of solar energetic particles from an active early Sun interacting with gas and dust present in the solar nebula have also been proposed (Shu et al., 1996; Shu et al., 1997; Lee et al., 1998; Leya et al., 2003; Chaussidon & Gounelle 2006).

1.4 Sources of Now-Extinct Short-Lived Nuclides

All elements and their isotopes with atomic number ≥ 6 (carbon onward) are synthesized primarily in stars during energy generation processes through nuclear reactions during its lifetime, and also during highly energetic sporadic and often catastrophic events towards the end of their lives. Both stable and radioactive nuclides are produced during stellar nucleosynthesis (Clayton 1983).

Apart from stellar production, spallation reactions induced by energetic cosmic rays of galactic or solar origin, generally referred to as Galactic Cosmic Rays (GCR) and Solar Energetic Particles (SEP), interacting with gas and dust present in the local interstellar space or in the solar nebula, respectively, can also produce stable and radioactive nuclides. GCR spallation reactions are primarily responsible for the production of Li, Be, B isotopes except for ^7Li , for which there is some contribution from primordial nucleosynthesis (Reeves 1994).

The now-extinct SLNs present in the early solar system may have two plausible sources:

- I. Stellar source(s)
- II. Energetic particle interactions with the gas and dust present in the protosolar cloud or in the solar nebula

Some of the SLNs can be uniquely identified with a specific source. For example, ^{60}Fe is considered as a distinct product of stellar nucleosynthesis as significant production by energetic particle reactions can be ruled out in the absence of abundant target nuclides and also because of its highly neutron-rich character. On the other hand, ^{10}Be is considered as a product of cosmic ray spallation reactions as it is not an end product during stellar nucleosynthesis. Several other short-lived nuclides (e.g. ^{41}Ca , ^{26}Al , ^{36}Cl , ^{53}Mn) could be product of both the sources (Goswami et al., 2005; Wasserburg et al., 2006; Gounelle et al., 2007; Huss et al., 2009). Studies of any short-lived nuclide that is a distinct product of either stellar nucleosynthesis or energetic particle production enables us to identify and infer the contribution from such a source to the inventory of the other short-lived nuclides present in the early solar system. Studies of multiple SLNs in the same object can therefore provide relevant information to find out if these SLNs are cogenetic (Sahijpal et al. 1998, 2000; Marhas et al., 2002; Meyer 2005). If we consider the case of ^{60}Fe , which is a distinct product of stellar nucleosynthesis, a combined study of this and other SLNs of possible stellar origin will provide information if they were also co-produced in the same stellar source and were co-injected along with ^{60}Fe into the protosolar cloud. In such a case it should be possible to concurrently explain the observed abundances of the SLNs in the object assuming a single stellar source. This also allows us to construct a valid chronology of objects formed during various epochs in the early

solar system, with reference to the first solar system solids, the CAIs. On the other hand, if some of the SLNs, e.g. ^{10}Be , that are produced due to interactions of energetic particles from the active early Sun with the gas and dust present in the solar nebula, their abundances in early solar system objects will not provide any meaningful information on relative chronology. Instead, they will provide information regarding the energetic environment in the solar nebula and activity of the early Sun.

1.5 Scope of the Present Study

The primary aim of this work is to study records of the now-extinct short-lived nuclide, ^{60}Fe , a unique product of stellar nucleosynthesis, in early solar system objects and infer its Solar System Initial (SSI) abundance. Several stellar sources, such as a Thermally Pulsating Asymptotic Giant Branch star (TP-AGB), Supernova (SN), and Wolf-Rayet star (WR) can produce ^{60}Fe in different amounts depending upon their initial mass and metallicity. A proper knowledge of SSI $^{60}\text{Fe}/^{56}\text{Fe}$ will allow us to identify its plausible stellar source and hence the contribution from this source to the inventory of the other short lived nuclides of stellar origin. We can then combine this information with data for SSI abundances of other short-lived nuclides e.g. ^{26}Al , ^{41}Ca , that are considered to be of stellar origin (Sahijpal et al., 1998, 2000) to confirm our inference about the plausible stellar source.

The possible presence of ^{60}Fe in early solar system object was first reported by Birck & Lugmair (1988) based on studies of nickel isotopes records in Allende CAIs. They observed isotopic anomalies in ^{60}Ni as well as in ^{62}Ni and ^{64}Ni that led them to infer an upper limit initial $^{60}\text{Fe}/^{56}\text{Fe}$ value of 1.6×10^{-6} at the time of CAI formation, assuming that the observed excess in ^{60}Ni is solely due to in-situ decay of ^{60}Fe . However, because of the presence of nucleogenic anomalies in ^{62}Ni and ^{64}Ni , the possibility that the excess observed in ^{60}Ni could be partly due to preserved nucleosynthetic anomaly in the CAIs cannot be ruled out. Additionally, Volkening and Papanastassiou (1989) reported anomalous Fe isotope composition with conspicuous excess in ^{58}Fe in FUN CAIs (Volkening & papanastassiou 1989). Endemic nucleogenic isotopic anomalies are also found for Fe-group elements in CAIs (Niederer et al., 1981; Niederer & Papanastassiou 1984; Birck & Allègre 1988; Völkening & Papanastassiou 1990). Thus, ^{60}Ni excess seen in CAIs could not be attributed to decay of ^{60}Fe unambiguously. Further, being a moderately volatile

element Fe is not easily incorporated in refractory mineral phases constituting CAIs. The absence of phase with high Fe/Ni ratio in CAIs, coupled with the presence of nucleosynthetic Ni anomalies in them, make it difficult to look for ^{60}Fe records in CAIs.

The first evidence for the presence of live ^{60}Fe in early solar system was reported by Shukolyukov & Lugmair (1993a) based on the observed Fe-Ni isotope systematics in a differentiated meteorite (Eucrite), Chervony Kut. They observed a correlation of excess ^{60}Fe with the nickel concentration in bulk samples and reported an initial $^{60}\text{Fe}/^{56}\text{Fe}$ value of $(3.9 \pm 0.6) \times 10^{-9}$ at the time of formation of Chervony Kut. However, the mineral isochron in this meteorite was found to be disturbed and another eucrite, Juvinas, with the same formation age as Chervony Kut, yielded initial $^{60}\text{Fe}/^{56}\text{Fe}$ value lower by almost an order of magnitude (Shukolyukov & Lugmair 1993b; Lugmair & Shukolyukov 1998). Choi et al. (1999) studied Ni isotope abundances in secondary sulfides in a CAI and the result provided an upper limit that was close to that reported by Birck & Lugmair (1988).

Because of the above difficulties associated with interpreting results from analyses of CAIs, later attempts were focused on studies of Fe-rich phases in chondrules. Several studies of Fe-Ni isotopes in various Fe-rich phases in Unequilibrated Ordinary Chondrites (UOCs) of low petrologic grades have been conducted in recent years. Tachibana and Huss (2003) analyzed Fe-rich phases like troilite (FeS) and magnetite (Fe_3O_4) found in chondrule rims and matrix and inferred an initial $^{60}\text{Fe}/^{56}\text{Fe}$ value of $(1-2) \times 10^{-7}$ in troilite grains in Bishunpur (LL3.1) and Krymka (LL3.4). A subsequent study of troilite in matrix of UOC Semarkona, that are not associated with metal, yielded a much higher value of $(0.92 \pm 0.24) \times 10^{-6}$ (Mostefaoui et al., 2005). The lower initial values in troilites in Bishunpur and Krymka seen in the earlier study were explained by these authors as due to exchange of Ni between sulfide and associated metal phases. However, lack of independent estimate of the formation of the sulphide phases, relative to CAIs, made it difficult to infer the Solar System Initial (SSI) $^{60}\text{Fe}/^{56}\text{Fe}$. A study of Fe-Ni isotope systematics in silicate phases in UOC chondrules (Tachibana et al., 2006) yielded initial $^{60}\text{Fe}/^{56}\text{Fe}$ values of $(2-3.7) \times 10^{-7}$ at the time of formation of these chondrules. These authors assumed a time interval of 1.5-2 Ma between the formation of CAIs and chondrules and inferred a SSI $^{60}\text{Fe}/^{56}\text{Fe}$ value of

$(5-10) \times 10^{-7}$. Thus, in all the previous studies, conducted in Fe-rich oxides, sulphides or silicates, it was necessary to assume the time of formation of the analysed phases to infer SSI $^{60}\text{Fe}/^{56}\text{Fe}$. An independent estimate of the time of formation of the analyzed objects/phases is therefore crucial for an unambiguous estimate of the most plausible SSI $^{60}\text{Fe}/^{56}\text{Fe}$ value. A combined study of $^{53}\text{Mn}-^{53}\text{Cr}$ and $^{60}\text{Fe}-^{60}\text{Ni}$ systematics in sulphide phases from unequilibrated enstatite chondrites (UECs) using ion microprobe showed a large variation, $(2-20) \times 10^{-7}$ for inferred initial $^{60}\text{Fe}/^{56}\text{Fe}$; this variation is most probably a reflection of disturbed isotope systematics in the thermally metamorphosed sulphides phases (Guan et al., 2007). Based on Al-Mg and Ni isotopic studies on a suite of samples that include chondrites, achondrites and iron meteorites, Bizzarro et al. (2007) suggested that the injection of ^{60}Fe in solar nebula took place approximately 1 Ma after the injection of ^{26}Al from the same stellar source. However, this data set appears to have suffered from analytical bias (Cook et al., 2008; Dauphas et al., 2008; Regelous et al., 2008). It is obvious that a proper estimate of SSI $^{60}\text{Fe}/^{56}\text{Fe}$ is lacking at present. As noted earlier, a precise value of $^{60}\text{Fe}/^{56}\text{Fe}$ is essential both for constraining the stellar source of ^{60}Fe and for estimating the contribution from this source to the inventory of the other SLNs present in the early solar system. This will also help us check the proposal of late injection of ^{60}Fe , relative to ^{26}Al , and the plausible role of ^{60}Fe as a heat source, during the evolution of planetesimals in the early solar system, along with the well established primary heat source, ^{26}Al . The work presented in this thesis attempts to answer these issues by a combined study of Fe-Ni and Al-Mg isotope systematics in a selected set of UOC chondrules.

The primary aims of this thesis work are:

- I. *Establish solar system initial $^{60}\text{Fe}/^{56}\text{Fe}$:* There exists an uncertainty of close to an order of magnitude in the reported SSI $^{60}\text{Fe}/^{56}\text{Fe}$ values by different groups at present. A major lacuna in these studies is the absence of information on the time of formation of the analyzed objects, relative to CAIs, an input needed to infer SSI $^{60}\text{Fe}/^{56}\text{Fe}$. Studies of both Fe-Ni and Al-Mg isotope systematics in individual chondrules from UOCs of low petrologic grades were conducted to obtain a robust value of SSI $^{60}\text{Fe}/^{56}\text{Fe}$. The data from Al-Mg isotope systematics provide information on the time of formation of the analyzed chondrules, relative to CAIs.

II. *Constrain the stellar source of ^{60}Fe :* The SSI $^{60}\text{Fe}/^{56}\text{Fe}$ obtained in this study will help in choosing between the potential stellar source(s) of ^{60}Fe viz. a Thermally Pulsing Asymptotic Giant Branch star or a Wolf-Rayet star or a Supernova. This will also allow us to infer the contribution made by this source to other short-lived nuclides present in the early solar system.

III. The question of late injection of ^{60}Fe , relative to ^{26}Al , from the same stellar source, suggested recently, can also be addressed by looking for possible correlation or lack of it between the initial $^{60}\text{Fe}/^{56}\text{Fe}$ and $^{26}\text{Al}/^{27}\text{Al}$ at the time of formation of the analyzed UOC chondrules.

Although not addressed in this thesis, a related issue will be whether the SSI $^{60}\text{Fe}/^{56}\text{Fe}$ obtained in this study will also allow us to infer the role of ^{60}Fe as a plausible heat source during early evolution of planetesimals, along with the well established primary heat source, ^{26}Al .

A description of the major analytical instruments used in this study, namely, the Electron Probe Micro-Analyser (EPMA) and the high-mass-resolution Secondary Ion Mass Spectrometer (SIMS or ion microprobe) along with the experimental procedures are presented in Chapter 2. Chapter 3 contains details of the analysed samples (UOC chondrules) as well as the chemical composition of the phases in individual chondrules analyzed for isotope records. The selection of phases with high Fe/Ni or Al/Mg for isotope studies is based on this data set. Results obtained from studies of Fe-Ni and Al-Mg isotope systematics in selected phases within individual chondrules are presented in Chapter 4. Discussion of the result obtained in terms of the primary aims of this study, viz., plausible value of SSI $^{60}\text{Fe}/^{56}\text{Fe}$, stellar source of ^{60}Fe , as well as other questions noted above are enumerated in Chapter 5. The last chapter (Chapter 6) summarizes the results and conclusions obtained in this study and a brief outline for future work.

CHAPTER 2: EXPERIMENTAL TECHNIQUES

A Study of Fe-Ni and Al-Mg isotope systematics was carried out on suitable phases in selected chondrules from three unequilibrated ordinary chondrites (UOCs) of low metamorphic grades. Identification of phases within individual chondrules with high Fe/Ni and Al/Mg was necessary for the study of these two isotope systems. An Electron Probe Micro Analyser (EPMA: Cameca SX 100) was used for imaging, identification as well as characterization of such phases within each of the analyzed chondrules. Fe-Ni and Al-Mg isotope analyses in the identified phases were carried out using a Secondary Ion Mass Spectrometer (SIMS: Cameca ims-4f), also known as ion microprobe. In this chapter a description of the analytical instruments along with experimental procedures used in this study are presented.

2.1 Electron Probe Micro Analyzer (EPMA)

Electron probe microanalysis is one of the widely used approach for qualitative as well as quantitative determination of major and minor element composition of solids at small spatial scale (\geq micron). EPMA technique has advantages over other techniques, such as, instrumental/radioactive neutron activation analysis (INAA, RNAA), inductively coupled plasma atomic emission spectroscopy (ICP-AES), as it is non destructive in nature. An EPMA (Cameca SX100; Fig. 2.1) that is capable of providing back scattered electron (BSE) image, secondary electron (SE) image and X-ray elemental image of a sample in addition to performing quantitative elemental analysis of solids with a detection limit of close to or less than a hundredth of weight percent was used in this study.

In EPMA, an electron beam is generated from a tungsten filament by heating it to ~ 200 °C and the electrons are accelerated to 5-20 keV and focussed on to a polished carbon coated sample surface using a set of electromagnetic (condenser) lenses. The energetic electron beam interacts with the near surface atomic layers of the sample producing back-scattered electrons, secondary electrons and characteristic X-rays of elements ($Z \geq 11$) depending upon the energy of the electron beam. The secondary and back-scattered electrons can be used to obtain image of sample surface with a

resolution of less than a few microns. Elemental concentration maps of the surface can also be generated by using either a wavelength dispersive X-ray spectrometer (WDX) or a energy dispersive X-ray spectrometer (EDX) attached to the probe.

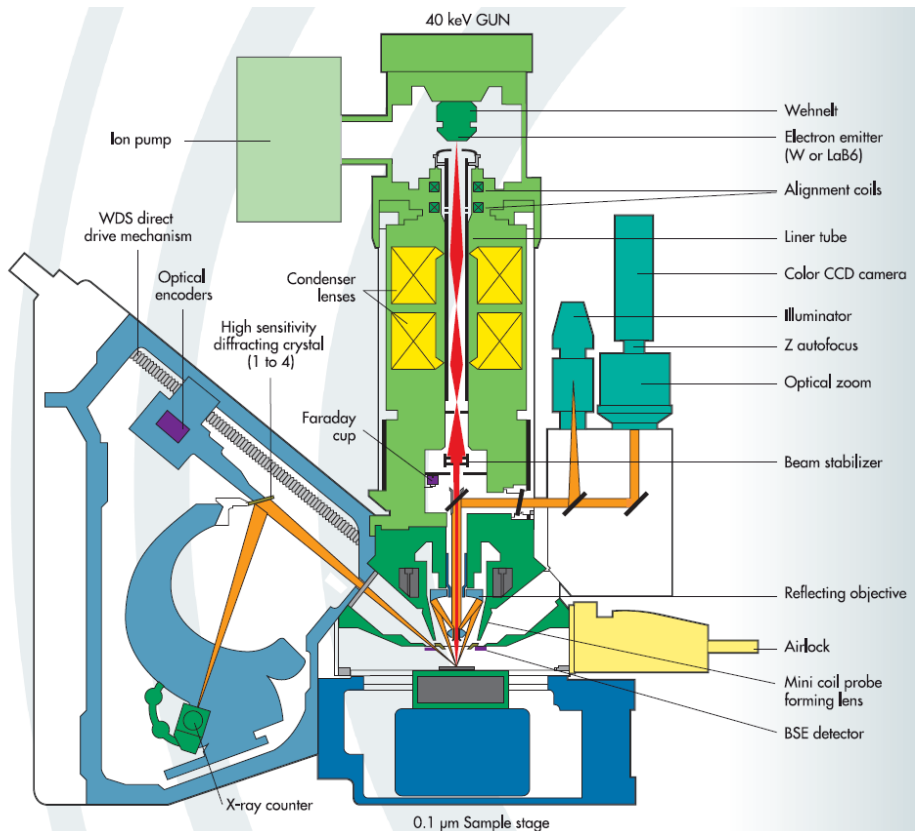


Fig. 2.1 Schematic diagram of Electron Probe Micro Analyser (Cameca SX100).

In the present study, the EPMA was used to obtain magnified back-scattered and elemental images of selected chondrules. Iron (Fe), calcium (Ca), aluminium (Al), and magnesium (Mg) X-ray elemental maps were obtained for each chondrule by rastering a micron-size, 70 nA electron beam on the sample surface. The Fe-rich and Al-rich regions seen in the elemental maps were subsequently analysed using an electron beam accelerated to 15 kV with beam size of ~1 micron and carrying a beam current of ~20 nA for quantitative elemental analysis. Suitable reference standards were used for instrument calibrations.

2.2 Secondary Ion Mass Spectrometer

The high mass resolution secondary ion mass spectrometer (Cameca ims-4f) used in this study has been designed for use both as an ion microscope as well as an ion microprobe. The main salient feature of the ion microprobe is its capability for performing in-situ isotopic analysis of solids with a spatial resolution of a few microns. This makes it ideal for isotopic studies of chondrule microphases with high Fe/Ni and Al/Mg ratios conducted in this work. Secondary ion mass spectrometers have been extensively used in the fields of cosmochemistry and geochemistry during the last two decades.

In a secondary ion mass spectrometer (Fig. 2.2) an energetic primary ion beam sputters secondary neutral atoms, single and multiple charged ions as well as molecular ions from the target solid kept at a high potential of 4.5KV. In the case of non-conducting solids like the silicate chondrules analyzed in this study, the sample is coated with gold or carbon to avoid sample charging effect during primary ion bombardment. The sputtered secondary ions are then extracted using a grounded potential plate. This plate and the sample at a high potential constitutes an immersion lens. The sputtered secondary ions then pass through a contrast aperture, an entrance slit and a field aperture before entering an electrostatic analyzer (ESA) constituting of two hemispherical plates. The ESA disperses the incoming ions of different energies in such a manner that they are sorted as a function of energy at the exit plane of the ESA. The ions with lower energies are deflected the most and hence lie closer to the innermost plate, while ions with higher energy are dispersed lesser and lie closer to the outer plate. Ions having a small spread of energy (~20 eV) around the mean energy (4.5 KeV) are selected by using a moveable energy (slit) window and enters the magnetic sector which produces dispersion of this nearly mono-energetic ions as a function of their mass to charge (m/q) ratio. Ions representing a given m/q can be detected by using either a fluorescent screen or their intensity measured using a faraday cup or an electron multiplier. The Cameca ims-4f ion microprobe basically consists of a source, electrostatic and magnetic analyser and detectors. The primary beam passing through the primary column and the sample to be analyzed constitute the source. The secondary column hosting various lenses and apertures, an electrostatic analyser and a magnetic sector constitute the analyser, while the faraday

cup, electron multiplier and the fluorescent screen serve as detectors in different modes. In the following sections, each of these components of the ion microprobe and their working principles are briefly described.

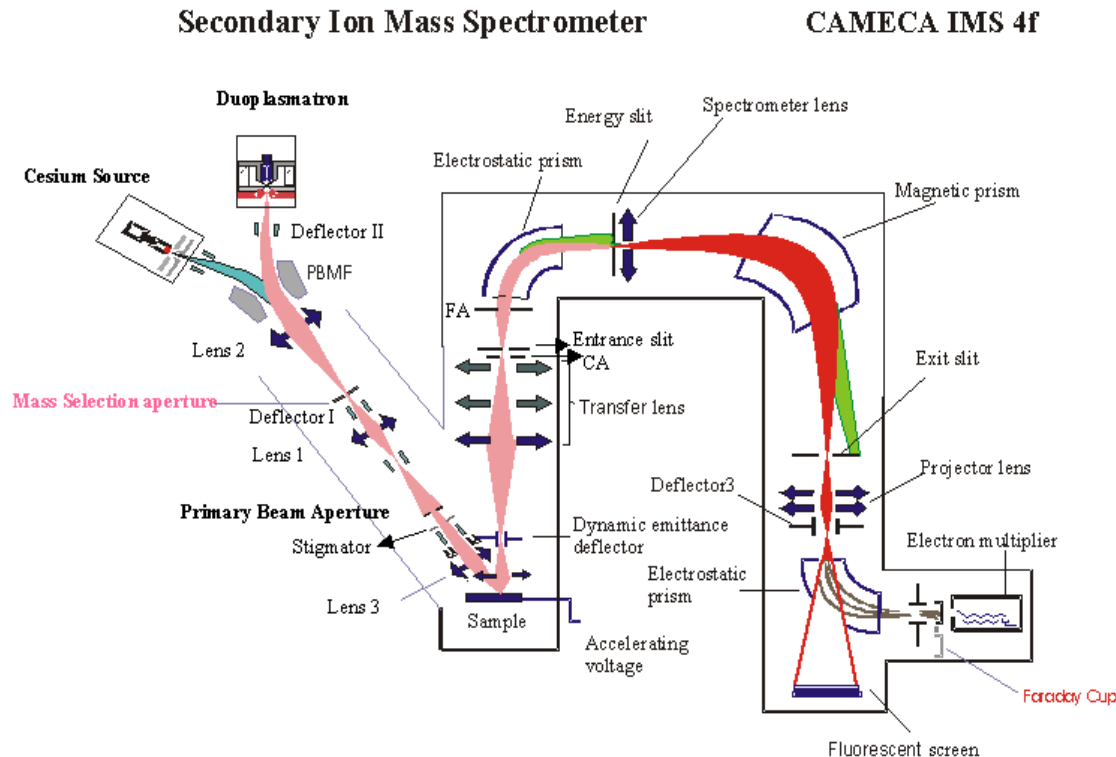


Fig. 2.2 Schematic diagram of secondary ion mass spectrometer (Make Cameca ims-4f).

2.2.1 Primary Column

Primary Beam Sources

The Cameca ims-4f has two types of primary beam sources, a duoplasmatron and a caesium (Cs) source. The duoplasmatron works on cold cathode discharge principle and can be used to generate ions of both (duo) kinds from a gaseous source (e.g. oxygen) while caesium source generates positively charged beam of Cs by thermal excitation/emission. In a duoplasmatron (Fig. 2.3), pure gas (oxygen in our case) at low pressure is leaked through a hollow cathode in a controlled manner using a regulating knob. A potential difference of few hundred volts (~ 400 V) between cathode and anode creates plasma using an arc which is confined within a small

region using a magnetic coil. An intermediate electrode, moveable in vertical (Z) plane, also called Z electrode, is used to select positive or negative ions from the plasma. The duoplasmatron can be floated at a high potential in the range of 5-20 kV

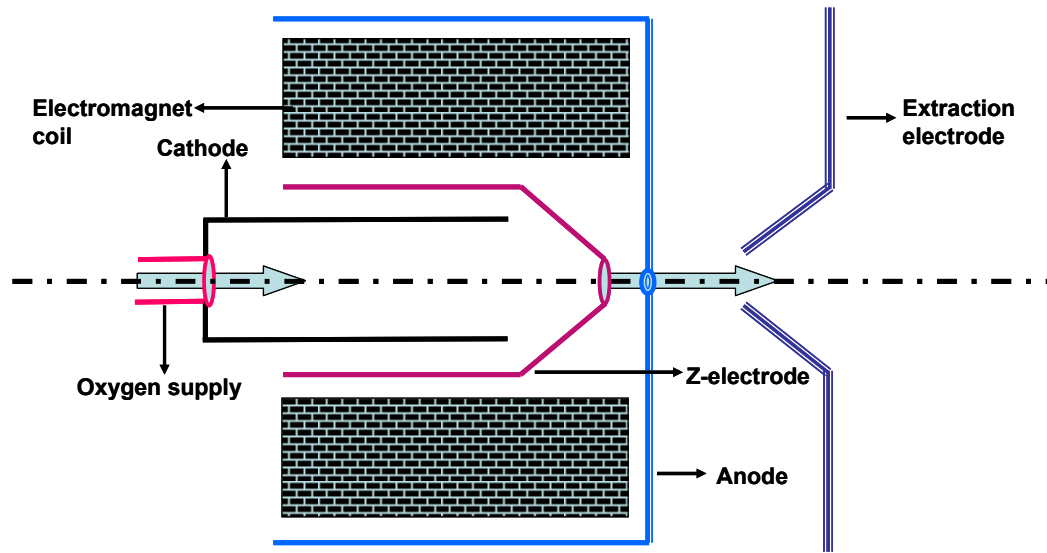


Fig. 2.3 Schematic diagram of Duoplasmatron.

in steps of 2.5 kV, with respect to a grounded extraction plate that is used to extract ion beam from the duoplasmatron. A small electro-magnetic sector called primary beam mass filter (PBMF) is used to select desired ions from the accelerated beam apart from removing spurious contaminant ions. Negative oxygen ions provide better yields for electropositive elements and hence in this study a $^{16}\text{O}^-$ beam was used to sputter secondary ions (Ni^+ , Fe^+ and Al^+ , Mg^+) for studies of Fe-Ni and Al-Mg isotope systematics.

Caesium Source:

A metal reservoir containing solid caesium chromate or carbonate tablet ($\text{Cs}_2\text{CrO}_4/\text{Cs}_2\text{CO}_3$) is heated to 400°C to generate caesium vapour (Fig. 2.4). The caesium vapour is then passed over a surface of tungsten (ionizer) heated to 1100°C , that ionizes Cs to Cs^+ ion by electron transfer. The ionizer and reservoir are kept at a high voltage of 10 kV and are independently heated by two annular filaments. A grounded extraction electrode placed in front of the ioniser extract and accelerate the Cs^+ ions. Cs^+ ions provide better yields for electronegative elements and used for generating secondary negative ions of C, O, Si etc.

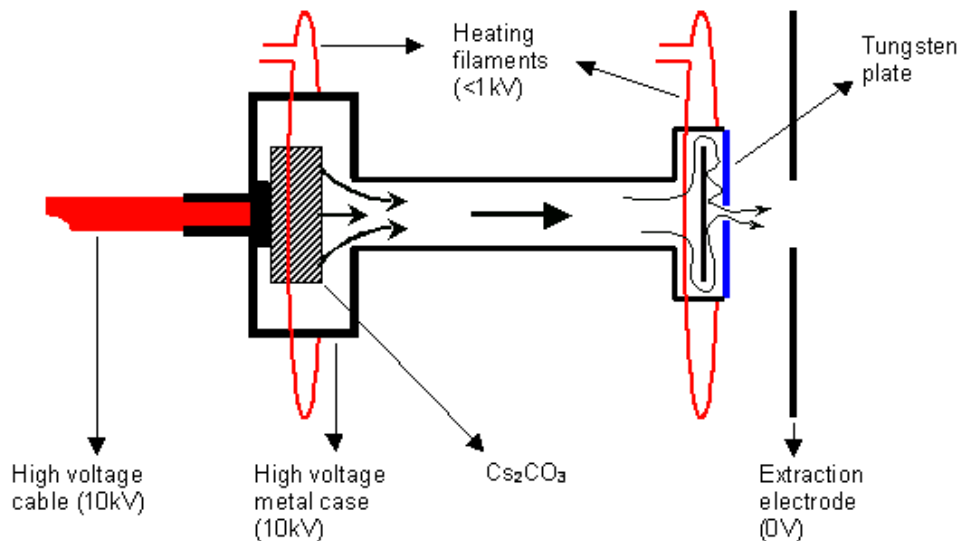


Fig. 2.4 Schematic diagram of the Caesium Source

Primary Column:

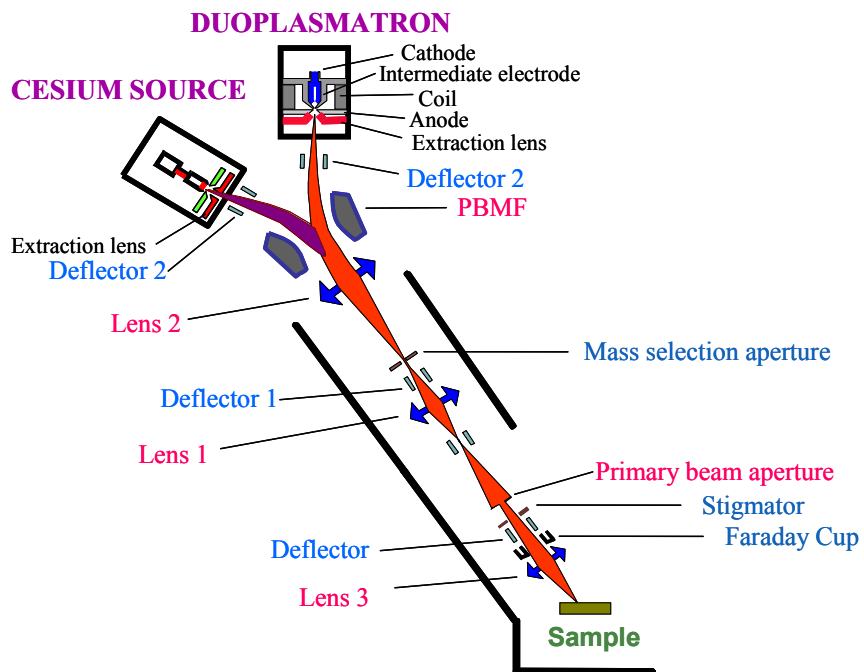


Fig. 2.5 Schematic diagram of the primary sector consisting of source and the primary column hosting lenses, apertures and deflectors.

The ion beam generated by either the duoplasmatron or the caesium source is deflected into the primary column by the primary beam mass filter. The primary column hosts lenses, apertures, stigmator and deflectors, that are adjusted to obtain desired beam size, beam current and finally focus the beam on to the sample surface (Fig. 2.5). All lenses in the primary column are electrostatic einzel lens consisting of three plates with circular aperture in their centre such that only the inner plate is energised to variable values while outer plates are kept at ground potential so that the energy of the ion beam remains steady. The plates can be set at different voltages to make them act as either a converging or a diverging lens. Lens L1 is used to maximise the beam current while L2 aligns the beam through the mass aperture and lens L3 is used to focus the beam on to the sample surface (Fig. 2.5). Two oppositely charged parallel metallic plates constitute a deflector that is used to align the beam along the optical axis of the primary column. Molybednum coated circular metallic plates with holes of different sizes are used as apertures that remove non-paraxial ion beam to reduce various aberrations in the ion image. An eight-plate stigmator placed before lens L3 is used to remove astigmatism and aligns the primary beam along its optic axis. A retractable faraday cup in the primary column is used to optimise the settings of various lenses, deflectors, and stigmators for maximising primary current.

2.2.2 Secondary Sector

The secondary sector consists of a secondary column and detectors (Fig. 2.6). The secondary column hosts an immersion lens, a set of three transfer lenses, a contrast aperture, an entrance slit, a field aperture, an electrostatic prism, an energy slit, a spectrometer lens, a magnetic sector, a projector lens, deflectors and secondary ion detectors. Several options exist for ion detection that include fluorescent screen for viewing ion image and faraday cup and electron multiplier for quantitative estimate of ion intensities. Analysis of positive secondary ions was conducted using a primary 12.5 keV $^{16}\text{O}^+$ beam that strikes the surface of the polished solid, coated with carbon/gold to avoid charge build up, at an angle of 30° . Sputtered secondary ions

generated by the primary beam from the sample surface can have a spread in energy of ~ 100 eV or more although most of them will have energy within a narrow spread of ≤ 20 eV. The sample kept at a potential of 4.5 kV along with a grounded plate, having a circular aperture in the centre, placed at a distance of a few mm from the sample, constitute an immersion lens. The immersion lens extracts the secondary ions generated at the sample surface and they get accelerated and energised during their

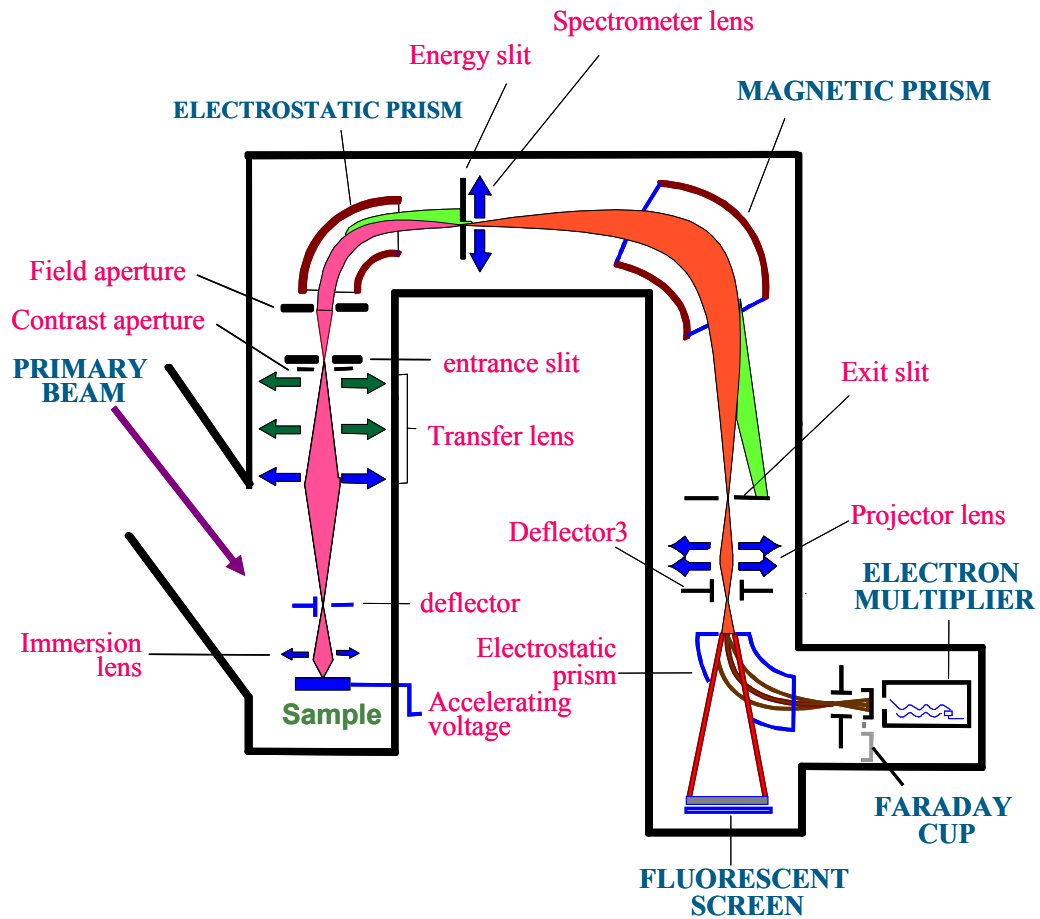


Fig. 2.6 Schematic diagram of the secondary sector constituting the analysers and detectors.

passage through this lens that also focuss the secondary ions into the secondary column (Figs. 2.6; 2.7). The immersion lens forms a demagnified virtual image ($A'_iB'_iC'_i$) of the sample ($A_iB_iC_i$) such that all ions having same energy (E) and angle (α) appear to be coming from a single point called cross over (CP in Fig. 2.7). A set of transfer lenses, all three plate einzel lens assembly, are used to obtain a real magnified image of the crossover and the sample in the plane of contrast aperture and field

aperture, respectively. The instrument provides three different setting of magnification ($25\mu\text{m}$, $150\mu\text{m}$, and $250\mu\text{m}$ images), which is obtained by suitably energising the transfer lenses. For all the analysis reported in this thesis, the instrument was used at a magnification setting of $150\mu\text{m}$, while the others magnification settings were primarily used for tuning of the instrument. The contrast aperture, entrance slit and field aperture are located successively after the transfer lens. The instrument is provided with four different platinum/ iridium coated metallic

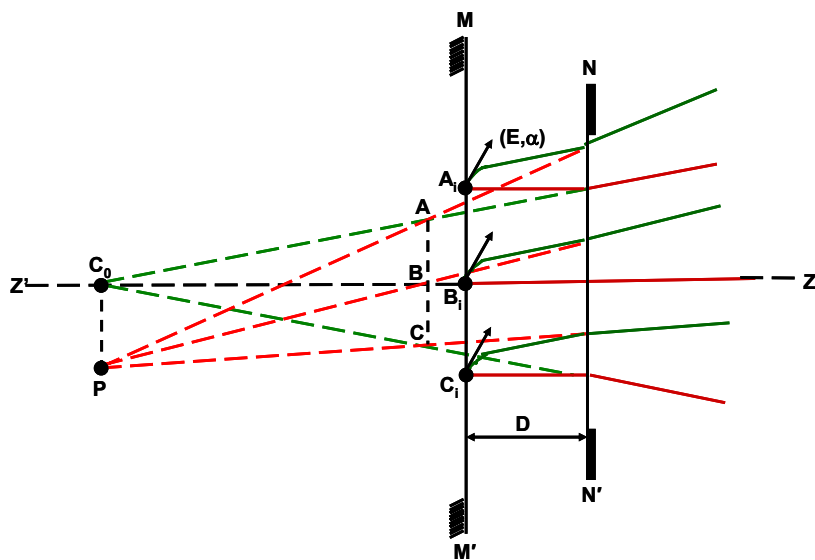


Fig. 2.7 Schematic diagram showing trajectory of secondary ions emitted from the sample surface.

circular contrast apertures ($20\mu\text{m}$, $50\mu\text{m}$, $150\mu\text{m}$ and $400\mu\text{m}$) just before the entrance slit where the cross over image is formed. The contrast aperture is used to improve the image by restricting ions with larger angular dispersion whereas variable entrance slit limits the size of crossover thereby reducing spherical aberration and improving the spatial resolution of the ion image. Field apertures of different sizes ($100\mu\text{m}$, $400\mu\text{m}$, $750\mu\text{m}$, $1800\mu\text{m}$) can be selected that allows selection of ions coming from a particular region of the sputtered sample surface to pass through the electrostatic analyser.

Electrostatic Analyser

The secondary ions after passing through the field aperture enter an electrostatic analyser. Two spherical plates having a mean internal diameter of 8.5 cm, cut with a

sector angle of 90^0 and separated from each other by 1cm, constitute the electrostatic sector. The inner and outer plates are so energised that ions with mean energy of 4.5 keV travel along the central circular path while ions with higher and lower energy travel along trajectories such that ions with lower energy move along a circle of smaller radius, while ions with higher energy travel along a circle of larger radius. The 90^0 sector electrostatic analyser thus sorts ions according to their velocity (energy) at its exit plane. A variable energy slit, movable in direction perpendicular to ion beam, allows selection of ions within a given range of energy and limits energy spread of incoming ions, within a narrow range around the mean energy, at the exit point. An energy window of 25eV was used in the present study. This ability of using apertures to limit ion paths both before and after the electrostatic sector allows reduction in beam divergence and chromatic aberration that are very essential for high mass resolution studies.

Magnetic Sector

The secondary ions coming out of the electrostatic sector, with a small energy spread of ~ 25 eV, are focussed on to the entrance plane of the magnetic sector using a spectrometer lens. The ions get dispersed according to their mass by charge ratio (m/q) when they pass through the 30^0 electromagnetic sector. An electromagnet of radius of 12.7 cm and a gap width of 8 mm between them act as the magnetic prism. The unique design of ims-4f with an electrostatic analyser followed by a magnetic sector allows double focussing of the ion beam in both energy and direction.

Detectors

The detecting system of the Cameca ims-4f consists of a channel plate connected to a fluorescent screen, an electron multiplier and a faraday cup. In the ion counting mode, an electrostatic sector deflects the ion towards the retractable faraday cup, placed in front of the electron multiplier and one of these detectors may be chosen for operation. In the case of imaging mode, the ions are allowed to fall on a channel plate through a gap in the electrostatic sector and one can have an ion image of the sample surface or of the entrance slits.

Electron Multiplier

A deflector placed after the exit slit makes the secondary ions fall on electron multiplier in the counting mode. Electron multiplier (EM) is made up of a series of curved metallic plates/electrodes also called dynodes. Each dynode is kept at a successively higher potential than the previous one that leads to an avalanche of secondary electrons after successive stage. The (SEV 217, Pfeiffer-Balzer) electron multiplier used in this study has seventeen stages that allows high amplification of the signal. The first dynodes is kept at ground potential while each successive one is at a higher potential of ~ 400 V. The EM is operated in pulse counting mode using high speed electronic counter. The detection efficiency of the electron multiplier deteriorates with time and the detector is replaced when the efficiency falls below 70%. The basic parameters such as the background, dead time and efficiency of the counting system are monitored on regular basis.

Faraday Cup

A metal cup connected to a high resistor and a discriminator circuit serves as the detecting system when the count rate is higher than 2×10^6 . Measurement during this study involved low counting rates hence faraday cup was not used for ion counting in this study.

Channel Plate

Ion images can be obtained using a channel plate that amplifies the signal of incident ions by secondary electron emission before the electron to strike a fluorescent screen and to produce the ion image. Since the ion image of the sample is transferred to the fluorescent screen through the mass analyser, the ion microprobe in this mode serve as an ion microscope. The brightness of the image is proportional to the intensity of ion reaching the channel plate and can be viewed on a video monitor or CCD using a suitable coupling mechanism.

2.2.3 Vacuum System

The source region, primary column, secondary column and the detectors are kept in high vacuum, generated and maintained by two rotary, four turbo molecular and two ion pumps. The vacuum on the primary column is $\sim 10^{-5}$ torr, while the sample

chamber is maintained at better than $\sim 10^{-6}$ torr. The secondary sectors, including the detectors are maintained at still higher vacuum of $\sim 10^{-8}$ torr supported by the two ion pumps. A couple of thermocouple gauges and a pirani gauge monitor vacuum system in different active regions of the ion microprobe.

2.3 Ion Microprobe Studies of Fe-Ni & Al-Mg Isotope System

2.3.1 Fe-Ni isotope System

Fe-Ni and Al-Mg isotope systematics in selected phases of chondrules from UOCs along with appropriate terrestrial analogue standards were studied using the ion microprobe. Both iron and nickel have more than three stable isotopes and their relative abundances are shown in Table 2.1.

Table 2.1 Stable isotopes of Fe and Ni and their abundances

Element	Atomic mass	Abundance (%)	Normalized Ratio
^{26}Fe	54	5.8	0.06324
	56	91.72	1.0*
	57	2.2	
	58	0.28	0.02399
^{28}Ni			0.00305
	58	68.27	1.0*
	60	26.10	
	61	1.13	0.38231
	62	3.59	0.01655
	64	0.91	0.05259

Fe/Ni = 18.26 (Solar Abundance); *Most abundant isotope

A focussed 12.5 KeV $^{16}\text{O}^-$ primary beam with intensity varying from 8-15 nA and of was used to generate positive secondary ions of Fe and Ni from the analyzed phases (olivine and pyroxene) in the UOC chondrules. The beam was focussed to have a spot size of $\sim 10 \mu\text{m}$ on the sample surface. A typical analytical procedure for Fe-Ni isotope systematics involves measuring intensities of ^{57}Fe , ^{60}Ni and ^{62}Ni ions in cyclic sequence, in the peak jumping mode, at a mass resolution ($M/\Delta M$) of ~ 4000 , where

the electron multiplier for detection of ions. At this mass resolution all major peaks except those due to hydrides are well resolved; the hydride interference contribute at less than per mil level as evident in Figs. 2.8-2.10, where high mass resolution spectra at masses ^{57}Fe , ^{60}Ni and ^{62}Ni obtained in a terrestrial olivine standard are shown.

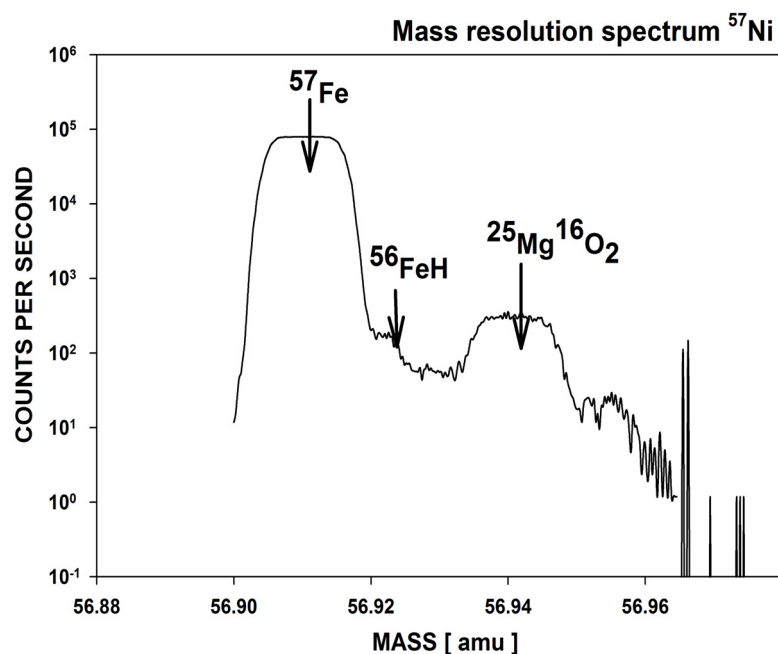


Fig. 2.8 High mass resolution spectrum at mass 57

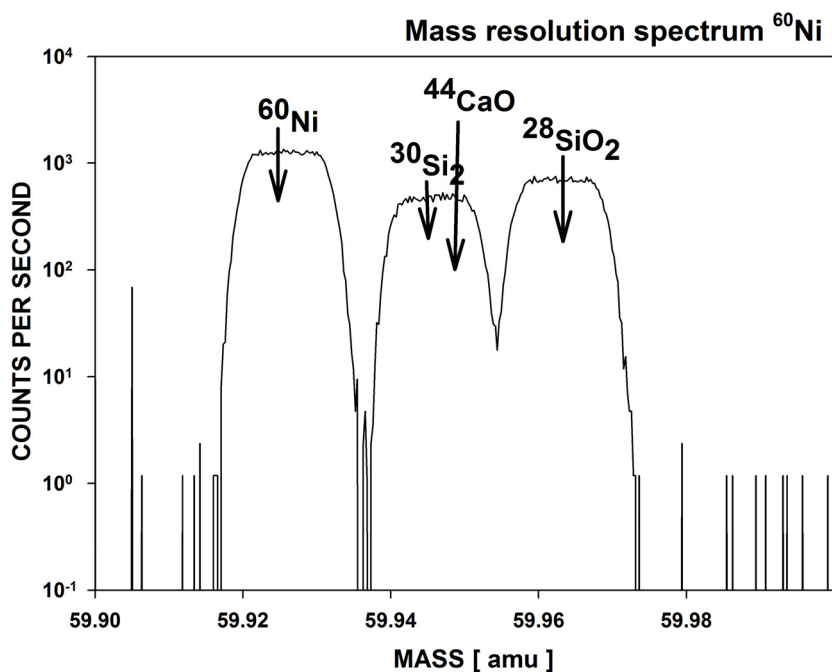


Fig. 2.9 High mass resolution spectrum at mass 60

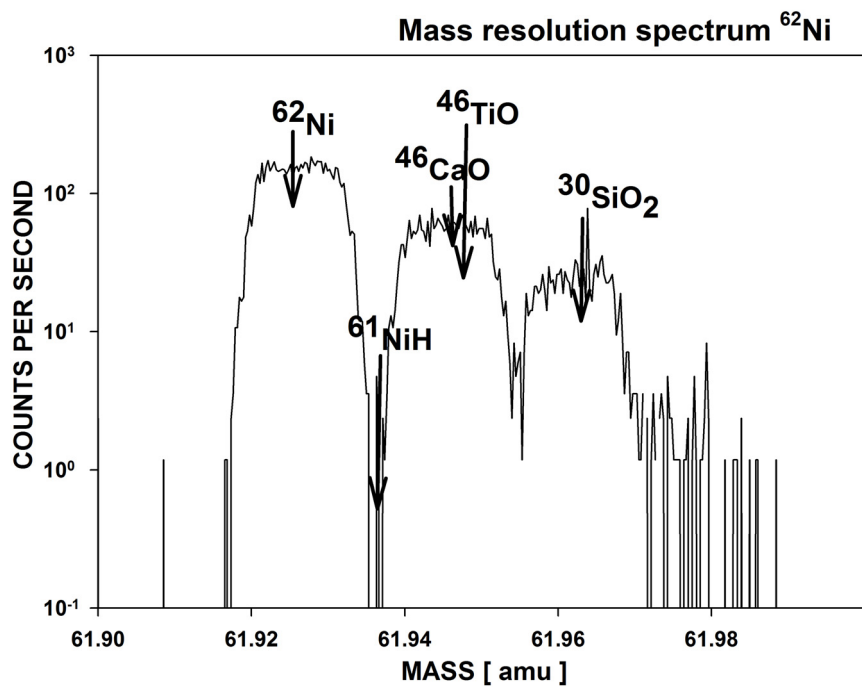


Figure 2.10 High mass resolution spectrum at mass 62

The typical count rates of the Fe and Ni ions ($^{57}\text{Fe}^+$, $^{60}\text{Ni}^+$, $^{62}\text{Ni}^+$) in the analysed chondrule phases were 10^5 , 10-20, 1-5 cps, respectively, in our instrument operating conditions. The mass 56.5 was also included in the analysis routine to monitor the dynamic background of the counting system because of the low count rate of ^{62}Ni . The background count rate varied between ~0.01 to 0.02 cps during different measurement sessions. A typical analysis routine involved measuring intensities of 56.5, ^{57}Fe , ^{60}Ni , ^{62}Ni ions with count times of 3-5, 1, 10, and 50 seconds, respectively, to have statistically significant data. Each analysis consisted of twenty blocks of data, with five cycles in each block and the analysis lasted for a couple of hours. Automatic mass calibration was done at mass ^{57}Fe after every (20-25) cycles. Multiple analyses on the same spot were carried out, as long as count rates and $^{56}\text{Fe}/^{62}\text{Ni}$ ratio remained nearly the same (details provided in Chapter-4), to improve analytical precision.

The measured isotopic ratios obtained using the ion microprobe may differ from their true values because of plausible mass fractionation taking place during the production, extraction and detection of ions. The instrument mass fractionation effect can be internally corrected by measuring abundances of three or more isotopes of an element and assuming a linear or exponential mass fractionation law. Though nickel has five

stable isotopes, experimental determination of internal mass fractionation correction is difficult because of the very low abundances of ^{61}Ni and ^{64}Ni that leads to typical count rate $<1\text{cps}$ in silicates from UOC chondrules in our instrument operating conditions. Further, it is not possible to resolve isobaric interference from ^{58}Fe at mass ^{58}Ni . The instrumental mass fractionation was therefore periodically monitored during chondrule analyses sessions by measuring Ni isotope composition of terrestrial analogue silicates (olivine and pyroxene) using similar analytical condition as adopted for the sample. Phases with low $^{57}\text{Fe}/^{62}\text{Ni}$ ratio ($<\text{few times } 10^4$) present within the chondrules were also analysed in several cases during studies of Fe-Ni isotope systematics to assess the magnitude of instrumental mass fractionation.

The observed deviation, if any, in the measured isotope ratios of $^{60}\text{Ni}/^{62}\text{Ni}$ in the analyzed UOC chondrule, with respect to reference (standard) value, may be expressed as:

$$\Delta^{60}\text{Ni} = [({}^{60}\text{Ni}/{}^{62}\text{Ni}_{\text{Sample}} - {}^{60}\text{Ni}/{}^{62}\text{Ni}_{\text{Standard}}) / {}^{60}\text{Ni}/{}^{62}\text{Ni}_{\text{Standard}}] \times 1000$$

The deviation ($\Delta^{60}\text{Ni}$) is defined in parts per thousand (per mil) and denoted by the symbol ‰. We have adopted the $^{60}\text{Ni}/^{62}\text{Ni}$ reference value of 7.273 reported by Birck and Lugmair (1988).

Any deviation ($\Delta^{60}\text{Ni}$) present could be either due to instrument mass fractionation or decay of ^{60}Fe or both and need to be corrected first for instrumental mass fractionation. Since internal mass fractionation correction is not possible with data for only two Ni isotopes, this was done by using the values obtained in terrestrial analog standards during the given analysis session. The deviation of the measured $^{60}\text{Ni}/^{62}\text{Ni}$ ratio in a terrestrial olivine (obtained from Vernadsky Institute, Moscow) from the reference value, measured periodically during the entire period of study varied within a few ‰/amu (Fig. 2.11). The weighted average mean and standard deviation of the total data set is $(1.2 \pm 0.7)\text{‰/amu}$. Thus, instrument mass fractionation in Ni isotope is of very small magnitude compared to statistical uncertainty in the Ni isotope ratios measured in UOC chondrules that are presented in Chapter 4. The data obtained in low Fe/Ni phases within the analyzed chondrules also suggest low magnitude of instrument mass fractionation effect for Ni isotopes.

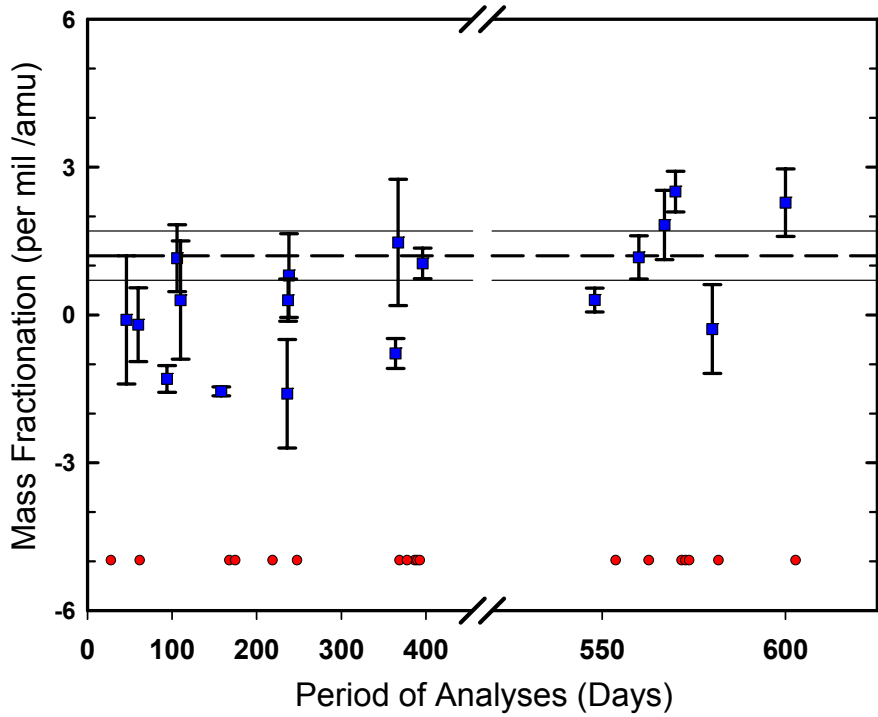


Figure 2.2 Mass fractionation inferred from measured $^{60}\text{Ni}/^{62}\text{Ni}$ in terrestrial olivine over the period of study. The days (period) during which meteoritic samples were analyzed are marked by “red” dots.

The yield of secondary ions of various elements from a solid target due to ion bombardment can be different and depends on the target composition. Thus, the inferred ratio of abundance of two isotopes of different elements (e.g., $^{57}\text{Fe}/^{62}\text{Ni}$), based on measurement of their secondary ion intensity using an ion microprobe, can differ from the true value. This can be taken into account by determining relative ion yield (λ) or sensitivity factor (SF) of the elements of interest by comparing the ion intensity ratio (e.g. $^{57}\text{Fe}^+/\text{Fe}^{60}$) obtained with the ion microprobe with the elemental ratio measured using electron microprobe and considering abundances of the isotopes of interest. The relative Ni/Fe ion yield can be expressed as:

$$\lambda (\text{Ni/Fe}) = [(\text{Fe}^{60}/\text{Fe}^{57})_{\text{electron microprobe}} / (\text{Fe}^{60}/\text{Fe}^{57})_{\text{ion microprobe}}]$$

The ion yield may vary with composition of the analysed phases and instrument settings and other analytical parameters adopted during isotope analysis. Relative ion

yields for Fe and Ni were obtained by analysing terrestrial analogues of the minerals analyzed in UOC chondrules with different Fe content. San-Carlos olivine (Fe = 7.64 %; Smithsonian Institution, USA), Vernadsky olivine (Fe = 15.7%; Institute, Moscow) and Augite (Fe=5.08%; Smithsonian Institution) were analysed under similar analytical conditions as used for the studies of UOC chondrules. The results suggest a dependence of sensitivity factor on Fe content at lower end (<10% Fe) although at higher Fe content the value is close to unity. Using O_2^- beam from a much larger geometry ion microprobe (Cameca ims1280), and selecting secondary ions with an energy window of ~ 25 eV, similar to the present study, Kita et al. (1998) inferred SF in the range of 0.6 – 0.9 for terrestrial olivines with a range of Fe (8-27%) content. Sugiura et al. (2006) obtained a SF value of 1 for olivine based on data obtained using a $^{16}O^-$ beam using a Cameca SIMS- 6f. They suggested that the relatively lower SF values seen by Kita et al (1998) may be attributed to the difference in the nature of the primary beam (O_2^-) used in that study. This trend is also reflected in our data as well. Since the olivines from UOC chondrules analyzed in this study have Fe content in the range 4 to 27 % and mostly >12%, we have used a sensitivity factor of 1 for (Ni/Fe) for inferring we have used a sensitivity factor of 1 for (Ni/Fe) for inferring the true $^{57}Fe^+ / ^{62}Ni^+$ ratio.

2.3.2 Al-Mg Isotope Systematics

The study of Al-Mg isotope systematics in UOC chondrules was done following already established analytical procedures (Rudraswami & Goswami 2007 and Rudraswami et al. 2008). Aluminium has only one stable isotope with mass 27 while magnesium has three isotopes with 24, 25 and 26. A 2-5nA O^- primary beam of size $\sim 5\text{-}10 \mu\text{m}$ was used to sputter secondary ions primarily from Al-rich glassy mesostasis in UOC chondrules. A mass resolution ($M/\Delta M$) of ~ 4000 is sufficient to resolve the hydride interference from NaH^+ in ^{24}Mg , MgH^+ in ^{25}Mg , ^{26}Mg and ^{27}Al as well as interference in ^{24}Mg due to doubly charged $^{48}\text{Ca}^{++}$ and $^{48}\text{Ti}^{++}$. High mass

resolution spectra at masses 24, 25, 26 and 27 are shown in Fig. 2.12.

The analytical procedures used for studying Al-Mg isotope systematics involve measuring ^{24}Mg , ^{25}Mg , ^{26}Mg and ^{27}Al ions in peak jumping mode in cyclic sequence with appropriate measurement time. The ^{24}Mg ion counts were kept below 10^5 to minimize dead time correction. A typical analysis involved twenty blocks of data with five cycles in each block. The counting time for each isotope was so adjusted that the total counts for ^{24}Mg were $\sim 10^6$ and $\sim 5 \times 10^5$ for ^{25}Mg and ^{26}Mg . Mass calibration was automatically done using ^{24}Mg as reference after every 3-4 blocks. Analyses were repeated at the same spot as long as Al/Mg ratio remained same to improve analytical precision. Instrument mass fractionation effect was evaluated internally based on the

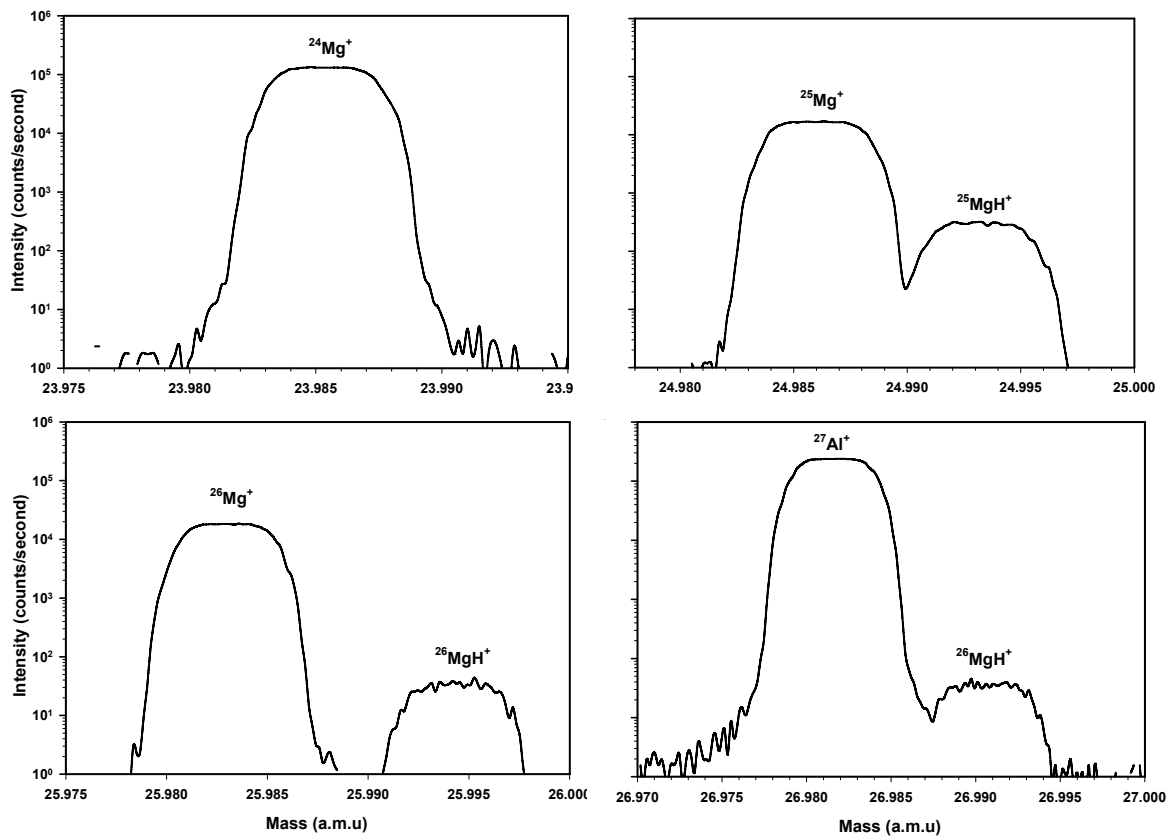


Figure 2.12 High mass resolution ($M/\Delta M \sim 4000$) spectra of ^{24}Mg , ^{25}Mg , ^{26}Mg , ^{27}Al

departure of the measured $^{25}\text{Mg}/^{24}\text{Mg}$ ratio from the reference value. Terrestrial analogues such as lake county plagioclase and GB4 glass were used to monitor instrument performance.

The measured isotopic ratio of $^{25}\text{Mg}/^{24}\text{Mg}$ and $^{26}\text{Mg}/^{24}\text{Mg}$ were used to evaluate for any departure from reference values using the following relation:

$$\Delta^{26}\text{Mg} = [({}^{26}\text{Mg} / {}^{24}\text{Mg}_{\text{Sample}} - {}^{26}\text{Mg} / {}^{24}\text{Mg}_{\text{Standard}}) / {}^{26}\text{Mg} / {}^{24}\text{Mg}_{\text{Standard}}] \times 1000$$

where $({}^{26}\text{Mg} / {}^{24}\text{Mg})_{\text{sample}}$ and $({}^{26}\text{Mg} / {}^{24}\text{Mg})_{\text{standard}}$ are the measured isotopic ratio in the sample and the reference (standard) value respectively. For Mg isotopes, the standard values are: $({}^{25}\text{Mg} / {}^{24}\text{Mg}) = 0.12663$ and $({}^{26}\text{Mg} / {}^{24}\text{Mg}) = 0.13932$ (Catanzaro et al., 1966).

A linear mass fractionation law was then used to infer possible deviation in the measured ${}^{26}\text{Mg} / {}^{24}\text{Mg}$ from reference value using the following relation:

$$\delta^{26}\text{Mg} = \Delta^{26}\text{Mg} - 2x\Delta^{25}\text{Mg}$$

A positive value of $\delta^{26}\text{Mg}$ will be suggestive of excess due to decay of ${}^{26}\text{Al}$ present in the sample at the time of its formation.

Similar to the case of Fe–Ni isotopic analysis, relative ion yields of Al and Mg, $\lambda(\text{Al/Mg})$, was inferred from measurement of standard samples with known Al and Mg content using both electron probe and ion microprobe and using the following relation:

$$\lambda(\text{Al/Mg}) = [({}^{27}\text{Al} / {}^{24}\text{Mg})_{\text{electron microprobe}} / ({}^{27}\text{Al}^+ / {}^{24}\text{Mg}^+)_{\text{ion microprobe}}]$$

Relative ion yield from GB4 glass, and lake county plagioclase inferred during this (1.37 and 1.27) are similar to those obtained earlier (Rudraswami & Goswami 2008). The relative ion yield of Al relative to Mg in glass is ~8% higher than plagioclase under similar analytical condition. Because of this small difference and unavailability of exact analogue terrestrial standard for chondrule glass (mesostasis), the ion yield measured for plagioclase standard was used to infer ${}^{27}\text{Al} / {}^{24}\text{Mg}$ ratio in chondrule glassy mesostasis.

CHAPTER 3: SAMPLE DESCRIPTION

Meteorites, that are representative fragments of asteroids, reach the earth from time to time and serve as very valuable probes for studying early evolutionary history of the solar system as well as the evolution of their parent bodies, the various types of asteroids. Those meteorites whose “fall” on earth are observed and are also recovered soon after their fall are designated as “Falls”. However, a majority of meteorites that are found accidentally or through extensive planned search (e.g. meteorites from Antarctica or hot Deserts), and are not associated with observed falls, are designated as “Finds”. Meteorites are classified into several groups; the largest group is “Chondrite” that is further classified into ordinary, carbonaceous and enstatite types. Chondrites are characterized by the presence of igneous silicate spheroids, called chondrules (except in C1 type). The non-chondritic meteorites are differentiated objects and broadly classified based on their primary composition into Achondrites (silicate), Stony-Irons (silicate and metal) and Irons (metal). The ordinary chondrites are further sub-divided on the basis of their chemical composition into H, L and LL depending on their metallic content. Van Schmus & Wood (1967) introduced a secondary classification scheme that provides a guide to the degree of thermal or aqueous alteration suffered by chondrites (Van Schmus & Wood 1967). According to this, chondrites are divided into petrographic grade 1 through 6, with increasing number representing an increasing degree of chemical equilibrium and textural recrystallisation, presumably due to thermal metamorphism. Type 3 chondrites are the least altered (unequilibrated) while type 6 are the most altered (equilibrated). Type 1 represents higher degree of aqueous alteration compared to type 2, based largely on the abundance of hydrous silicates. The type 3 Unequilibrated Ordinary Chondrites (UOCs) are further divided into ten sub-types ranging from 3.0-3.9 based on the thermo-luminescence sensitivity of minerals (feldspar series) present, which is an indicator of the degree of crystallization (Sears et al., 1991). Of late, various other techniques for classification of unequilibrated chondrites have also been proposed based on the organic content or deviation in the chromium oxide composition in olivine as indicators of thermal or aqueous alteration suffered by UOCs (Brearley 2005; Grossman & Brearley 2005; Bonal et al., 2006; Bonal et al., 2007).

Isotopic studies of early solar system objects to infer about the early evolution of the solar system will be meaningful only if the analyzed objects have acted as a closed system and did not suffer any secondary thermal or other (e.g. shock) effects that may alter the pristine isotope records. The Ca-Al-rich refractory Inclusions (CAIs) are generally considered best choice for such a study. However, as noted in the Introduction (Chapter1), studies of Fe-Ni isotope systematics in CAIs are difficult both due to absence of phases with high Fe/Ni and possible intrinsic presence of nuclear anomalies in Fe group elements. Chondrules in UOCs of low petrologic type host phases (olivine and pyroxene) with relatively high Fe/Ni ratio and could be suitable for such a study. Extensive studies of Al-Mg isotope systematics have already been done in UOC chondrules and the presence of phases with high Fe/Ni makes them suitable for a combined study of Al-Mg and Fe-Ni isotope systematics, the primary objective of this thesis work.

Three unequilibrated ordinary chondrites (UOCs), Semarkona (LL 3.0), LEW 86134 (L 3.0) and Y791324 (L 3.1) were identified for the present study due to their low petrologic type suggesting that they have not experienced temperature in excess of 250°C during their residence in their parent asteroids (Huss et al., 2006) and thus should retain pristine isotope records. A description of these UOCs and the chondrules in them selected for studies of isotope records along with representative electron probe micro-analyser (EPMA) data for the phases in Chondrules analyzed are presented here.

3.1 Semarkona

It is one of the most pristine UOCs, that fell in Chhindwara district of Madhya Pradesh in 1940. A total mass of 692 gram was recovered in the form of two pieces. A thin section and a small piece of this meteorite used in this study was provided by the Geological Survey of India, Calcutta. This UOC belongs to type LL of lowest petrologic grade (LL3.0) and have not experienced any shock through out its evolutionary history. Studies of matrix in Semarkona (Alexander et al., 1989) and radial pyroxene and cryptocrystalline chondrules (Grossman et al., 2000) in it provide evidences that it may have suffered mild aqueous alteration. Bulk sample of Semarkona have not experienced thermal metamorphism (events) greater than 250°C

in its parent body (Alexander et al., 1989; Huss et al., 2006). Its pristine character and presence of abundant porphyritic, large ferromagnesian chondrules make it a suitable choice for the present study. From the thin section containing more than seventy chondrules, eleven chondrules were selected for detail of petrography and mineralogy studies to check their suitability for Fe-Ni and Al-Mg isotope studies. In addition, five chondrules from twenty one handpicked chondrules and fragments were also selected for detail petrologic study. Fig 3.1 to 3.2 show representative backscattered images of chondrules from Semarkona analyzed in this study. The classification of the chondrules to various groups such as porphyritic olivine (PO), porphyritic olivine pyroxene (POP), porphyritic pyroxene (PP), Bar (B), Radial (R) etc. are based on their textures and mineralogic properties given in Table 3.1

3.2 Lewis Hill 86314 (Lew 86314)

LEW 86314 is an unequilibrated ordinary chondrite belonging to type L of lowest petrologic grade (L3.0) and is a “find” from the Lewis Hill region of the Antarctica cold desert. A total mass of 29.8 gram was found and a thin section was provided by National Institute of Polar Studies, Tokyo, Japan for this study. Out of about fifty chondrules, a barred olivine, a radial pyroxene and two porphyritic olivine chondrules present in the thin section were selected for this study (Table 3.1).

3.3 Yamato Hill 791324 (Y 791324)

A thin section of this UOC belonging to type L of petrologic grade 1 (L3.1) and collected in the Yamato Hill region of Antarctica was provided by the National Institute of Polar Studies, Tokyo, Japan. Eight chondrules of different morphological types, out of close to forty chondrules in this section, were selected for this study (Table 3.1).

Representative backscattered electron images of selected chondrules obtained by using an EPMA (Cameca SX100) are shown in Fig. 3.1-3.4.

Table 3.1 Chondrules selected for isotope studies

Semarkona Thin section			
Chondrule #	Texture	Mineralogic type	Compositional type
Sem Ch#1	Porphyritic	PP	IB
Sem Ch#2	Porphyritic	PP	IIB
Sem Ch#20	Porphyritic	POP	IIAB
Sem Ch#21	Porphyritic	POP	IIAB
Sem Ch#28	Barred	BO	IIA
Sem Ch#29	Porphyritic	POP	IIAB
Sem Ch#36	Porphyritic	PP	IB
Sem Ch#39	Barred	BP	IIB
Sem Ch#40	Radial	RP	IB
Sem Ch#4	Porphyritic	PO	IIA
Sem Ch#43	Barred	BP	IB

Semarkona Piece			
Sem C#3	Porphyritic	POP	IIA
Sem C#8	Porphyritic	PO	IIA
Sem C#18	Barred	BP	IIAB
Sem C#21	Fragment	PO	IIA
Sem C#1	Barred	BP	IB

LEW 86134 L 3.0 Thin section			
Chondrule #	Texture		Compositional type
Lew Ch#36	Barred	BO	IIA
Lew Ch#37	Radial	RP	IIB
Lew Ch#39	Porphyritic	PO	IIA
Lew Ch#40	Porphyritic	PO	IIA

Y791324 L3.1 Thin section			
Chondrule #	Texture		Compositional type
Y791324 Ch#8	Porphyritic	POP	IIA
Y791324 Ch#3	Porphyritic	POP	IIAB
Y791324 Ch#6	Porphyritic	POP	IIAB
Y791324 Ch#13	Barred	BP	IA
Y791324 Ch#15	Radial	RP	IB
Y791324 Ch#14	Barred	BP	IIB
Y791324 Ch#12	Barred	BP	IIB

Porphyritic Olivine (PO); Porphyritic Pyroxene (PP); Porphyritic Olivine Pyroxene (POP); Barred Olivine (BO); Barred Pyroxene (BP); Radial Pyroxene (RP)

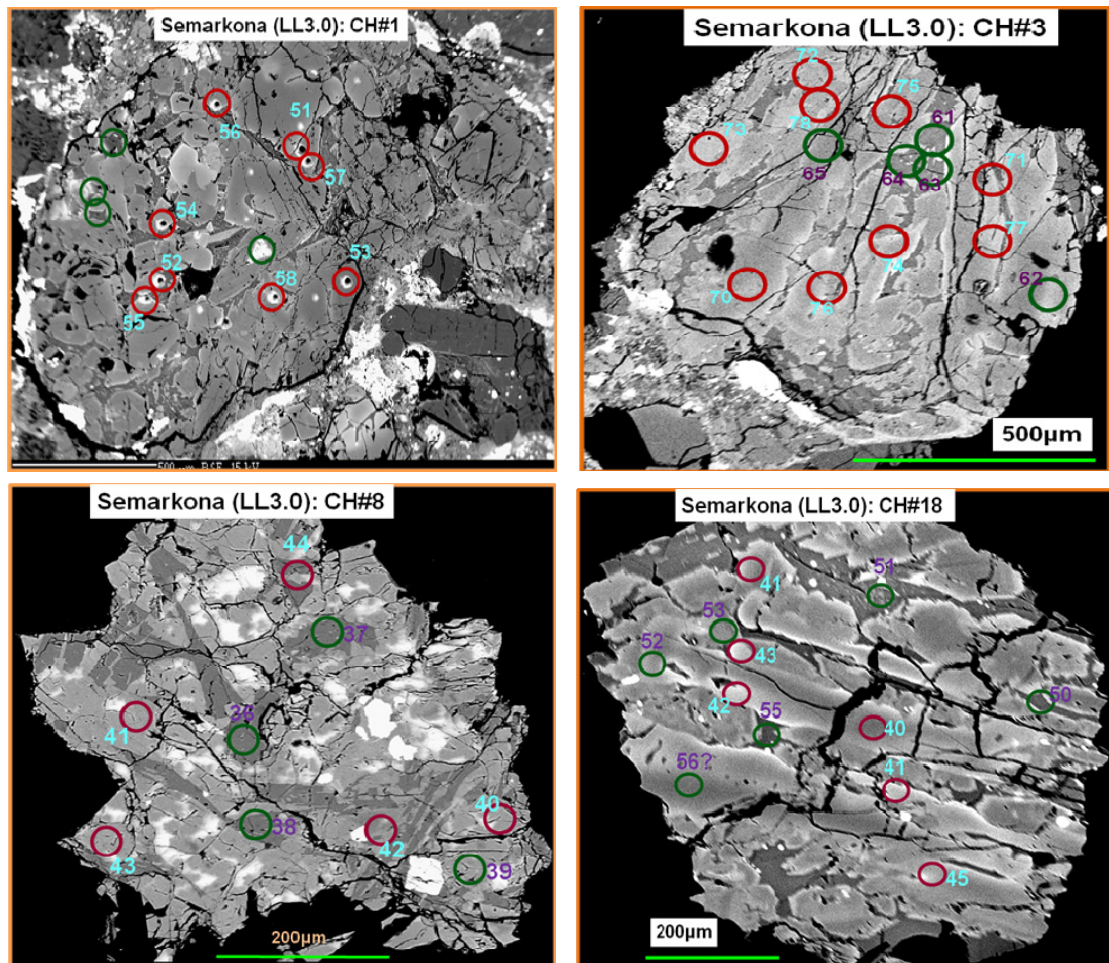


Fig. 3.1 Back scattered electron images of selected Semarkona chondrules. Red circles indicate regions analysed for Fe-Ni isotope systematics while green circles indicate regions analysed for Al-Mg isotope systematics in this study.

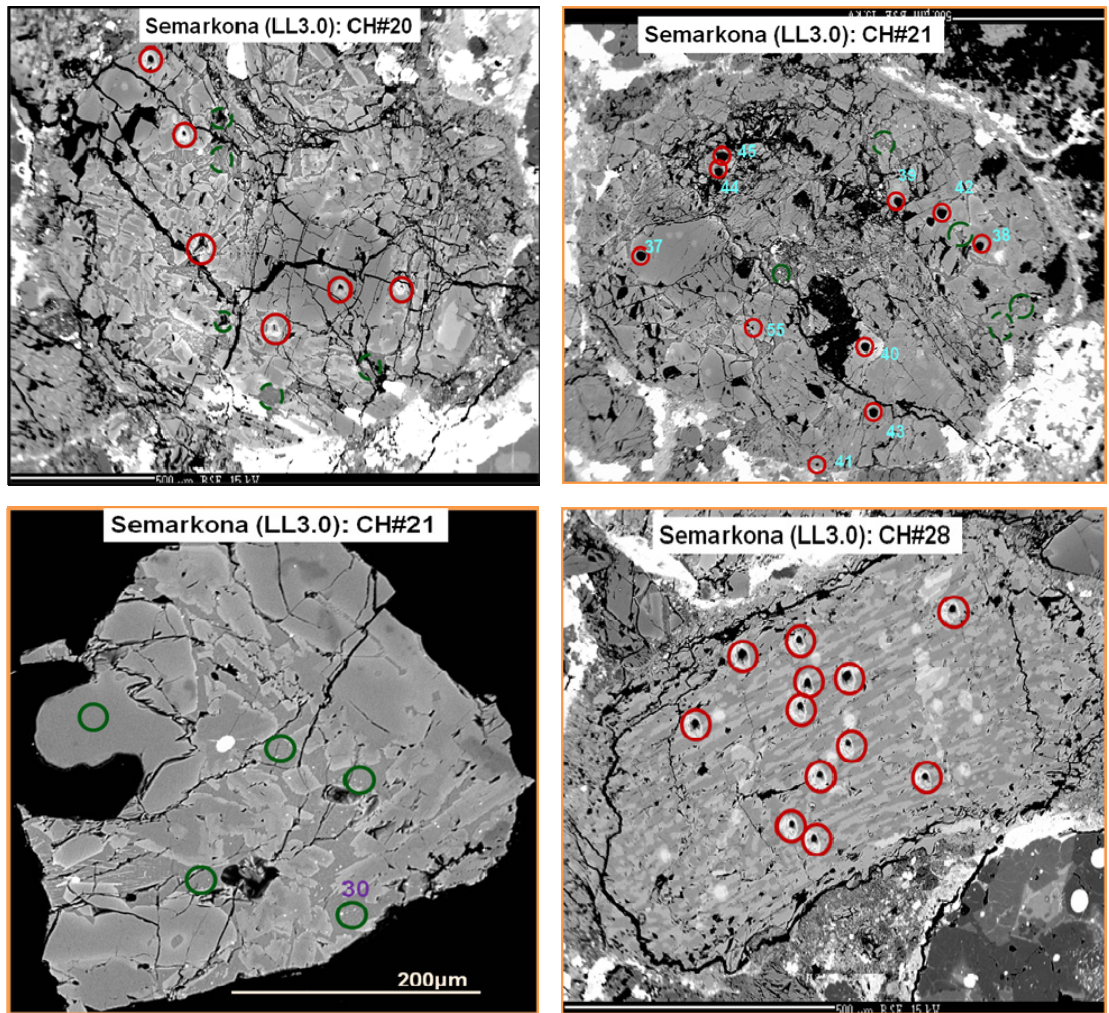


Fig. 3.2 (cont'd) Back scattered electron images of selected Semarkona chondrules. Red circles indicate regions analysed for Fe-Ni isotope systematics while green circles indicate regions analysed for Al-Mg isotope systematics in this study.

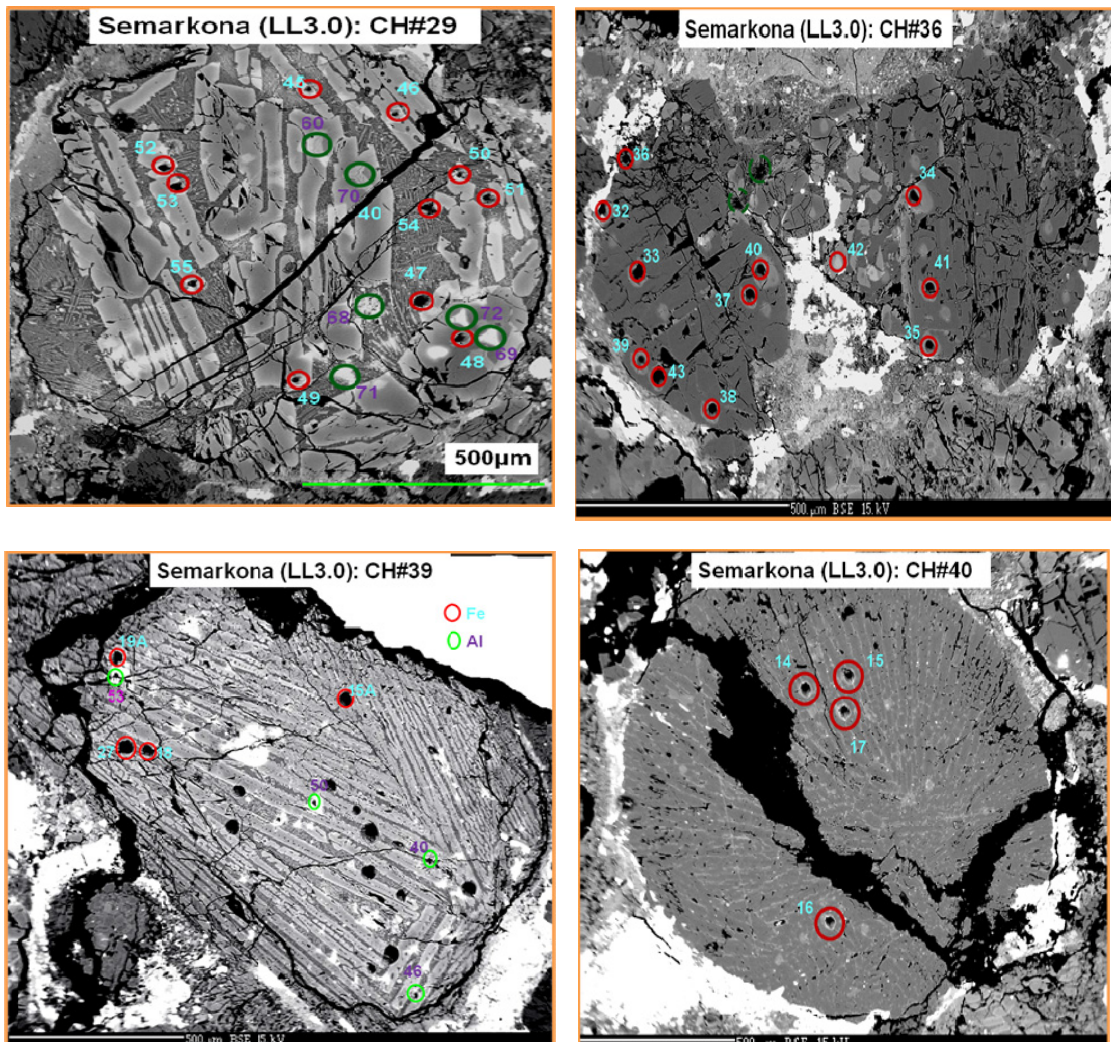


Fig. 3.2 (cont'd) Back scattered electron images of selected Semarkona chondrules. Red circles indicate regions analysed for Fe-Ni isotope systematics while green circles indicate regions analysed for Al-Mg isotope systematics in this study.

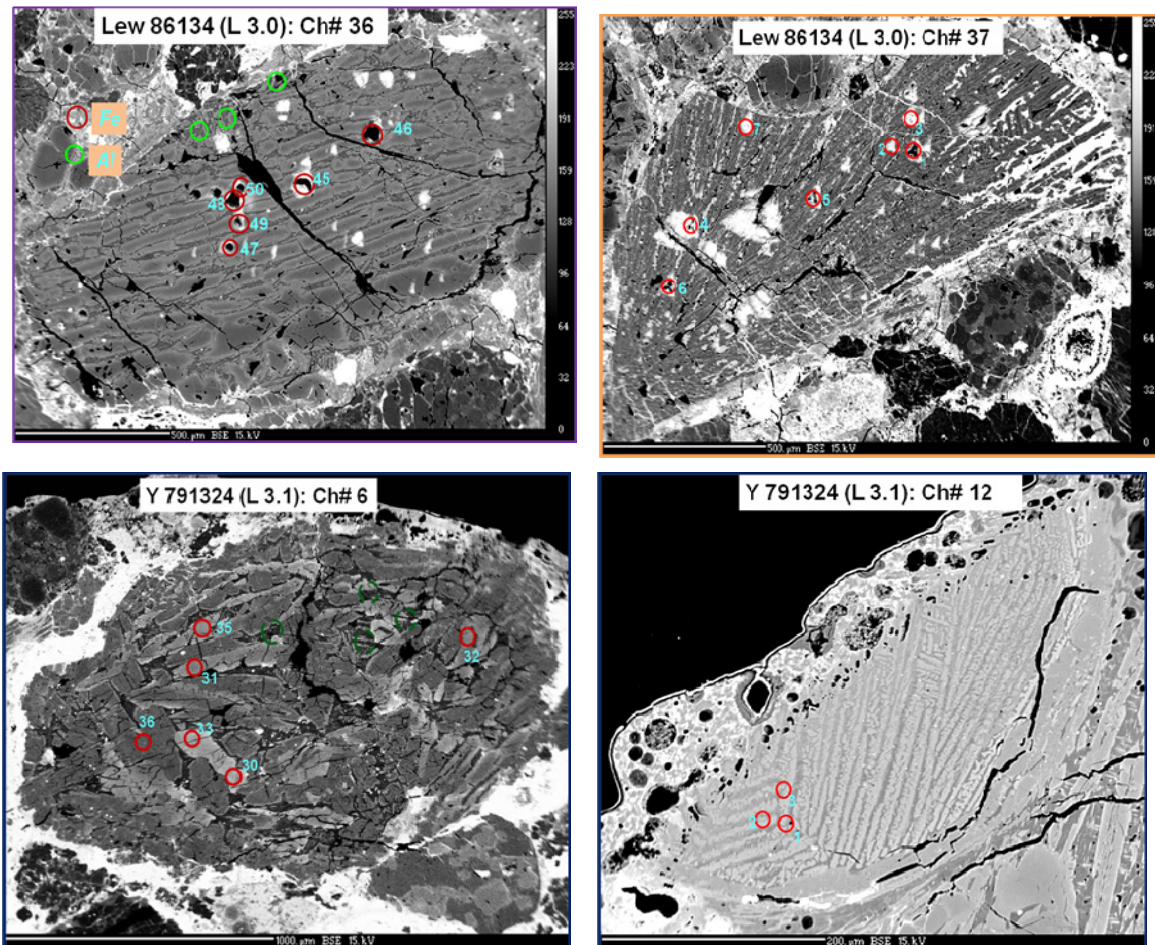


Fig. 3.4 Back scattered electron images of selected chondrules from LEW 86134 and Y791324 analysed in the present study. Red and green circles indicate regions analysed for Fe-Ni and Al-Mg isotope systematics respectively.

3.4 EPMA Studies of UOC Chondrules

Microscopic and petrographic observations as well as compositional studies of the selected chondrules in the three thin sections of the UOCs, as well as polished section of the four hand-picked chondrules from a sample of Semarkona, were carried out to identify chondrules that may be suitable for isotope studies. X-ray elemental maps of Fe, Al, Ca, and Mg for the chondrules were obtained using a focused $\sim 2 \mu\text{m}$, 70 nA e^- beam accelerated to 15kV and operated in the raster mode to map the whole chondrule. Intensities of Fe, Al, Ca X-rays were measured using LPET (Large Pentaery thristol), TAP (Thallium acid phthalate), LIF (lithium Fluoride) crystals, respectively, attached to the spectrometer, while Mg signal was measured simultaneously using EDX. Representative X-ray elemental image of one of the chondrules (LEW #36) is shown in Fig. 3.5.

Quantitative analysis of potential Fe-rich and Al-rich areas were carried out in WDX mode to find suitable phase with high Fe/Ni or Al/Mg for isotopic analysis. For WDX measurement, a 20nA, focused, $\sim 1 \mu\text{m}$ e^- beam accelerated to 15kV was used. Representative data set for chondrules analysed in this study are provided in Table 3.2-3.9. The composition of the phases are expressed as Fo (Mg_2SiO_4) for forsteritic olivine, Wo (CaSiO_3) for wollastonite, En (MgSiO_3) for enstatite, Fs (FeSiO_3) for ferrosilicic pyroxene. Reference terrestrial standards were analyzed before each session of analysis to ensure proper instrument performance.

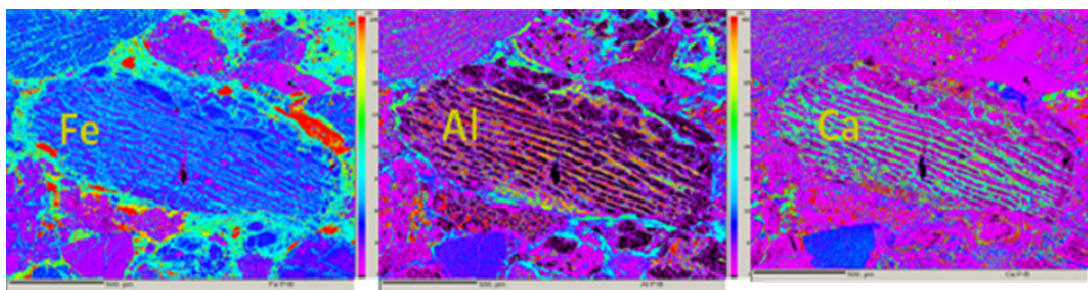


Fig. 3.5. Fe, Al and Ca X-ray elemental map of LEW 86134 Ch#36.

Table 3.2 Chemical composition of Semarkona (LL 3.0) chondrule

Analysis No.	Chondrule#1			Chondrule#2		
	1	2	3	1	2	3*
Na ₂ O	0.14	0.04	4.04	0.03	0.02	2.95
SiO ₂	57.22	58.32	66.48	54.82	54.58	0.01
MgO	34.58	36.20	2.11	26.74	27.09	71.53
Al ₂ O ₃	0.39	0.65	13.65	0.27	0.15	22.51
P ₂ O ₅	nd	nd	0.13	nd	0.01	0.04
K ₂ O	0.04	0.01	0.45	nd	0.01	0.70
CaO	0.37	0.14	7.58	0.73	0.49	0.12
TiO ₂	0.03	0.01	0.54	0.03	0.03	0.04
Cr ₂ O ₃	0.57	0.54	0.20	0.87	0.75	0.02
MnO	0.38	0.19	0.35	0.52	0.80	00
FeO	6.47	5.47	4.97	15.20	15.39	0.30
NiO	nd	nd	nd	0.02	nd	nd
Total	100.17	101.57	100.49	99.21	99.32	98.23
Phase	Pyroxene	Pyroxene	Glass	Pyroxene	Pyroxene	Glass
Composition	En90Wo1Fs9	En92Fs8		En75Wo1Fs24	En75Wo1Fs25	

Analysis No.	Chondrule#3			Chondrule#8		
	1	2	3	1	2	3
Na ₂ O	0.02	0.13	1.76	0.03	0.04	0.08
SiO ₂	36.51	35.91	69.60	38.59	51.87	46.27
MgO	31.29	27.24	0.50	40.84	21.86	0.66
Al ₂ O ₃	0.12	0.26	15.87	0.03	2.36	31.48
P ₂ O ₅	0.01	nd	0.30	nd	0.05	0.32
K ₂ O	nd	nd	0.84	nd	0.01	0.01
CaO	0.28	0.36	0.76	0.25	5.09	19.13
TiO ₂	0.03	0.03	0.55	0.05	0.53	0.03
Cr ₂ O ₃	0.29	0.42	nd	0.37	0.46	nd
MnO	0.83	0.85	0.18	0.28	0.26	0.03
FeO	32.10	36.24	6.99	20.56	16.65	1.00
NiO	nd	0.02	0.06	nd	nd	nd
Total	101.48	101.47	97.41	100.99	99.18	99.01
Phase	Olivine	Pyroxene	Glass	Olivine	Pyroxene	Glass
Composition	Fa37	En77Wo2Fs21		Fa22	En63Wo10Fs27	

Table 3.3 Chemical composition of Semarkona (LL 3.0) chondrule

Analysis No.	Chondrule# 18			Chondrule#20		
	1	2	3	1	2	3*
Na ₂ O	0.04	0.10	0.94	0.05	0.06	2.13
SiO ₂	37.97	54.84	66.02	37.12	52.74	0.38
MgO	37.33	27.35	0.13	36.65	23.81	65.36
Al ₂ O ₃	0.01	0.26	14.09	0.01	0.38	12.18
P ₂ O ₅	nd	0.02	0.27	0.02	nd	0.06
K ₂ O	0.02	0.03	0.71	0.03	0.01	0.76
CaO	0.16	1.03	1.21	0.01	0.77	4.14
TiO ₂	nd	0.05	0.60	nd	0.01	0.42
Cr ₂ O ₃	0.43	0.86	0.03	0.47	0.82	0.03
MnO	0.56	0.73	0.22	0.77	0.90	11.28
FeO	23.85	15.94	11.95	24.49	18.78	0.43
NiO	nd	nd	0.10	nd	0.17	nd
Total	100.37	101.20	96.25	99.70	98.46	97.14
Phase	Olivine	Pyroxene	Glass	Olivine	Pyroxene	Glass
Composition	Fa26	En74Wo2Fs24		Fa27	En68Wo2Fs30	

Chondrule#21A	1	2	3	Chondrule21	2	3*
Na ₂ O	0.16	0.40	0.79	0.04	0.06	7.85
SiO ₂	39.58	54.50	71.17	38.16	56.76	0.71
MgO	46.59	29.37	0.64	38.54	31.75	62.34
Al ₂ O ₃	0.02	0.30	16.23	0.07	0.30	18.81
P ₂ O ₅	nd	0.01	0.06	nd	0.01	0.25
K ₂ O	0.03	0.02	0.92	0.02	0.01	0.29
CaO	0.10	2.21	0.91	0.20	0.25	3.81
TiO ₂	0.03	0.05	0.51	nd	0.06	0.28
Cr ₂ O ₃	0.52	1.08	0.01	0.58	0.94	0.56
MnO	0.62	0.96	0.28	0.55	0.29	1.87
FeO	11.61	8.70	5.39	21.13	11.18	0.04
NiO	nd	nd	nd	nd	0.13	nd
Total	99.24	97.60	96.90	99.30	101.73	96.81
Phase	olivine	Pyroxene	Glass	Olivine	Pyroxene	Glass
Composition	Fa12	En75Wo1Fs25		Fa24	En83Fs16	

Table 3.4 Chemical composition of Semarkona (LL 3.0) chondrule

Analysis No.	Chondrule28			Chondrule29		
	1	2	3	1	2	3
Na ₂ O	0.05	0.05	0.10	0.01	nd	1.09
SiO ₂	37.56	37.87	52.92	36.71	38.47	73.76
MgO	36.54	36.79	24.60	32.98	41.64	2.16
Al ₂ O ₃	0.03	0.01	2.37	0.02	0.03	9.84
P ₂ O ₅	nd	0.05	0.02	nd	0.03	0.05
K ₂ O	nd	nd	0.06	nd	0.01	0.93
CaO	0.20	0.16	3.44	0.19	0.11	2.83
TiO ₂	0.04	0.02	0.37	0.02	nd	0.37
Cr ₂ O ₃	0.27	0.19	0.52	0.75	0.50	0.39
MnO	0.28	0.33	0.30	0.70	0.34	0.14
FeO	24.32	23.46	14.25	27.82	18.08	8.36
NiO	nd	nd	nd	nd	nd	0.12
Total	99.28	98.91	98.94	99.18	99.20	100.04
Phase Composition	Olivine Fa27	Olivine Fa26	Glass	Olivine Fa32	Olivine Fa20	Glass

Analysi s No	Chondrule36			Chondrule39		
	1	2	3*	1	2	3
Na ₂ O	nd	nd	8.78	0.38	0.71	0.20
SiO ₂	41.57	58.21	0.23	41.83	52.32	54.05
MgO	52.12	35.65	60.76	38.39	18.50	23.63
Al ₂ O ₃	0.01	0.35	22.47	0.30	0.61	1.80
P ₂ O ₅	0.02	0.06	0.04	0.02	0.15	0.10
K ₂ O	0.01	0.01	0.28	0.04	0.03	nd
CaO	0.06	0.38	5.06	1.83	13.13	11.63
TiO ₂	nd	0.03	0.11	0.02	0.14	0.36
Cr ₂ O ₃	0.39	0.60	0.01	0.75	1.98	1.35
MnO	0.33	0.49	0.28	0.64	0.85	1.26
FeO	5.80	4.35	0.04	17.71	11.97	5.20
NiO	nd	nd	nd	nd	0.01	0.02
Total	100.28	100.06	98.03	101.91	100.38	99.61
Phase Compos	Olivine Fa6	Pyroxene En93Wo1Fs	Glass	Olivin Fa21	Pyroxene En53Wo27F	Pyroxene En68Wo24

Table 3.5 Chemical composition of Semarkona (LL 3.0) chondrule

Analysis No.	Chondrule40				
	1	2	3	5	6
Na ₂ O	0.07	0.05	0.10	2.95	2.47
SiO ₂	54.76	56.65	54.34	62.26	62.25
MgO	29.59	35.06	27.41	1.58	2.93
Al ₂ O ₃	1.34	0.58	1.06	19.01	17.84
P ₂ O ₅	0.03	0.01	0.08	0.03	0.13
K ₂ O	0.03	0.05	nd	0.45	0.40
CaO	4.37	0.23	7.84	6.30	6.66
TiO ₂	0.13	0.05	0.19	0.56	0.43
Cr ₂ O ₃	1.78	0.88	1.70	0.02	0.25
MnO	1.22	0.43	1.68	0.52	0.48
FeO	4.83	4.21	4.15	3.41	3.54
NiO	nd	0.06	0.03	0.05	0.04
Total	98.13	98.26	98.56	97.12	97.41
Phase	Pyroxene	Pyroxene	Pyroxene	Glass	Glass
Composition	En83Wo9Fs8	En93Wo0Fs6	En77Wo16Fs7		

Table 3.6 Chemical composition of LEW 86134 (L 3.0) chondrule

Analysis	Chondrule # 36			Chondrule # 37		
	1	2	3*	1	5	6
Na ₂ O	0.02	nd	5.50	0.21	0.44	0.20
SiO ₂	39.81	40.15	0.51	51.55	52.94	53.63
MgO	45.19	45.57	70.36	19.11	19.96	26.39
Al ₂ O ₃	0.02	0.01	11.61	3.38	3.22	0.77
P ₂ O ₅	0.03	nd	0.01	0.15	0.12	0.05
K ₂ O	nd	0.01	1.09	nd	0.05	nd
CaO	0.10	0.10	0.67	11.33	5.96	0.91
TiO ₂	nd	0.01	0.43	0.30	0.29	0.04
Cr ₂ O ₃	0.45	0.45	0.01	1.05	0.86	0.66
MnO	0.44	0.39	6.44	0.79	0.75	0.73
FeO	14.53	14.46	0.39	13.11	14.57	17.23
NiO	nd	nd	nd	nd	nd	0.63
Total	100.58	101.14	97.00	100.99	99.15	101.22
Phase	Olivine	Olivine	Glass	Pyroxene	Pyroxene	Pyroxene
Composition	Fa15	Fa15		En55Wo24Fs21	En62Wo13Fs25	En71Wo2Fs26

Table 3.7 Chemical composition of LEW 86134 (L 3.0) chondrule

Analysis	Chondrule # 39					
	1	2	3	4	5	6
Na ₂ O	0.01	0.08	0.07	0.04	6.66	0.01
SiO ₂	37.65	55.42	54.22	37.70	69.25	55.3
MgO	34.22	27.13	24.97	30.75	0.86	28.0
Al ₂ O ₃	0.02	0.30	0.46	nd	15.42	0.3
P ₂ O ₅	0.05	0.02	nd	0.04	0.09	nd
K ₂ O	0.01	nd	0.02	nd	0.05	nd
CaO	0.31	1.24	1.73	0.36	0.20	1.7
TiO ₂	0.03	0.04	0.05	nd	0.27	0.09
Cr ₂ O ₃	0.21	0.97	1.01	0.23	0.02	3.0
MnO	0.71	0.56	0.64	0.87	0.12	0.6
FeO	28.49	16.07	17.61	33.93	6.56	12.9
NiO	nd	nd	0.01	0.06	0.08	0.02
Total	101.70	101.82	100.77	103.98	99.58	100.2
Phase Composition	Olivine Fa32	Pyroxene En73Wo2Fs24	Pyroxene En69Wo3Fs27	Olivine Fa38	Glass	Glass

Table 3.8 Chemical composition of Y791324 (L 3.1) chondrule

Analysis No.	Chondrule# 6			Chondrule# 8		
	1	2	3*	Analysis	4	5
Na ₂ O	0.01	0.05	9.03	0.04	0.22	4.22
SiO ₂	36.74	37.84	63.66	39.49	53.72	69.17
MgO	33.94	35.81	0.75	43.24	25.88	4.46
Al ₂ O ₃	0.02	0.01	14.86	nd	0.70	6.34
P ₂ O ₅	0.01	0.03	0.16	0.04	0.02	0.11
K ₂ O	nd	nd	0.08	nd	nd	0.05
CaO	0.16	0.22	2.01	0.14	1.54	6.33
TiO ₂	0.02	nd	0.51	nd	0.06	0.34
Cr ₂ O ₃	0.27	0.11	0.07	0.32	1.23	0.48
MnO	0.68	0.74	0.16	0.40	0.83	0.33
FeO	27.64	25.65	7.1	16.38	15.01	7.05
NiO	nd	nd	nd	0.07	0.14	0.27
Total	99.49	100.46	98.37	100.11	99.34	99.12
Phase Composition	Olivine Fa31	Olivine Fa29	Glass	Olivine Fa18	Pyroxene En73Wo3Fs23	Glass

Table 3.9 Chemical composition of Y791324 (L 3.1) chondrule

Analysis	Chondrule # 12				
	1	2	3	4	5
Na ₂ O	0.14	0.96	1.46	5.81	3.27
SiO ₂	39.39	51.94	53.75	64.62	63.61
MgO	41.37	33.69	10.70	3.61	2.38
Al ₂ O ₃	0.12	2.78	2.18	8.80	7.19
P ₂ O ₅	nd	0.06	0.16	0.12	0.16
K ₂ O	0.01	0.75	0.03	0.08	0.06
CaO	0.06	1.07	11.35	3.03	5.57
TiO ₂	0.01	0.08	0.29	0.27	0.43
Cr ₂ O ₃	0.33	0.50	1.19	0.19	0.28
MnO	0.61	0.39	0.84	0.25	0.45
FeO	19.27	10.39	18.25	10.39	15.58
NiO	nd	0.01	0.13	0.29	nd
Total	101.31	102.61	100.33	97.46	98.97
Phase Composition	Olivine Fa21	Pyroxene En84Wo2Fs14	Pyroxene En37Wo28Fs35	Pyroxene En31Wo19Fs50	Pyroxene En16Wo26Fs58

CHAPTER 4: RESULTS

Chondrules from UOCs of low petrologic groups (3.0 and 3.1) analyzed in this study for their Fe-Ni and Al-Mg isotope records are expected to retain their pristine isotope records. The major constituents of UOC chondrules are ferromagnesian silicate minerals, olivine $[(\text{Fe},\text{Mg})_2\text{SiO}_4]$ and pyroxene $[\text{Ca}(\text{Fe},\text{Mg})\text{Si}_2\text{O}_6]$, apart from Fe-Ni metal, sulphide, occasional feldspathic phases and glassy silicate mesostasis. Fe-Ni isotope study was carried out in silicate phases (olivine/pyroxene) as they are less susceptible to disturbances by thermal events in comparison to the other Fe-rich phases such as FeS that are also present in chondrules. Al-Mg isotopic study was carried out mainly in the silicate-rich glassy mesostases that are usually rich in Na, Al, Ca and K relative to bulk chondritic composition. It is difficult to find regions with high Fe/Ni or Al/Mg within chondrules; however we have been successful in finding a reasonable number of such chondrules during this study. We note here that so far only in one chondrule combined data for both Fe-Ni and Al-Mg isotope systematics, that revealed presence of ^{60}Fe and ^{26}Al at the time of its formation, have been reported. The experimental procedures described in Chapter 3 were adopted for studies of Fe-Ni and Al-Mg isotope systematics. Here we present the results obtained in this study, first for Fe-Ni isotopes system, and then for Al-Mg system in Semarkona, LEW 86134 and Y 791324.

4.1 Fe-Ni Isotope Systematics

4.1.1 Semarkona

Fifteen chondrules, eleven from the Semarkona thin section and four from the hand-picked sample of chondrules, were analysed. Nine chondrules have resolved excesses at 2σ level and another one at 1σ while upper limit values could be obtained for other chondrules. The results are presented in Tables 4.1 and the corresponding three isotope plots of $^{60}\text{Ni}/^{62}\text{Ni}$ vs. $^{56}\text{Fe}/^{62}\text{Ni}$ are shown in Fig. 4.1-4.6. The inferred initial values for $^{60}\text{Fe}/^{56}\text{Fe}$ based on isochron approach (discussed in Chapter 1) are also shown in these figures.

Table 4.1 Fe-Ni isotope data for chondrules from Semarkona (LL 3.0)

Chd	Phases	$^{56}\text{Fe}/^{62}\text{Ni}$		$^{60}\text{Ni}/^{62}\text{Ni}$		$(^{60}\text{Fe}/^{56}\text{Fe})_i [\pm 2\sigma]$
1	Olivine	20956	\pm	119	7.29	\pm 0.01
	Pyroxene	67223	\pm	2419	7.26	\pm 0.02
	Pyroxene	108105	\pm	6329	7.32	\pm 0.02
	Pyroxene	176502	\pm	3107	7.31	\pm 0.02
	Pyroxene	203423	\pm	2648	7.42	\pm 0.03
	Pyroxene	277809	\pm	15625	7.35	\pm 0.02
	Pyroxene	350395	\pm	1563	7.29	\pm 0.05
	Pyroxene	400517	\pm	2185	7.47	\pm 0.06
	Pyroxene	469546	\pm	2902	7.48	\pm 0.07 $(2.30 \pm 1.3) \times 10^{-7}$
2	Olivine	2320	\pm	3	7.26	\pm 0.01
	Olivine	21708	\pm	19	7.25	\pm 0.01
	Pyroxene	146470	\pm	40612	7.27	\pm 0.03 $(1.10 \pm 3.6) \times 10^{-7}$
3	Olivine	20453	\pm	283	7.28	\pm 0.01
	Olivine	76503	\pm	8926	7.30	\pm 0.01
	Olivine	115626	\pm	13834	7.32	\pm 0.01
	Olivine	163521	\pm	11191	7.31	\pm 0.02
	Olivine	208629	\pm	547	7.26	\pm 0.03
	Olivine	236296	\pm	801	7.34	\pm 0.04
	Olivine	296480	\pm	953	7.42	\pm 0.04
	Olivine	434578	\pm	2732	7.43	\pm 0.07 $(3.2 \pm 1.8) \times 10^{-7}$
8	Olivine	19580	\pm	709	7.31	\pm 0.01
	Olivine	41555	\pm	1233	7.37	\pm 0.02
	Olivine	59037	\pm	1648	7.34	\pm 0.02
	Olivine	86393	\pm	799	7.28	\pm 0.04
	Olivine	109830	\pm	14717	7.37	\pm 0.03 $(7.7 \pm 11.0) \times 10^{-7}$
18	Olivine	20600	\pm	606	7.27	\pm 0.01
	Olivine	82930	\pm	4481	7.34	\pm 0.01
	Olivine	187915	\pm	23772	7.45	\pm 0.02
	Olivine	320218	\pm	1302	7.30	\pm 0.05 $(6.60 \pm 6.0) \times 10^{-7}$
20	Olivine	18598	\pm	186	7.29	\pm 0.02
	Olivine	60575	\pm	638	7.29	\pm 0.02
	Olivine	236593	\pm	25259	7.32	\pm 0.03
	Pyroxene	323399	\pm	17473	7.52	\pm 0.02
	Pyroxene	557905	\pm	4398	7.34	\pm 0.09 $(4.1 \pm 2.8) \times 10^{-7}$
21	Olivine	20913	\pm	17	7.27	\pm 0.01
	Olivine	101515	\pm	7303	7.32	\pm 0.01
	Olivine	181897	\pm	8394	7.29	\pm 0.05
	Pyroxene	209950	\pm	2778	7.34	\pm 0.05
	Pyroxene	252365	\pm	13066	7.44	\pm 0.06
	Pyroxene	314006	\pm	8200	7.51	\pm 0.16 $(4.8 \pm 2.8) \times 10^{-7}$

29	Olivine	18598	\pm	186	7.29	\pm	0.02	
	Olivine	66600	\pm	2621	7.22	\pm	0.02	
	Olivine	108689	\pm	17054	7.25	\pm	0.01	
	Pyroxene	142509	\pm	6704	7.28	\pm	0.01	
	Pyroxene	175657	\pm	10344	7.28	\pm	0.02	
	Pyroxene	218219	\pm	6872	7.30	\pm	0.02	
	Olivine	245085	\pm	33738	7.29	\pm	0.02	
	Olivine	431651	\pm	97335	7.43	\pm	0.04	
	Pyroxene	784299	\pm	19552	7.33	\pm	0.08	
	Pyroxene	945125	\pm	22707	7.27	\pm	0.06	
	Pyroxene	1258374	\pm	18016	7.34	\pm	0.10	$(1.97 \pm 1.50) \times 10^{-7}$
36	Pyroxene	259	\pm	0.2	7.21	\pm	0.01	
	Pyroxene	16695	\pm	2089	7.30	\pm	0.02	
	Pyroxene	35122	\pm	95	7.21	\pm	0.03	
	Pyroxene	50423	\pm	7134	7.35	\pm	0.06	
	Pyroxene	91391	\pm	5746	7.27	\pm	0.03	
	Pyroxene	115116	\pm	1628	7.42	\pm	0.07	
	Pyroxene	170591	\pm	2060	7.24	\pm	0.05	
	Pyroxene	201851	\pm	6221	7.34	\pm	0.07	
	Pyroxene	236513	\pm	3314	7.36	\pm	0.09	
	Pyroxene	264013	\pm	3395	7.31	\pm	0.07	$(5.2 \pm 4.2) \times 10^{-7}$
39	Pyroxene	128315	\pm	11185	7.23	\pm	0.05	
	Pyroxene	256200	\pm	16450	7.22	\pm	0.04	
	Pyroxene	458701	\pm	33401	7.32	\pm	0.05	
	Pyroxene	607232	\pm	6040	7.50	\pm	0.12	
	Pyroxene	731000	\pm	7800	7.41	\pm	0.13	
	Pyroxene	887500	\pm	34500	7.55	\pm	0.11	$(4.3 \pm 2.4) \times 10^{-7}$
40	Olivine	20120	\pm	210	7.29	\pm	0.01	
	Pyroxene	72950	\pm	21750	7.27	\pm	0.03	
	Pyroxene	363000	\pm	5100	7.27	\pm	0.13	
	Pyroxene	590000	\pm	11000	7.51	\pm	0.17	
	Pyroxene	724000	\pm	6000	7.40	\pm	0.07	
	Pyroxene	1018000	\pm	63000	7.45	\pm	0.13	$(1.6 \pm 1.5) \times 10^{-7}$

4.1.2 LEW 86134 (L 3.0)

Four chondrules from this meteorite were selected for Fe-Ni systematics study. Only two chondrules showed well resolved excess while in other two despite regions with high Fe concentration no regions with high Fe/Ni suitable for isotopic study could be found. Table 4.2 shows results from Fe-Ni isotopic study while Fig 4.4 and 4.5 shows the isochron diagram obtained in them.

Table 4.2 : Fe-Ni isotope data for chondrules from LEW 86134 (L 3.0)

Chd	Phases	$^{56}\text{Fe}/^{62}\text{Ni}$		$^{60}\text{Ni}/^{62}\text{Ni}$		$(^{60}\text{Fe}/^{56}\text{Fe})_i [\pm 2\sigma]$
36	Olivine	66000	\pm 400	7.36	\pm 0.05	
	Olivine	22117	\pm 441	7.25	\pm 0.01	
	Olivine	5569	\pm 1159	7.23	\pm 0.01	
	Olivine	279000	\pm 2200	7.48	\pm 0.07	
	Olivine	514000	\pm 7500	7.50	\pm 0.13	
	Olivine	206418	\pm 14165	7.30	\pm 0.02	
	Olivine	459052	\pm 38777	7.38	\pm 0.08	$(4.1 \pm 2.6) \times 10^{-7}$
37	Pyroxene	10743	\pm 77	7.32	\pm 0.02	
	Olivine	22117	\pm 441	7.25	\pm 0.01	
	Pyroxene	254890	\pm 5112	7.38	\pm 0.07	
	Pyroxene	379193	\pm 26593	7.52	\pm 0.04	
	Pyroxene	645800	\pm 10500	7.32	\pm 0.14	
	Pyroxene	969600	\pm 20400	7.51	\pm 0.19	$(4.9 \pm 3.8) \times 10^{-7}$

4.1.3 Y791324 (L3.1) Four chondrules in the thin section of this meteorite were selected but none of them showed resolved excess of ^{60}Ni . Table 4.3 shows results from Fe-Ni isotopic study while Fig 4.6 shows the isochron diagram obtained in them.

Table 4.3 : Fe-Ni isotope data for chondrules from Y791324 (L 3.1)

Chd	Phases	$^{56}\text{Fe}/^{62}\text{Ni}$		$^{60}\text{Ni}/^{62}\text{Ni}$		$(^{60}\text{Fe}/^{56}\text{Fe})_i [\pm 2\sigma]$
6	Olivine	18942	\pm 1016	7.29	\pm 0.01	
	Olivine	20124	\pm 121	7.30	\pm 0.01	
	Pyroxene	30885	\pm 4770	7.32	\pm 0.01	
	Olivine	54046	\pm 10924	7.30	\pm 0.01	
	Pyroxene	138668	\pm 569	7.39	\pm 0.05	$(5.4 \pm 10.8) \times 10^{-7}$
12	Pyroxene	18942	\pm 1016	7.29	\pm 0.01	
	Olivine	20124	\pm 121	7.30	\pm 0.01	
	Pyroxene	440957	\pm 42711	7.32	\pm 0.03	
	Pyroxene	587034	\pm 56221	7.37	\pm 0.04	$(9.5 \pm 10.6) \times 10^{-8}$

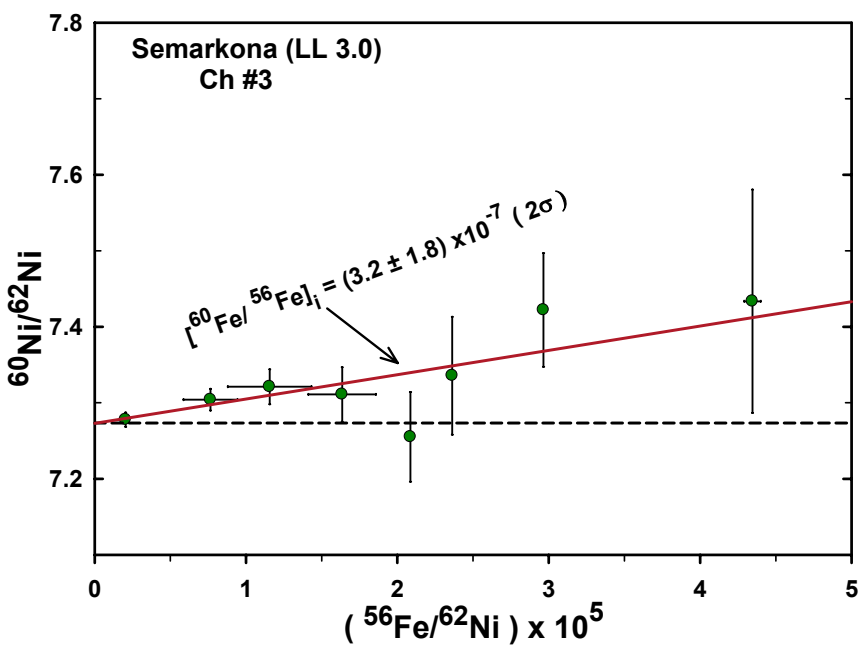
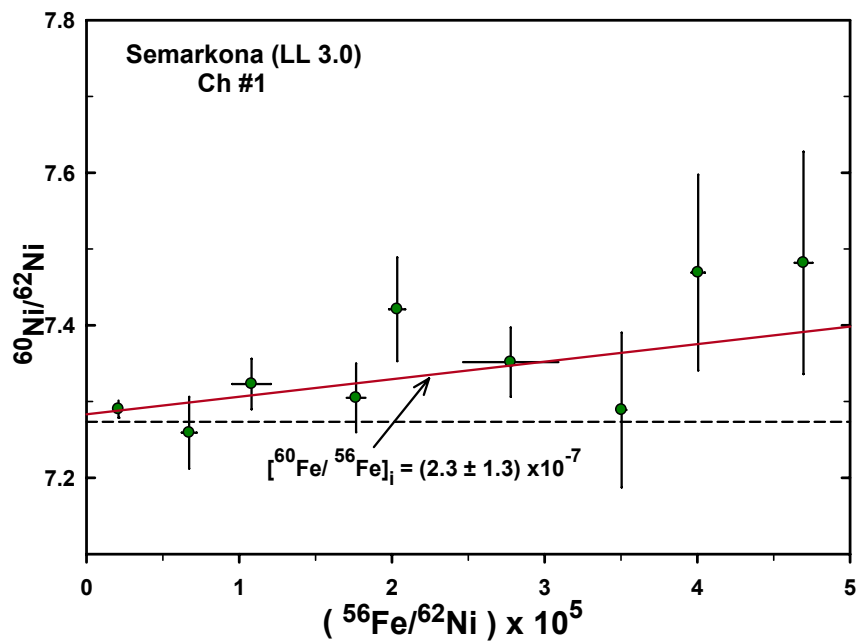


Fig. 4.1 Three isotope Fe-Ni plots for Semarkona chondrules # 1 and #3. The inferred initial ${}^{60}\text{Fe}/{}^{56}\text{Fe}$ is also shown. The dotted line is the reference value of ${}^{60}\text{Ni}/{}^{62}\text{Ni}$. Error bars 2σ .

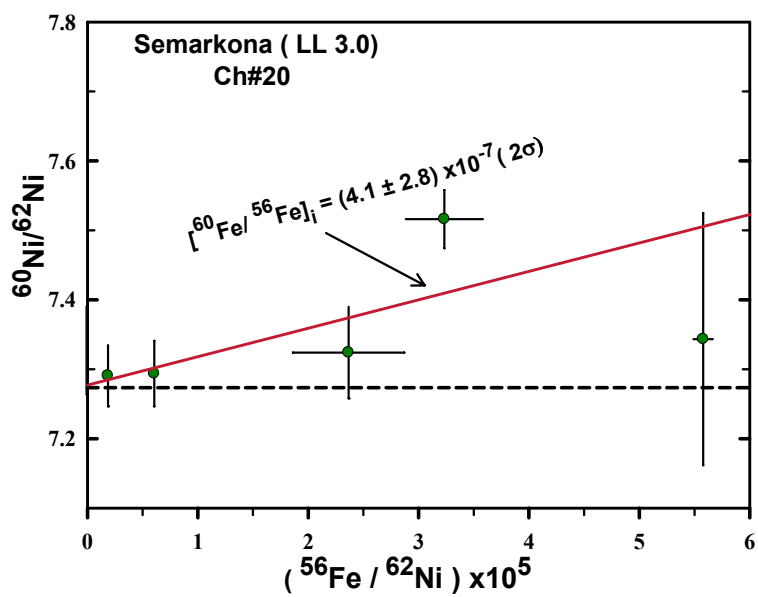
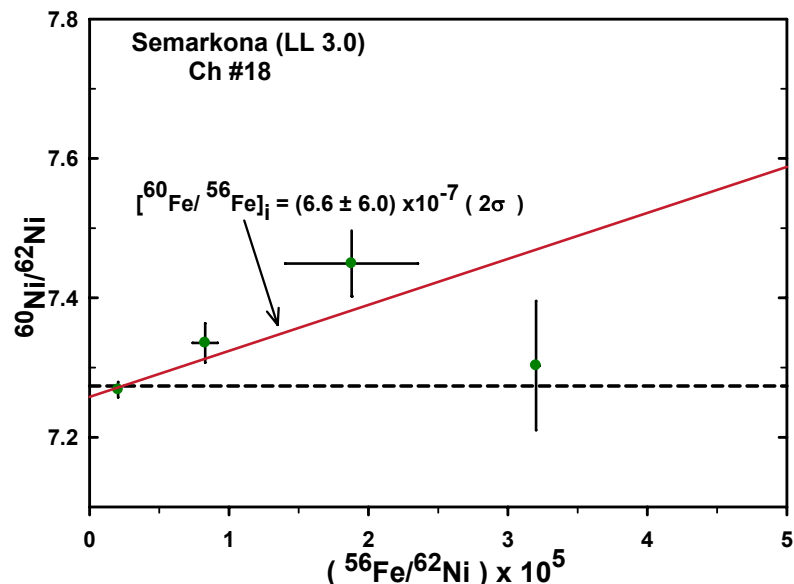


Fig. 4.2 Three isotope Fe-Ni plots for Semarkona chondrules # 18 and #20. The inferred initial ${}^{60}\text{Fe}/{}^{56}\text{Fe}$ is also shown. The dotted line is the reference value of ${}^{60}\text{Ni}/{}^{62}\text{Ni}$. Error bars 2σ .

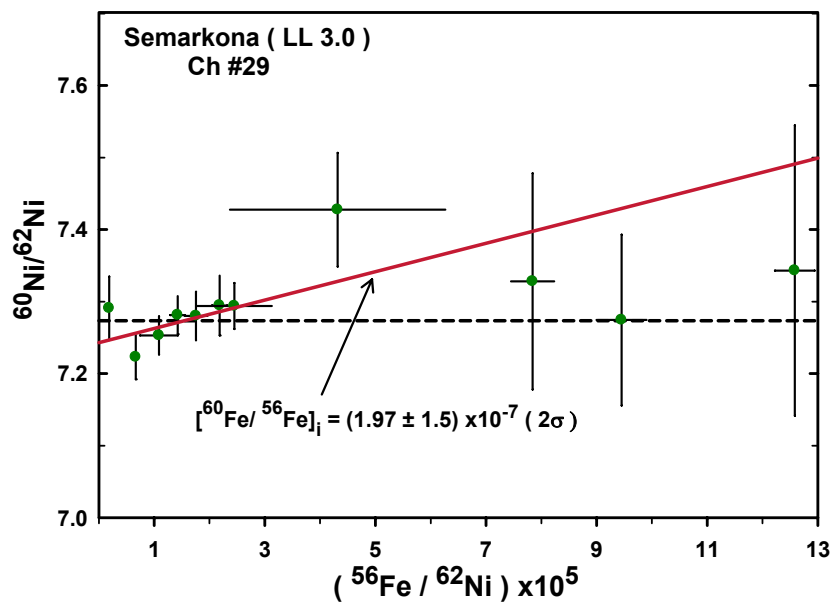
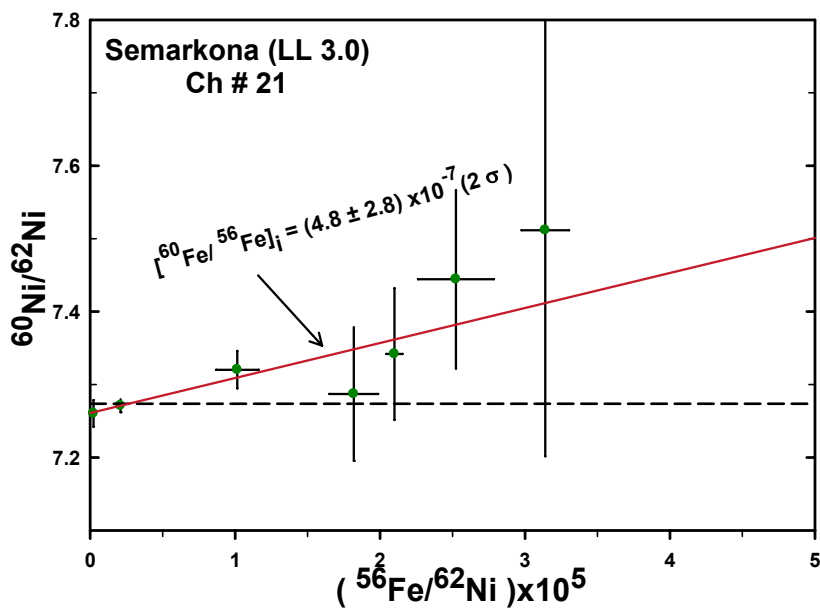


Fig. 4.3 Three isotope Fe-Ni plots for Semarkona chondrules # 21 and # 29. The inferred initial ${}^{60}\text{Fe}/{}^{56}\text{Fe}$ is also shown. The dotted line is the reference value of ${}^{60}\text{Ni}/{}^{62}\text{Ni}$. Error bars 2σ .

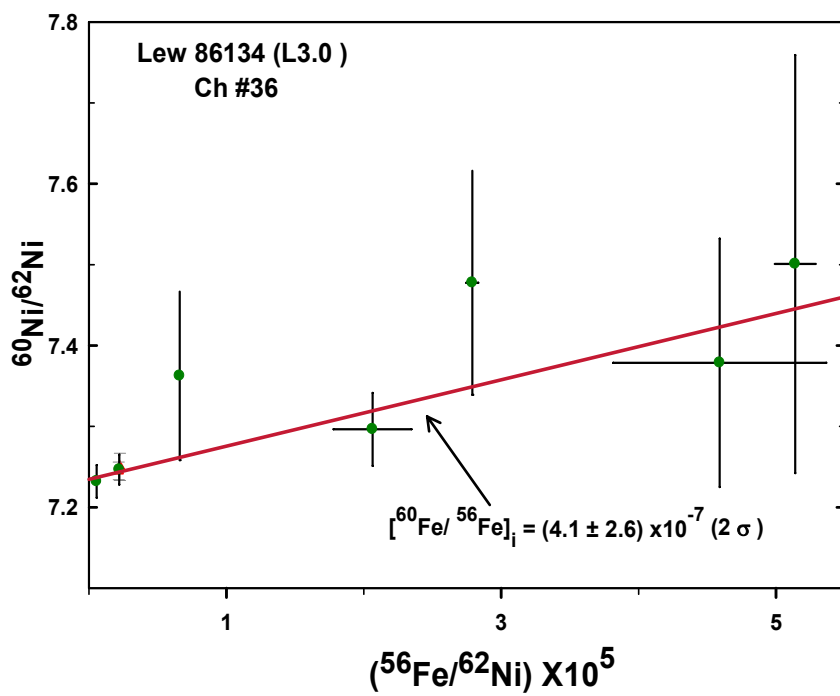
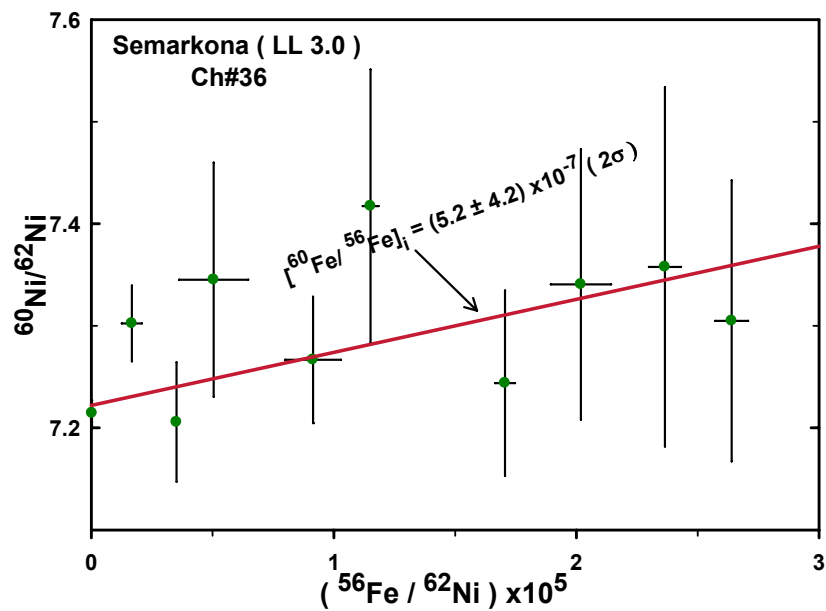


Fig. 4.4 Three isotope Fe-Ni plots for Semarkona chondrule # 36 and LEW chondrule #36. The inferred initial ${}^{60}\text{Fe}/{}^{56}\text{Fe}$ is also shown. The dotted line is the reference value of ${}^{60}\text{Ni}/{}^{62}\text{Ni}$. Error bars 2σ .

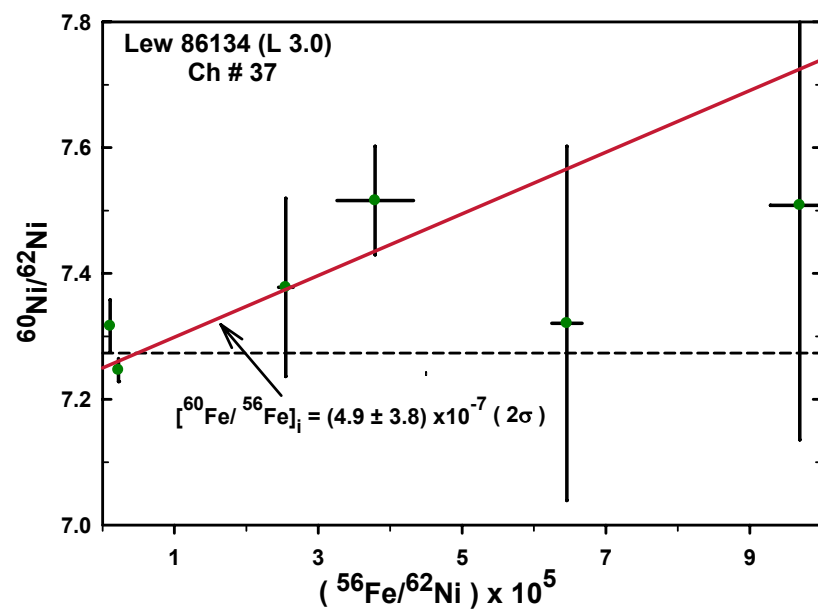
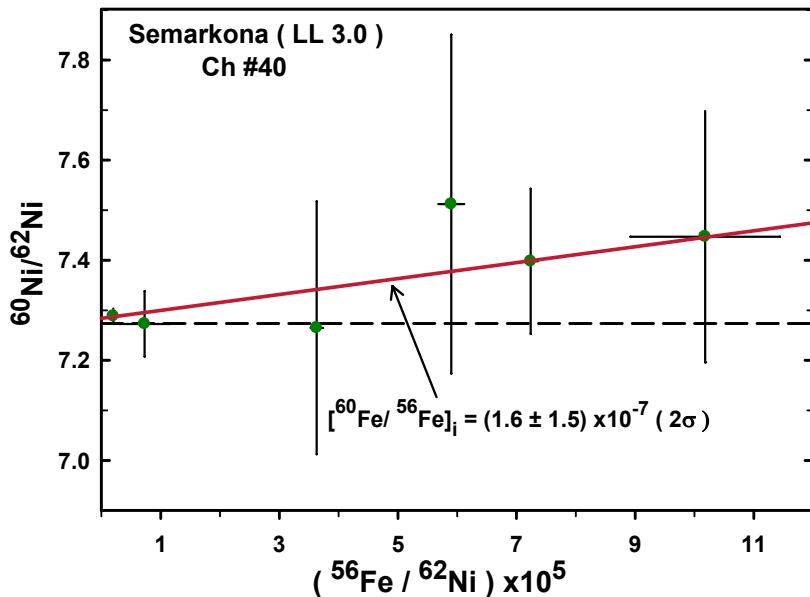


Fig. 4.5 Three isotope Fe-Ni plots for Semarkona chondrule # 40 and LEW chondrule #37. The inferred initial ${}^{60}\text{Fe}/{}^{56}\text{Fe}$ is also shown. The dotted line is the reference value of ${}^{60}\text{Ni}/{}^{62}\text{Ni}$. Error bars 2σ .

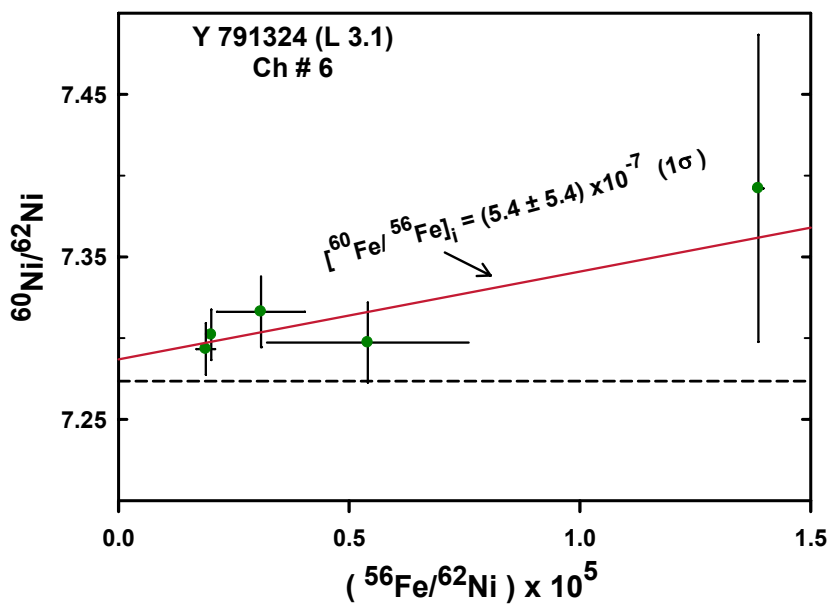
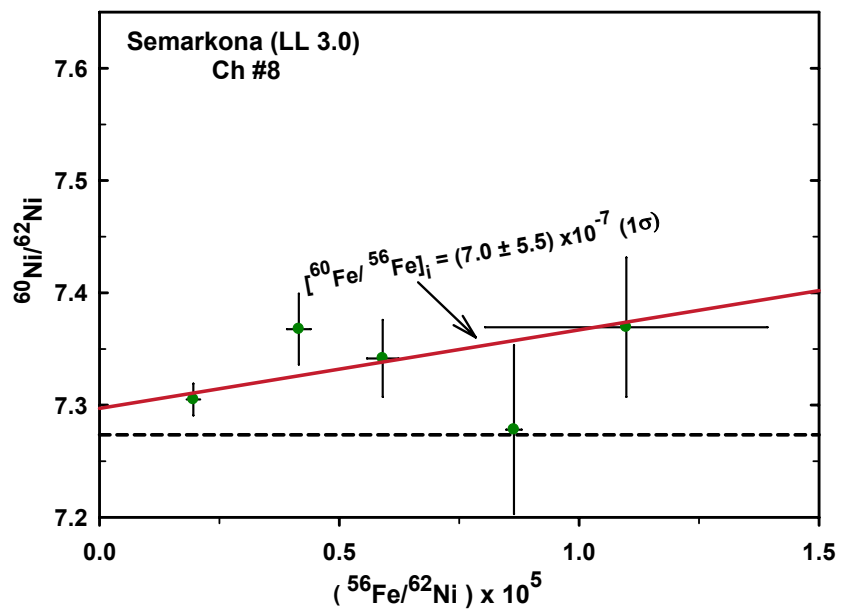


Fig. 4.6 Three isotope Fe-Ni plots for Semarkona chondrule # 8 and Yamato chondrule #6. The inferred initial ${}^{60}\text{Fe}/{}^{56}\text{Fe}$ is also shown. The dotted line is the reference value of ${}^{60}\text{Ni}/{}^{62}\text{Ni}$. Error bars 1σ .

Table 4.4 Results obtained from Fe-Ni isotope systematics in UOCs chondrules

Chondrule	[$^{60}\text{Fe}/^{56}\text{Fe}$] _i ($\pm 2\sigma$)
Sem Ch#18	(6.6±6.0)×10 ⁻⁷
Sem Ch#36	(5.2±4.2)×10 ⁻⁷
Sem Ch#21	(4.8±2.8)×10 ⁻⁷
Sem Ch#20	(4.1±2.8)×10 ⁻⁷
Sem Ch#1	(2.3±1.3)×10 ⁻⁷
Sem Ch#3	(3.2±1.8)×10 ⁻⁷
Lew Ch#36	(4.1±2.6)×10 ⁻⁷
Sem Ch#39	(4.3±2.4)×10 ⁻⁷
Sem Ch#8*	(7.0±11)×10 ⁻⁷
Y791324 Ch#6*	(5.4±11)×10 ⁻⁷
Lew Ch#37	(4.9±3.8)×10 ⁻⁷
Sem Ch#29	(1.97±1.5)×10 ⁻⁷
Sem Ch#40	(1.6±1.5)×10 ⁻⁷
Y791324 Ch#12*	(.95±1.06)×10 ⁻⁷

*Resolved only at 1σ level

4.2 Al-Mg ISOTOPE SYSTEMATICS

4.2.1 Semarkona

Ten chondrules were analysed for Al-Mg isotopic systematics of which four showed well resolved excesses of ^{26}Mg and gave meaningful isochron values of initial $^{26}\text{Al}/^{27}\text{Al}$. Others have either upper limit 1σ values or no suitable (high Al/Mg) regions could be found. The high Al/Mg region were either too small ($< 5\mu\text{m}$) or were surrounded by Mg rich micro-crystallites.

Table 4.5 : Al-Mg isotope data for chondrules from Semarkona (LL 3.0)

Chd	Phases	$^{27}\text{Al}/^{24}\text{Mg}$	$^{26}\text{Mg}/^{24}\text{Mg}$	Initial $^{26}\text{Al}/^{27}\text{Al}$
1	Olivine	0.02	± 0.003	0.1398 ± 0.0002
	Glass	22	± 0.2	0.1404 ± 0.0004
	Glass	40.5	± 1.2	0.1402 ± 0.0005
	Glass	60.7	± 2.4	0.1411 ± 0.0005
	Glass	133.7	± 6.7	0.1407 ± 0.0006
	Glass	222	± 4.2	0.1410 ± 0.0016 $(9.75 \pm 7.52) \times 10^{-6}$
3	Olivine	0.02	± 0.007	0.1391 ± 0.0001
	Glass	0.06	± 0.04	0.1391 ± 0.0001
	Glass	8.8	± 0.0	0.1394 ± 0.0001
	Glass	49.3	± 7.5	0.1394 ± 0.0001
	Glass	64.8	± 5.0	0.1397 ± 0.0002 $(6.4 \pm 5.6) \times 10^{-6}$
8	Olivine	0.004	± 0.003	0.1385 ± 0.0004
	Glass	42.9	± 4.9	0.1401 ± 0.0004
	Glass	56.1	± 4.1	0.1400 ± 0.0003
	Glass	58.7	± 1.6	0.1405 ± 0.0004 $(3.01 \pm 1.78) \times 10^{-5}$
18	Olivine	0.01	± 0.008	0.1390 ± 0.0002
	Glass	24	± 0.2	0.1399 ± 0.0007
	Glass	42	± 1.6	0.1401 ± 0.0004
	Glass	65	± 5.8	0.1417 ± 0.0007
	Glass	81	± 4.6	0.1402 ± 0.0006
	Glass	145	± 0.4	0.1485 ± 0.003 $(2.7 \pm 1.7) \times 10^{-6}$
21A	Olivine	0.01	± 0.006	0.1383 ± 0.0004
	Glass	17	± 1.5	0.1406 ± 0.0009
	Glass	22.8	± 0.4	0.1392 ± 0.0005
	Glass	29.0	± 0.8	0.1412 ± 0.0013 $(5.9 \pm 5.2) \times 10^{-5}$

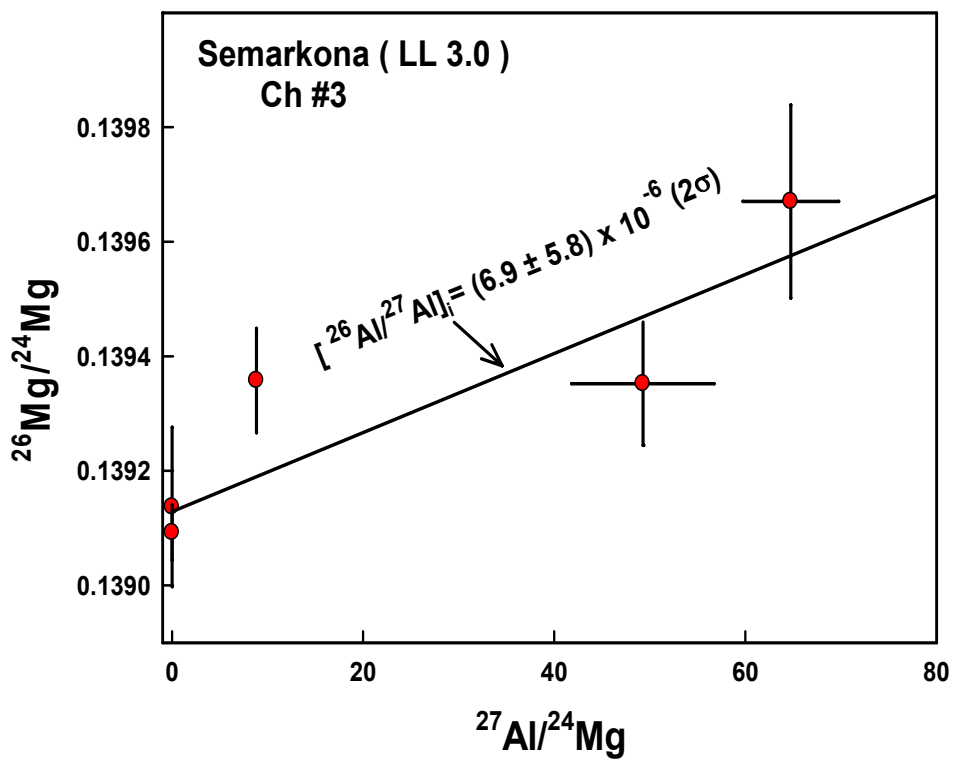
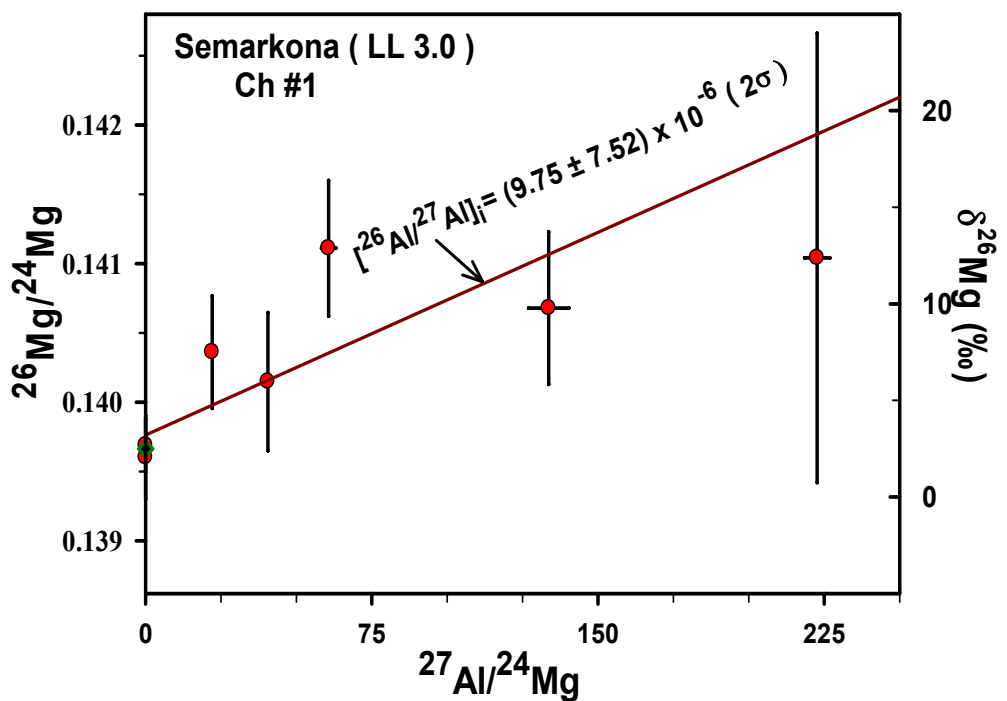


Fig 4.7 Al-Mg Evolution plots of Semarkona (LL 3.0) chondrules:
Ch#1 top; Ch#3 bottom. Error bars 1σ .

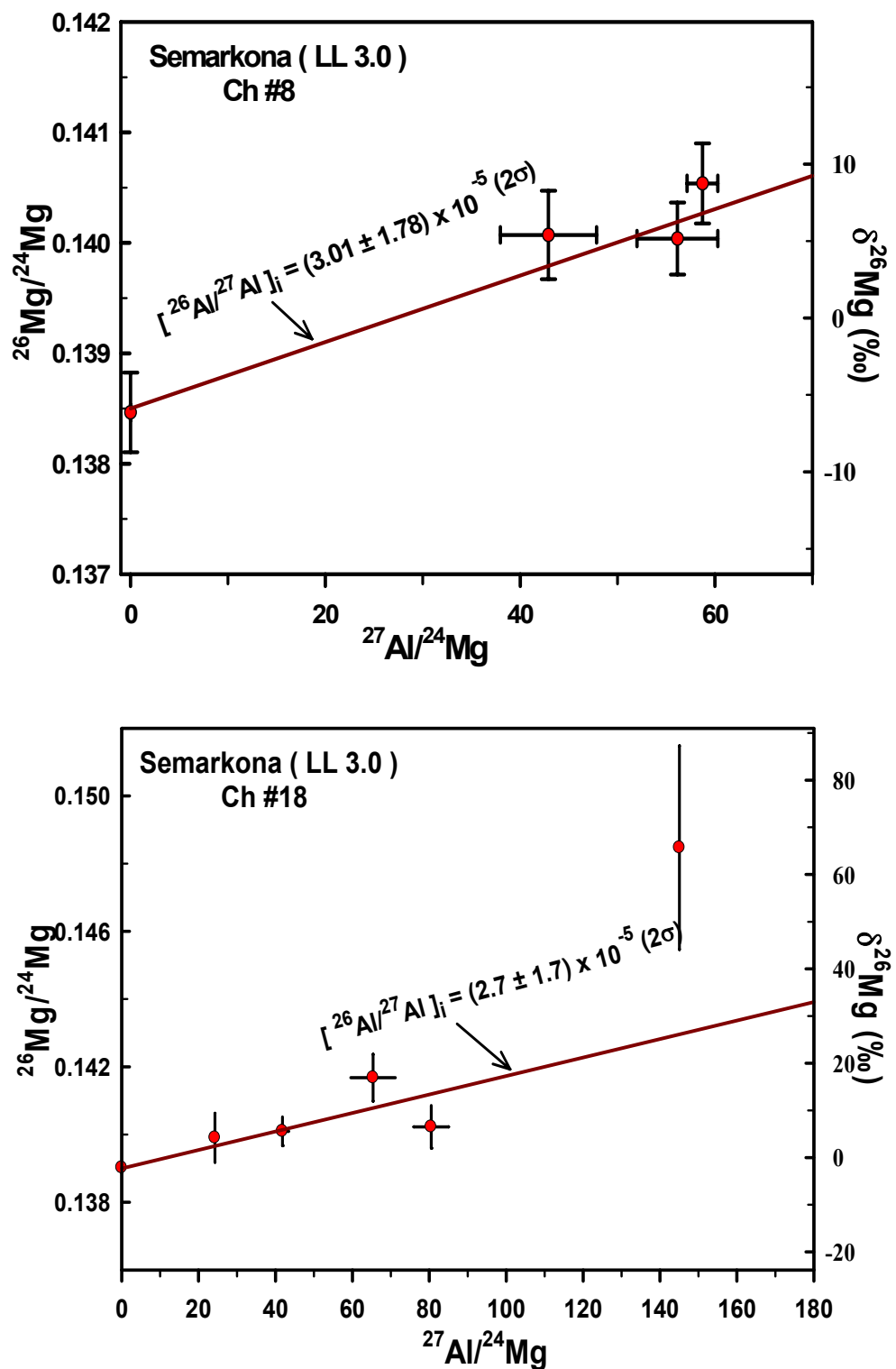


Fig. 4.8 Al-Mg Evolution plots of Semarkona (LL 3.0) chondrules:
Ch#8 top; Ch#18 bottom. Error bars 1σ .

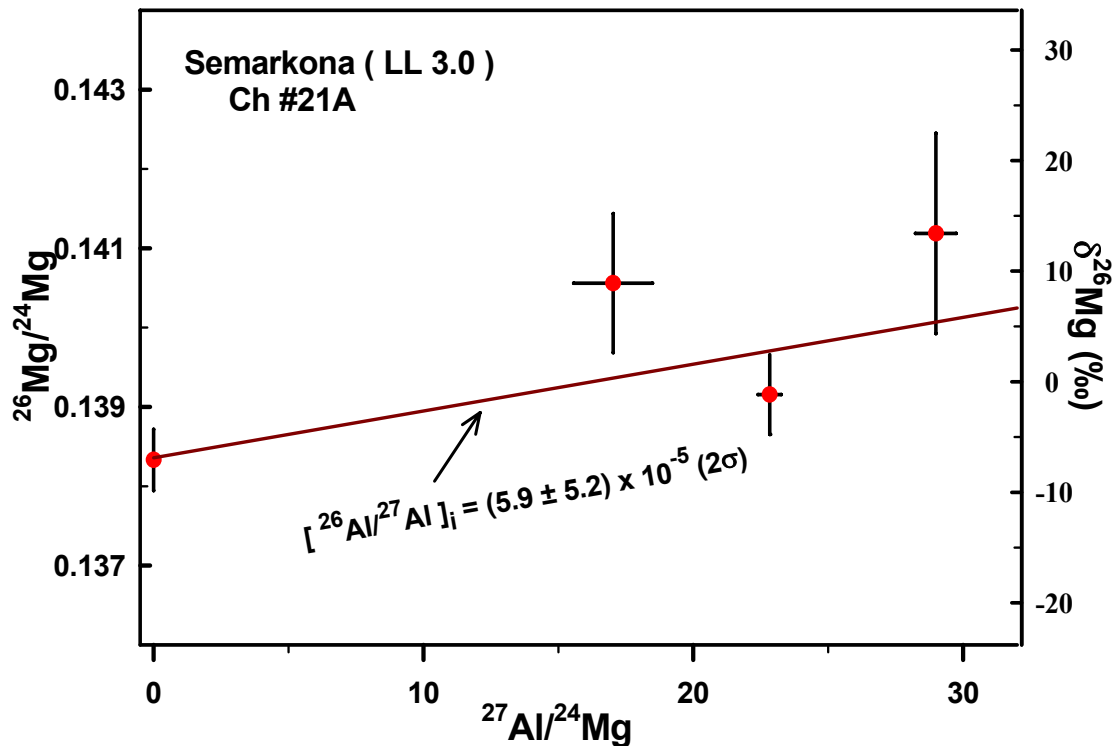


Fig. 4.9 Al-Mg Evolution plot of Semarkona Ch 21A chondrule. Error bars 1σ .

Summary of results obtained from Al -Mg isotope systematics; $^{26}\text{Al}/^{27}\text{Al}$ obtained are shown in Table 4.5 and 4.6 and Fig. 4.7-4.8. Also shown in the lower half of the table (Table 4.6) are results (shown in italics) obtained from similar study done earlier on these thin sections for which Fe-Ni isotope analysis were done in the this thesis and resolved excesses could be seen.

LEW 86134 (L 3.0) & Y791324 (L 3.1) : Of three chondrules selected for the present study in LEW 86134 only one showed resolved excess in 1σ . In others, regions rich in Al were too small to be analysed. In Y791324 also one chondrule showed resolved excess in 1σ .

Table 4.6 Al-Mg isotope data for analysed chondrules

Chondrule	[$^{26}\text{Al}/^{27}\text{Al}$] _i ($\pm 2\sigma$)	Time of formation Ma (relative to CAIs) ($\pm 2\sigma$)		
Sem Ch#18	$(2.70 \pm 1.75) \times 10^{-5}$	0.64	-0.52	+1.09
Sem Ch#1	$(9.75 \pm 7.52) \times 10^{-6}$	1.70	-0.59	+1.53
Sem Ch#3	$(6.9 \pm 5.8) \times 10^{-6}$	2.06	-0.63	+1.91
Sem Ch#8	$(3.01 \pm 1.78) \times 10^{-5}$	0.53	-0.48	+0.93
Sem Ch#39*	$(9.0 \pm 9.5) \times 10^{-6}$	--	--	--
Y791324 Ch#8*	$(2.1 \pm 2.20) \times 10^{-5}$	--	--	--
Y791324 Ch#3*	$(1.1 \pm 1.0) \times 10^{-5}$	--	--	--
Lew Ch#39*	$(1.83 \pm 2.46) \times 10^{-5}$	--	--	--
Sem Ch#20 [‡]	$(1.10 \pm 0.24) \times 10^{-5}$	1.57	-0.21	+0.26
Sem Ch#21 [‡]	$(1.15 \pm 0.54) \times 10^{-5}$	1.53	-0.40	+0.66
Sem Ch#36 [‡]	$(1.24 \pm 0.52) \times 10^{-5}$	1.45	-0.36	+0.56
Lew Ch#36 [‡]	$(1.63 \pm 0.72) \times 10^{-5}$	1.16	-0.38	+0.61
Y791324 Ch#6 [‡]	$(1.22 \pm 0.52) \times 10^{-5}$	1.47	-0.37	+0.58

* Resolved excess only at 1σ level.

† Data reported earlier by Rudraswami & Goswami 2007; Rudraswami et al., 2008.

Table 4.7 : Al-Mg isotope data for chondrules from LEW 86134 (L 3.0)

Chd	Phases	$^{27}\text{Al}/^{24}\text{Mg}$	$^{26}\text{Mg}/^{24}\text{Mg}$	Initial $^{26}\text{Al}/^{27}\text{Al}$
39	Olivine	0.0002 \pm 0.00002	0.1389 \pm 0.0001	
	Glass	22.13 \pm 4.83	0.1393 \pm 0.0002	$(1.83 \pm 2.46) \times 10^{-5}$

Table 4.8 : Al-Mg isotope data for chondrules from Y791324 (L 3.1)

Chd	Phases	$^{27}\text{Al}/^{24}\text{Mg}$	$^{26}\text{Mg}/^{24}\text{Mg}$	Initial $^{26}\text{Al}/^{27}\text{Al}$
8	Olivine	0.003 \pm 0.001	0.1393 \pm 1.3E-04	
	Glass	25.2 \pm 3.0	0.1393 \pm 4.3E-04	
	Glass	33.4 \pm 0.1	0.1399 \pm 4.3E-04	
	Glass	55.6 \pm 10.2	0.1414 \pm 7.6E-04	$(2.1 \pm 2.2) \times 10^{-5}$

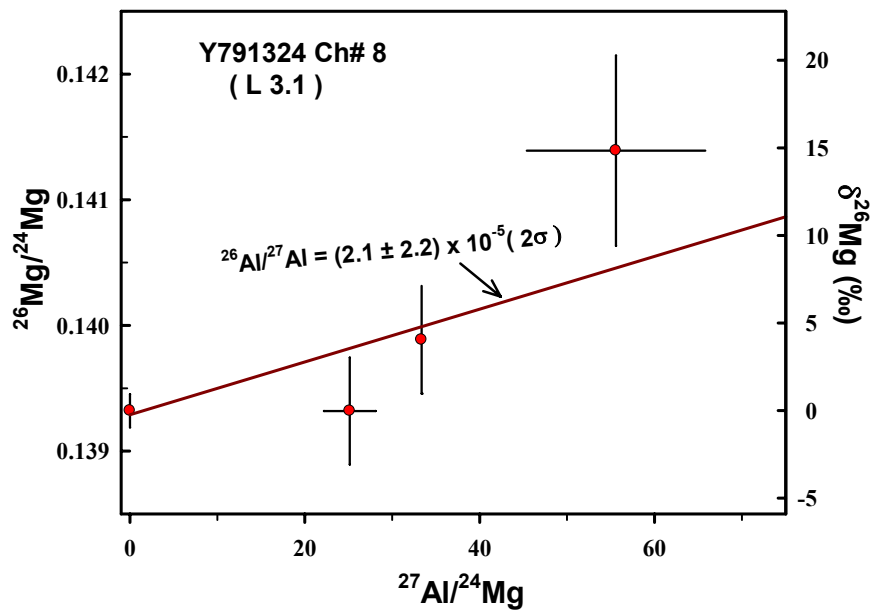


Fig. 4.10 Al-Mg Evolution diagram of Y791324 (L 3.0) chondrule #8.

Summary of results obtained from Fe-Ni and Al-Mg isotope systems in Semarkona LEW86134 and Y79132 are shown in Table 4.9.

Table 4.9 Data for Fe-Ni and Al-Mg isotope systematics for UOC chondrules.

Chondrule	[$^{26}\text{Al}/^{27}\text{Al}$] _i ($\pm 2\sigma$)	[$^{60}\text{Fe}/^{56}\text{Fe}$] _i ($\pm 2\sigma$)	Time of formation † Ma (relative to CAIs) ($\pm 2\sigma$)		
Sem Ch#1	$(9.75 \pm 7.52) \times 10^{-6}$	$(2.3 \pm 1.3) \times 10^{-7}$	1.70	-0.59	+1.53
Sem Ch#2*	$(5.5 \pm 0.33) \times 10^{-6}$	$(1.1 \pm 3.6) \times 10^{-7}$	--	--	--
Sem Ch#3	$(6.9 \pm 5.8) \times 10^{-6}$	$(3.2 \pm 1.8) \times 10^{-7}$	2.06	-0.63	+1.91
Sem Ch#8	$(3.01 \pm 1.78) \times 10^{-5}$	$(7.0 \pm 11) \times 10^{-7}$	0.53	-0.48	+0.93
Sem Ch#18	$(2.70 \pm 1.75) \times 10^{-5}$	$(6.6 \pm 6.0) \times 10^{-7}$	0.64	-0.52	+1.09
Sem Ch#20*	$(1.10 \pm 0.24) \times 10^{-5}$	$(4.1 \pm 2.8) \times 10^{-7}$	1.57	-0.21	+0.26
Sem Ch#21*	$(1.15 \pm 0.54) \times 10^{-5}$	$(4.8 \pm 2.8) \times 10^{-7}$	1.53	-0.40	+0.66
Sem Ch#21A	$(5.9 \pm 5.2) \times 10^{-5}$	--	--	--	--
Sem Ch#29	--	$(1.97 \pm 1.5) \times 10^{-7}$	--	--	--
Sem Ch#36*	$(1.24 \pm 0.52) \times 10^{-5}$	$(5.2 \pm 4.2) \times 10^{-7}$	1.45	-0.36	+0.56
Sem Ch#39	--	$(4.3 \pm 2.4) \times 10^{-7}$	--	--	--
Sem Ch#40	--	$(1.6 \pm 1.5) \times 10^{-7}$	--	--	--
Lew Ch#36*	$(1.63 \pm 0.72) \times 10^{-5}$	$(4.1 \pm 2.6) \times 10^{-7}$	1.16	-0.38	+0.61
Lew Ch#37	--	$(4.9 \pm 3.8) \times 10^{-7}$	--	--	--
Lew Ch#39	$(1.83 \pm 2.46) \times 10^{-5}$	--	--	--	--
Y791324 Ch#3	$(1.1 \pm 1.0) \times 10^{-5}$	--	--	--	--
Y791324 Ch#8	$(2.1 \pm 2.20) \times 10^{-5}$	--	--	--	--
Y791324 Ch#12	--	$(.95 \pm 1.06) \times 10^{-7}$	--	--	--

*Data reported earlier by Rudraswami & Goswami 2007; Rudraswami et al., 2008.

† The time of formation and SSI $^{60}\text{Fe}/^{56}\text{Fe}$ for data set showing resolved excess at 2σ level.

Multiple analyses were carried out on a spot as long as the count rates and Fe/Ni ratios remained nearly the same to improve precision of data. Stability of count rates during multiple analyses, each analyses lasting for a couple of hours, on a spot is shown in Fig. 4.11.

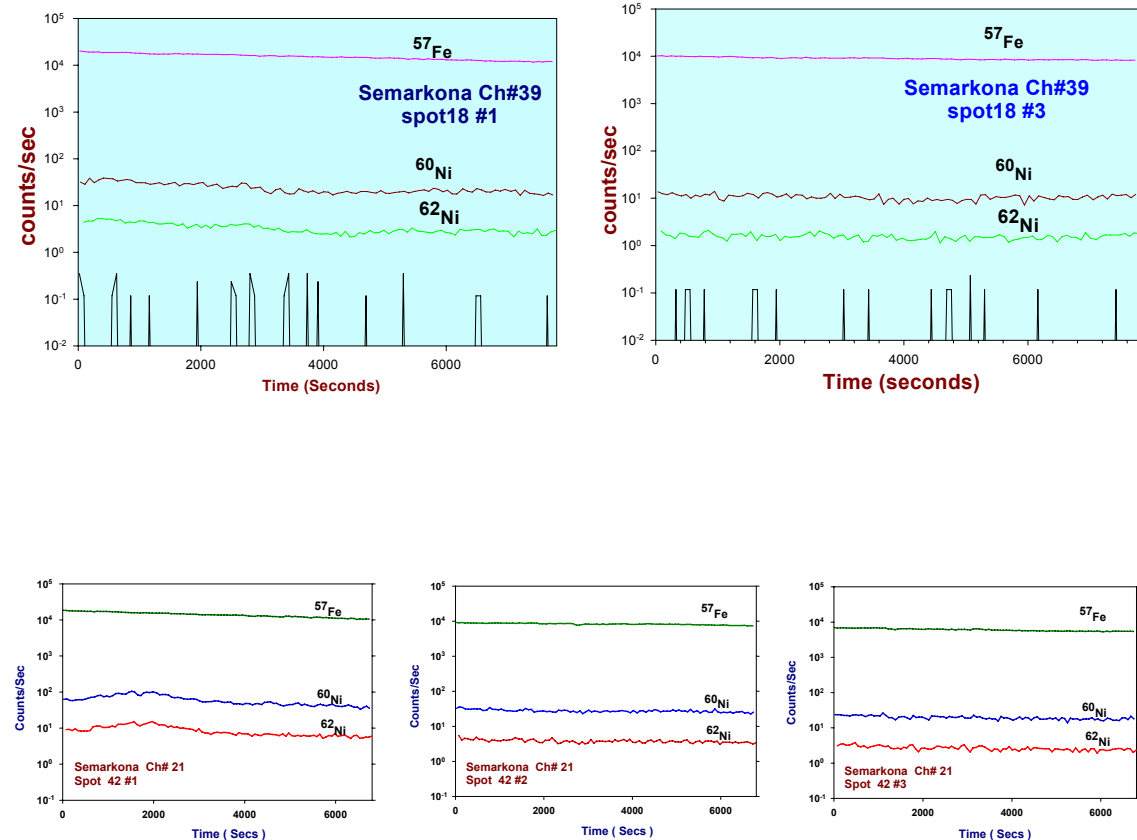


Fig. 4.11 Count rate data from repeat runs on the given spot in Semarkona chondrules (#39, #21). The dynamic background monitored at mass 56.5 is also plotted in the upper panel.

CHAPTER 5: DISCUSSION

Studies of fossil records of ^{60}Fe and ^{26}Al in about twenty chondrules selected out of close to two hundred chondrules from the three UOCs, Semarkona (LL3.0), Lewis Hill 86134 (L3.0) and Yamato 791324 (L3.1), conducted in the present study, have yielded the following important results:

- 1) Excess abundance in ^{60}Ni due to in-situ decay of the SLN ^{60}Fe has been found in eleven chondrules at 2σ level and in four chondrules at 1σ level.. .
- 2) The inferred initial $^{60}\text{Fe}/^{56}\text{Fe}$ values at the time of formation of these chondrules range from $\sim 2 \times 10^{-7}$ to 7×10^{-7} .
- 3) Excess abundance of ^{26}Mg , from in-situ decay of the SLN ^{26}Al , was detected in four chondrules (at 2σ level) of the above sample set in this study. Data for additional five chondrules were available from earlier studies conducted at PRL (Table 5.1). The inferred initial $^{26}\text{Al}/^{27}\text{Al}$ values in these chondrules at the time of their formation range from $(0.7\text{--}2.7) \times 10^{-5}$ indicating their formation ~ 0.6 Ma to ~ 2 Ma after CAIs.
- 4) The data for initial $^{60}\text{Fe}/^{56}\text{Fe}$ for individual chondrules, combined with their time of formation, relative to CAIs, and a half-life of 1.5 Ma for ^{60}Fe yielded SSI $^{60}\text{Fe}/^{56}\text{Fe}$ in the range of $(5\text{--}10) \times 10^{-7}$ with varying errors. The weighted mean SSI $^{60}\text{Fe}/^{56}\text{Fe}$ value based on this data set is $(7.1 \pm 1.8) \times 10^{-7}$ (2σ errors).

In the following, a discussion of the above salient results including their implications towards our understanding of several important topics related to the early history of the solar system is provided. The term “initial $^{60}\text{Fe}/^{56}\text{Fe}$ ” will be used to represent the value at the time of formation of the analyzed chondrules, while the inferred abundance of $^{60}\text{Fe}/^{56}\text{Fe}$ at the time of formation of CAIs will be referred to as the solar system initial (SSI) $^{60}\text{Fe}/^{56}\text{Fe}$.

5.1 Solar System Initial Abundance of ^{60}Fe

^{60}Fe is a unique product of stellar nucleosynthesis and establishing a robust value of SSI $^{60}\text{Fe}/^{56}\text{Fe}$ is important to identify its stellar source. Before discussing the results

obtained in this study, results obtained in previous studies (presented in Chapter 1) are briefly summarized here. An upper limit of 1.6×10^{-6} for SSI $^{60}\text{Fe}/^{56}\text{Fe}$ was inferred from Ni isotopic studies of Allende CAIs (Birck & Lugmair 1988). However, possible presence of nucleogenic Ni isotope anomalies, and lack of phases with high Fe/Ni make the CAIs unsuitable for studies of Fe-Ni isotope system. Conclusive evidence for the presence of ^{60}Fe was provided from a study of Fe-Ni isotope systematics in the differentiated meteorite (eucrite) Chevrony Kut (Shukolyukov & Lugmair 1993a). However, this value turned out to be about an order of magnitude higher than that obtained in another eucrite (Juvinas) with similar Mn-Cr age (Shukolyukov & Lugmair 1993b) and pointed towards disturbed Fe-Ni isotope systematics in eucrites. A study of Fe-rich silicate phases in Ureilite suggested an upper limit of 1.8×10^{-7} (Kita et al., 1998). Recent attempts concentrated on studies of Fe-rich minerals (troilites [FeS] and magnetite [Fe_3O_4]) present in UOC matrix and chondrules; these yielded initial $^{60}\text{Fe}/^{56}\text{Fe}$ in the range of $(1-9) \times 10^{-7}$ (Tachibana & Huss 2003; Mostefaoui et al., 2005) at the time of formation of the analyzed phases. Isotope records in sulphides, are, however susceptible to thermal disturbances and all sulphides may not be primary phases. The possibility of isotope exchange between metal and sulphide in association also cannot be ruled out. More importantly, the time of formation of the analyzed sulphide and oxide phases were unknown and plausible assumptions were made to infer SSI $^{60}\text{Fe}/^{56}\text{Fe}$ values that ranged from $(0.2-1.6) \times 10^{-6}$. Studies of Fe-rich silicates in achondrites and UOCs of low petrologic grades, have also been carried out (Kita et al., 2000; Sugiura et al., 2006; Tachibana et al., 2006). The studies of chondrules from UOCs (Semarkona and Bishunpur) yielded initial $^{60}\text{Fe}/^{56}\text{Fe}$ of $(2.2-3.7) \times 10^{-7}$ at the time of their formation (Tachibana et al., 2006), while Kita et al. (2000) suggested an upper limit of 1.4×10^{-7} based on absence of resolvable ^{60}Ni in a single Semarkona chondrule. Tachibana et al. (2006) suggested SSI $^{60}\text{Fe}/^{56}\text{Fe}$ value of $(5-10) \times 10^{-7}$, assuming that the analyzed chondrules formed within 1.5-2 Ma following the formation of the CAIs. A major lacuna in nearly all the previous efforts is the lack of an independent estimate of the time of formation of the analyzed phases (sulphide, oxide) or object (chondrule) needed to infer SSI $^{60}\text{Fe}/^{56}\text{Fe}$, based on the initial $^{60}\text{Fe}/^{56}\text{Fe}$ at the time of formation of the analyzed samples. An attempt to infer SSI $^{60}\text{Fe}/^{56}\text{Fe}$ from studies of achondrites (Eucrites and Angrites),

whose ages relative to CAIs are inferred from independent studies, yielded a very low value leading to suggestion for possible heterogeneity in the distribution of ^{60}Fe in the early solar system (Sugiura et al., 2006). Fe-Ni and Mn-Cr isotope systematics in sulphide assemblages in unequilibrated enstatite chondrites yielded a spread of about an order of magnitude in the inferred initial value, probably due to thermal perturbation (Guan et al., 2007). Fe-Ni isotope data in the above studies were obtained using ion microprobes.

Attempts to study Fe-Ni isotope systematics using Multi Collector Inductively Coupled Plasma Mass Spectrometer (MC-ICPMS) in carbonaceous and unequilibrated ordinary chondrites were not successful in obtaining well-resolved ^{60}Ni excesses (Quitte et al. 2006a). Similarly studies of metal phases, sulphide and bulk samples of achondrite, stony iron and iron meteorites using Thermal Ionization Mass Spectrometer (TIMS) and MC-ICPMS (Quitté et al., 2006b; Bizzarro et al., 2007; Cook et al., 2008; Dauphas et al., 2008; Regelous et al., 2008) neither provided any direct evidence for presence of ^{60}Fe in the analyzed samples nor supported the proposal for a difference in Ni isotope composition between differentiated meteorites and chondritic meteorites proposed by Bizzarro et al. (2007).

In this thesis, a study of Fe-Ni isotope systematics in Fe-rich silicates (olivine, pyroxene) in chondrules from UOCs of low petrologic grades (3.0, 3.1) was combined with study of Al-Mg isotope systematics in Al-rich glassy phases, present in mesostasis of the same chondrules, to infer SSI $^{60}\text{Fe}/^{56}\text{Fe}$. Chondrules are products of melting of precursor microscopic solids followed by rapid cooling in the solar nebula (Scott & Krot 2005). The chondrule-melting event will homogenize the isotopic compositions of the chondrule resetting the isotope clocks. Thus, the inferred initial $^{26}\text{Al}/^{27}\text{Al}$ and $^{60}\text{Fe}/^{56}\text{Fe}$ values in the chondrules reflect values at the time of their formation in the early solar system. The very low petrologic grades (3.0 and 3.1) of the UOCs selected for this study also rule out any post-formation thermal perturbation in the isotope records. Results obtained from Al-Mg isotope systematics in the chondrules (presented in Chapter -4) allow a determination of the time of formation of the analyzed chondrules, relative to CAIs. The inferred initial $^{60}\text{Fe}/^{56}\text{Fe}$ at the time of formation of the chondrules (presented in Chapter-4) concomitantly with their time of

formation inferred from Al-Mg isotope data allow us to estimate SSI $^{60}\text{Fe}/^{56}\text{Fe}$ with confidence. A summary of results for the seven chondrules that have well resolved excesses in both ^{60}Fe and ^{26}Mg at 2σ level are presented in Table 5.1. The only other datum of combined study of $^{60}\text{Fe}/^{56}\text{Fe}$ and $^{26}\text{Al}/^{27}\text{Al}$ in a chondrule from Semarkona, reported by Tachibana et al. (2007) is also included in this table. Some of the inferred $^{26}\text{Al}/^{27}\text{Al}$ values have been taken from earlier studies (Rudraswami & Goswami 2007; Rudraswami et al., 2008) conducted at PRL and are indicated by italics. The time of formation of the analysed chondrules, relative to CAIs, based on inferred initial $^{26}\text{Al}/^{27}\text{Al}$ in the chondrules, are also shown.

Table 5.1 Initial $^{60}\text{Fe}/^{56}\text{Fe}$ and $^{26}\text{Al}/^{27}\text{Al}$ at the time of formation of UOC chondrules and inferred SSI $^{60}\text{Fe}/^{56}\text{Fe}$

Chondrule	$[^{26}\text{Al}/^{27}\text{Al}]_i$ ($\pm 2\sigma$)	$[^{60}\text{Fe}/^{56}\text{Fe}]_i$ ($\pm 2\sigma$)	Time of formation [#] (Ma)	Inferred SSI $^{60}\text{Fe}/^{56}\text{Fe}$
Sem Ch#18	$(2.70 \pm 1.75) \times 10^{-5}$	$(6.6 \pm 6.0) \times 10^{-7}$	0.64	$(8.87 \pm 8.06) \times 10^{-7}$
Lew Ch#36	$(1.63 \pm 0.72) \times 10^{-5}$	$(4.1 \pm 2.6) \times 10^{-7}$	1.16	$(7.02 \pm 4.45) \times 10^{-7}$
Sem Ch#36	$(1.24 \pm 0.52) \times 10^{-5}$	$(5.2 \pm 4.2) \times 10^{-7}$	1.45	$(10.2 \pm 8.20) \times 10^{-7}$
Sem Ch#21	$(1.15 \pm 0.54) \times 10^{-5}$	$(4.8 \pm 2.8) \times 10^{-7}$	1.53	$(9.72 \pm 5.67) \times 10^{-7}$
Sem Ch#20	$(1.10 \pm 0.24) \times 10^{-5}$	$(4.1 \pm 2.8) \times 10^{-7}$	1.57	$(8.48 \pm 5.79) \times 10^{-7}$
Sem Ch#1	$(9.75 \pm 7.52) \times 10^{-6}$	$(2.3 \pm 1.3) \times 10^{-7}$	1.70	$(5.04 \pm 2.85) \times 10^{-7}$
Sem Ch#3	$(6.9 \pm 5.8) \times 10^{-6}$	$(3.2 \pm 1.8) \times 10^{-7}$	2.06	$(8.28 \pm 4.66) \times 10^{-7}$
Weighted Mean				$(7.07 \pm 1.79) \times 10^{-7}$
SMK 3-6*	$(7.2 \pm 2.8) \times 10^{-6}$	$(1.7 \pm 1.1) \times 10^{-7}$	2.01	$(4.31 \pm 2.79) \times 10^{-7}$

[#] Relative to CAIs.

* Data from Tachibana et al. (2007).

Values for $[^{26}\text{Al}/^{27}\text{Al}]_i$ in *Italics* from Rudraswami & Goswami (2007) and Rudraswami et al. (2008).

Data for initial $^{60}\text{Fe}/^{56}\text{Fe}$ inferred at the time of formation of each chondrule along with its time of formation, relative to CAIs, based on Al-Mg isotope data, and the half-life of ^{60}Fe (1.5 Ma) can be used to estimate of the SSI $^{60}\text{Fe}/^{56}\text{Fe}$ (last column in Table 5.1). The mean value of $[^{26}\text{Al}/^{27}\text{Al}]_i$ in the chondrules was used to infer their

time of formation, relative to CAIs. The estimated SSI $^{60}\text{Fe}/^{56}\text{Fe}$ span the range $(5\text{-}10)\times10^{-7}$ that include the uncertainty in the inferred initial $[^{60}\text{Fe}/^{56}\text{Fe}]_i$. The independent estimates for SSI $^{60}\text{Fe}/^{56}\text{Fe}$, obtained from the data from each of the seven individual chondrules, where we have found excess in both ^{60}Ni and ^{26}Mg at 2σ level, yield a weighted mean SSI $^{60}\text{Fe}/^{56}\text{Fe}$ value of $(7.1\pm1.8)\times10^{-7}$ (2σ). If the uncertainty in the formation time of the chondrules, relative to CAIs, is also considered, based on the errors in $[^{26}\text{Al}/^{27}\text{Al}]_i$ (Table 4.4), the corresponding mean values are 5.6×10^{-7} (for positive error) and 11.3×10^{-7} (for negative error), respectively. We believe the data presented in this work establish that the value of SSI $^{60}\text{Fe}/^{56}\text{Fe}$ is $>5\times10^{-7}$ with a most probable value of $\sim7\times10^{-7}$. This may be considered as the first robust value for SSI $^{60}\text{Fe}/^{56}\text{Fe}$ reported till date.

The inferred SSI $^{60}\text{Fe}/^{56}\text{Fe}$ value is higher than those reported from studies of Fe-rich sulphide and oxide phases in UOC chondrules (Tachibana et al., 2003), but within the range of $(5\text{-}10)\times10^{-7}$ reported by (Tachibana et al., 2006) for silicates in UOC chondrules, based on an assumed range (1.5 to 2 Ma after CAIs) for the age of formation of the analyzed chondrules. The SSI $^{60}\text{Fe}/^{56}\text{Fe}$ value obtained in this study do not support the suggested high value of $\sim1.5\times10^{-7}$ based on studies of CAIs and sulphides (Birck & Lugmair 1988; Mostefaoui et al., 2005). The inconsistency with the value suggested from studies of CAIs may be caused by preserved nucleosynthetic anomalies in them. Further, the possibility of disturbance in Fe-Ni isotope records in samples of chondrites and achondrites studied earlier cannot be ruled out. For example, the Fe-Ni isotope records in eucrites appeared to be disturbed and investigations by various groups did not yield concordant results. Bulk analysis of silicate chondrules from Chainpur (LL3.4) also did not yield well-behaved isotope systematics (Chen et al., 2009). An integrated approach of determining both the time of formation as well as Fe-Ni isotope systematics in samples expected to retain pristine isotope records was lacking in previous attempts; the present study is the first attempt to remove this ambiguity.

5.2 Plausible Source(s) of ^{60}Fe

In general, SLNs present in the early solar system could be of stellar origin or/and products of energetic particle interactions with gas and dust in the protosolar cloud or

in the evolved solar nebula (Goswami et al., 2005; Huss et al., 2009). However, production of ^{60}Fe by energetic particle interactions is extremely inefficient due to lack of suitable targets in the solar nebula for proton or alpha particle induced reactions leading to production of this very neutron-rich nuclide. Few possible reactions with neutron rich target nuclides, such as, $^{64}\text{Ni}(\text{p}, \text{p}\alpha)^{60}\text{Fe}$, $^{58}\text{Fe}(\alpha, 2\text{p})^{60}\text{Fe}$ have very low reaction cross sections of \sim 50-150 micro-barns (Lee et al., 1998). Thus, even in the most optimistic scenarios, energetic particle irradiation models that attempt to account for the SSI abundances of other SLNs (e.g. $^{26}\text{Al}/^{27}\text{Al}=5\times 10^{-5}$) under produce $^{60}\text{Fe}/^{56}\text{Fe}$ by several orders of magnitude below the range of SSI values (10^{-7} to 10^{-6}) reported so far (Lee et al., 1998; Leya et al., 2003; Huss et al., 2009).

On the other hand, ^{60}Fe is produced during stellar nucleosynthesis via neutron capture processes taking place during various evolutionary phases of different mass stellar sources (Timmes et al., 1995; Woosley & Weaver 1995; Rauscher et al., 2002; Limongi & Chieffi 2006; Wasserburg et al., 2006). ^{60}Fe is product of neutron capture on ^{59}Fe (half life = 44 days), which itself is produced by neutron capture on ^{56}Fe and ^{58}Fe . Although in high temperature ($\geq 10^9\text{K}$) stellar interior, the effective half-life of ^{59}Fe can get reduced, efficient production of ^{60}Fe is still plausible (Limongi & Chieffi 2006). ^{60}Fe is, therefore, considered as a distinct product of stellar nucleosynthesis.

The question, whether some or all of the SLNs present in the early solar system solids may represent galactic steady state abundances of these nuclides, representing averages of contributions from various stellar sources over time, has been addressed initially by Clayton (1984). More recent studies (Jacobsen, 2005; Huss et al., 2009) clearly suggest that the inferred SSI abundances of $^{60}\text{Fe}/^{56}\text{Fe}$ and $^{26}\text{Al}/^{27}\text{Al}$ cannot be explained by galactic steady state abundances of these nuclides and require a late injection of freshly synthesized ^{60}Fe and ^{26}Al into the nascent solar system. A brief outline of the various nucleosynthesis processes occurring in different stellar sources that may lead to production of ^{60}Fe is presented here before considering the most plausible stellar source of ^{60}Fe present in the early solar system.

5.3 Stellar Nucleosynthesis and ^{60}Fe

Significant progress has been made in recent decades in our understanding of the evolution of stars of various masses and nucleosynthesis processes operating during various phases of their evolution. However, a proper knowledge of the evolution of stars in the mass range of $7\text{-}11 M_{\odot}$ and mass greater than $40M_{\odot}$ is still lacking. Further, there are still uncertainties in reaction cross sections for the neutron production via $[^{22}\text{Ne}(\alpha, n)^{25}\text{Mg}]$, and mass loss rates of high mass stars. Nonetheless, evolution of low mass stars ($1\text{-}7M_{\odot}$) and massive stars having mass in the range of ($\sim 11\text{-}40 M_{\odot}$) and nucleosynthesis processes taking place in these stars are reasonably well understood. Huss et al. (2009) have provided a detail review of the stellar nucleosynthesis processes that can produce the SLNs present in the early solar system. In the following, we particularly discuss the current understanding of stellar production of the short-lived nuclide, ^{60}Fe .

5.3.1 Production of ^{60}Fe in Asymptotic Giant Branch (AGB) star

Low and intermediate mass stars ($1\text{-}8 M_{\odot}$) evolve towards the Asymptotic Giant Branch (AGB) phase after the completion of hydrogen and helium burning in their cores, and before they form planetary nebulae and end their life as white dwarfs. An

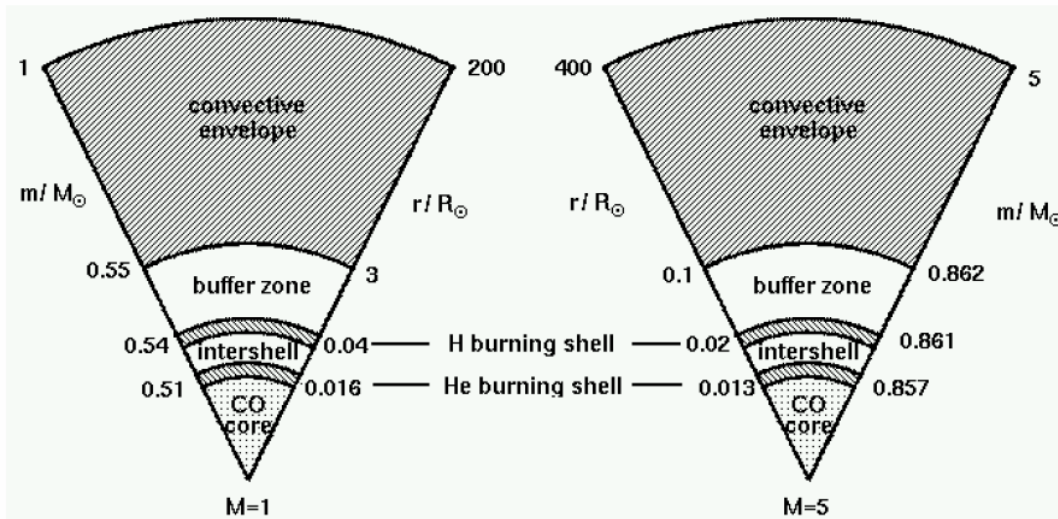


Fig. 5.1 Structure of $1M_{\odot}$ and $5M_{\odot}$ star during AGB phase

AGB star has an inert carbon-oxygen (C-O) core surrounded by helium burning shell, helium-hydrogen intershell, hydrogen burning shell, buffer zone and a very large

convective hydrogen envelope that contains majority of the stellar mass (Fig. 5.1). A characteristic phase of the AGB stars is the thermally pulsing stage due to alternate burning of H and He that mixes material from the He shell and the inter-shell region between the H and He shell. The evolution of AGB stars and nucleosynthesis taking place during various phases of evolution have been extensively studied (Lattanzio 1991; Straniero et al., 1997; Busso et al., 1999; Herwig 2005; Wasserburg et al., 2006). Distribution of mass and physical dimensions of typical AGB stars are shown in Fig. 5.1 for $1M_{\odot}$ and $5M_{\odot}$ solar masses.

There are two major pathways leading to production of neutrons in AGB stars, $^{13}\text{C}(\alpha, n)^{16}\text{O}$ and $^{22}\text{Ne}(\alpha, n)^{25}\text{Mg}$. The ^{13}C neutron source operates at relatively low neutron densities ($N_n < 10^7 \text{ cm}^{-3}$) and temperatures ($T < 0.9 \times 10^8 \text{ K}$) in TP-AGB stars during the inter-pulse period. The ^{22}Ne neutron source operates at much higher neutron densities ($N_n > 10^{10} \text{ cm}^{-3}$) and requires higher temperatures ($T > 3 \times 10^8 \text{ K}$) which are achieved only when the convective thermal pulse is ongoing. In high mass AGB stars, such temperatures are more easily achieved, and ‘s’ process elements are expected to form mainly due to neutrons from the $^{22}\text{Ne}(\alpha, n)^{25}\text{Mg}$ reaction. The $^{13}\text{C}(\alpha, n)^{16}\text{O}$ neutron source provides a higher total number of neutrons but lower neutron density than $^{22}\text{Ne}(\alpha, n)^{25}\text{Mg}$ source that can produce high neutron density of up to 10^{13} n/cm^3 . In AGB stars ($\sim 3M_{\odot}$), the ‘s’process occurs both in the He shell and the inter-shell region between the H and He shells. For a $4M_{\odot}$ AGB star, temperature during helium shell burning is sufficiently high to activate the $^{22}\text{Ne}(\alpha, n)^{25}\text{Mg}$ neutron source and neutron density $> 3 \times 10^{10} \text{ n/cm}^3$ is achieved. In AGB stars of mass greater than $4M_{\odot}$, ^{60}Fe is efficiently produced during convective core He burning. Studies of nucleosynthesis yield during AGB phase for stars in the mass range ($1-5$) M_{\odot} with different metallicities suggest that low ($1-2$) M_{\odot} and intermediate mass ($3-5$) M_{\odot} AGB stars can at best explain a SSI $^{60}\text{Fe}/^{56}\text{Fe}$ value of 3×10^{-7} and up to 10^{-6} , while accounting for SSI abundances of a few other SLNs like ^{41}Ca , ^{26}Al and ^{107}Pd . However, the higher value of $^{60}\text{Fe}/^{56}\text{Fe}$ is possible only if one considers an intermediate $5M_{\odot}$ AGB star and an extremely short interval of $\sim 10^5$ years between injection of freshly synthesized nuclides and formation of the first solar system solids (Wasserburg et al., 2006), which is not realistic. A recent study (Trigo-Rodriguez et al., 2009) suggests that nucleosynthesis yield from a $6.5M_{\odot}$ AGB star with solar

metallicity may explain SSI $^{60}\text{Fe}/^{56}\text{Fe}$ and also the canonical SSI abundance of $^{26}\text{Al}/^{27}\text{Al}$, $^{41}\text{Ca}/^{40}\text{Ca}$ and $^{107}\text{Pd}/^{108}\text{Pd}$ assuming a time interval of $\sim 5 \times 10^5$ years and a dilution factor of 3×10^{-3} , a value that is more than an order of magnitude higher than the typical value of $\sim 10^{-4}$ for dilution factor considered in most of the earlier studies.

5.3.2 Production of ^{60}Fe in Massive ($>10\text{M}_\odot$) Star

In massive stars ($M > 10\text{M}_\odot$), the nuclear burning in the core starts with hydrogen burning and continues with successive burning of He, C, O, Ne and Si until the production of the Fe-group elements, as the core becomes progressively hotter. The core is finally surrounded by concentric shells where the previous burning (H, He, C, O, Ne, Si) took place. Synthesis of ^{60}Fe takes places both during the hydrostatic equilibrium phase of different shell burning as well as during the core collapse explosive phase (Woosley & Weaver 1995; Rauscher et al., 2002; Limongi & Chieffi 2006; Huss et al., 2009). A brief discussion of the same is provided here.

Hydrostatic Equilibrium Phase

^{60}Fe is produced by “s” process during He and C shell burning via neutron capture on ^{59}Fe [$^{59}\text{Fe}(\text{n},\gamma)^{60}\text{Fe}$] in the presence of the neutron sources $^{22}\text{Ne}(\alpha, \text{n})^{25}\text{Mg}$ and $^{13}\text{C}(\alpha, \text{n})^{16}\text{O}$, discussed previously. A general trend of increased ^{60}Fe production with increasing mass of a star is seen due to the higher abundance of seed nuclides and stronger activation of neutron source in more massive stars (Limongi & Chieffi 2006). Fig 5.2. shows yield of ^{60}Fe from different model calculations for a range of stellar masses. Woosley & Weaver (1995) and Rauscher et al. (2002) have extensively studied the evolution of $1-40\text{M}_\odot$ through all hydrostatic burning stage up to core collapse and explosive burning, and calculated the yields of various species including ^{60}Fe (Woosley & Weaver 1995; Rauscher et al., 2002). Limongi & Chieffi (2006) reported yields following evolution through all the phases including the explosive burning for solar metallicity stars in the mass range of $11-120\text{M}_\odot$. (Limongi & Chieffi 2006). Woosley and Heger (2007) have also presented yields for model calculation of stars in the range of $12-120\text{ M}_\odot$. Calculated yields of ^{60}Fe in these two models are not mutually consistent for massive stars. It may be noted that understanding the evolution of very massive stars is hampered by significant uncertainties in parameters

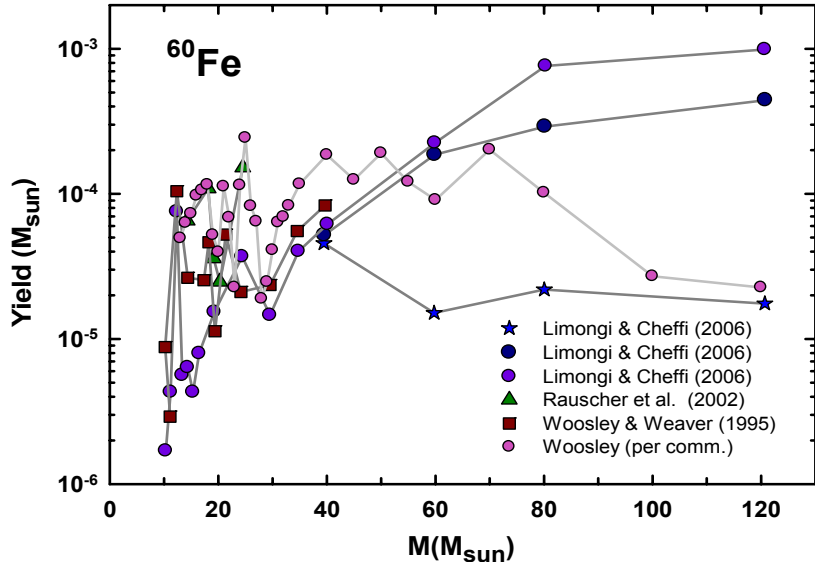


Fig. 5.2. ^{60}Fe yield (in solar mass) from model calculations for various stellar masses with solar metallicity. Results from Limongi & Chieffi are for two different stability criterion (\star , \bullet) and mass loss rate (\circ).

like mass loss rates during various phases of evolution, nuclear reaction cross sections and treatment of convection.

Explosive Nucleosynthesis

During explosive nucleosyntheses, at the time of core collapse, ^{60}Fe is produced in Fe-Ni core and at the base or within the Carbon convective shell where a peak temperature of 2.2×10^9 K is reached when the shock wave following core collapse traverses through it. The presently available models suggest that the total yield of ^{60}Fe is dominated by the contribution from the convective carbon shell for stars with mass less than 40M_\odot , while for stars with higher masses the He convective shell makes the major contribution to the total yield. Overall, the contribution from the explosive burning is not a major contributor to the total yield of ^{60}Fe . The yield during various phases, and hence the total yield from a star, varies as a function of its mass, metallicity, rotation rate etc. Contributions from He convective shell, C convective shell and explosive nucleosynthesis along with total yields estimated for two convective stability conditions, the Schwarzschild and Ledoux criteria, by Limongi & Chieffi (2006) are shown in Fig. 5.3.

5.4 Sources of ^{26}Al

Even though the primary focus of this work is on Fe-Ni isotope systematics, we note that ^{26}Al , used as a chronometer in this study to infer the time of formation of the analyzed chondrules, can be produced by both energetic particle interactions as well as stellar nucleosyntheses. Production of ^{26}Al by solar energetic particles interacting with gas and dust of solar composition as well as synthesis of ^{26}Al during stellar

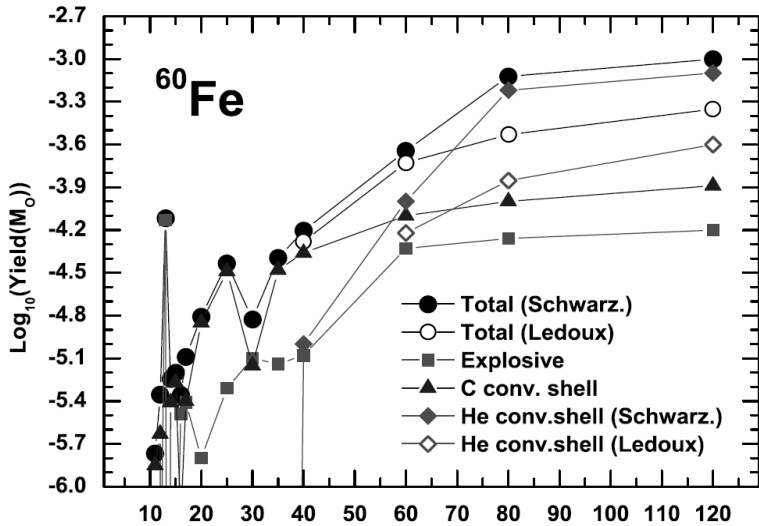


Fig. 5.3 Contribution from various shells to the total yield of ^{60}Fe for stars of solar metallicity

nucleosynthesis has been discussed extensively and summarized in Goswami et al.(2001, 2005), Leya et al. (2003); Chaussidon and Gounelle (2006) and Huss et al. (2009). Studies of possible production of ^{26}Al , along with ^{10}Be , a distinct product of energetic particle production, using parameters that matches SSI $^{10}\text{Be}/^{9}\text{Be}$ failed to reproduce the SSI $^{26}\text{Al}/^{27}\text{Al}$ value of 5×10^{-5} (Goswami et al., 2001; Marhas et al., 2002; Duprat & Tatischeff 2007; Fitoussi et al., 2008). At present, ^{26}Al in the early solar system is also considered primarily to be of stellar origin.

Production of ^{26}Al in various stellar sources (TP-AGB star, supernova and W-R stars) have been studied by several groups (Cameron et al., 1995; Woosley & Weaver 1995; Wasserburg et al., 1996; Arnould et al., 1997; Rauscher et al., 2002; Woosley et al., 2002; Arnould et al., 2006; Limongi & Chieffi 2006; Wasserburg et al., 2006; Woosley & Heger 2007). As noted earlier, co-production of ^{26}Al and ^{60}Fe to match

the solar system initial abundances of these two SLNs is possible only for intermediate mass ($4\text{-}5M_{\odot}$) AGB star but with very restricted parameters. Nucleosynthetic yields from high mass supernova can in principle be the source of both these SLNs. Suggestion for production of ^{26}Al during the wind phase of a W-R star and ^{60}Fe during its final explosive phase as a SN, leading to late injection of ^{60}Fe , relative to ^{26}Al , into the early solar system has also been proposed (Bizzarro et al., 2007).

In the following a discussion of the results obtained in this work is presented keeping in view our current understanding of the stellar production of the SLNs, ^{26}Al and ^{60}Fe , present in the early solar system objects.

5.5 Stellar Source(s) of SLNs ^{60}Fe and ^{26}Al

The question of co-injection of most of the SLNs, particularly those with shorter half-lives, from a single stellar source has been discussed extensively by various authors. Two parameters, dilution of freshly synthesized stellar material hosting SLNs with protosolar cloud material devoid of SLNs, and the free decay time, defining the time interval between production of the SLNs at the stellar site and their incorporation into the first solar system solids, need to be invoked in these calculations. Further, depending on the choice of the stellar source (low mass/high mass; AGB/SN/W-R) additional parameters such as stellar mass and neutron source strength are also to be taken into account. In the case of high mass exploding star (SN), one has to consider mixing of material between different shells as well as fall back of mass into the core following explosion. In the following, a brief summary of the present status in this field, pertinent to the present work is provided.

Several groups have performed analytical studies to infer the SSI $^{60}\text{Fe}/^{56}\text{Fe}$ by considering supernova and WR stars as plausible sources. Freshly synthesized material released via stellar wind from WR stars that can account for SSI $^{26}\text{Al}/^{27}\text{Al}$ can lead to a SSI $^{60}\text{Fe}/^{56}\text{Fe}$ value of only a few times 10^{-8} (Arnould et al., 2006). Yields from presently available models of core collapse supernova can explain higher values $^{60}\text{Fe}/^{56}\text{Fe}$ in the range of 3×10^{-7} to 1×10^{-5} (Rauscher et al., 2002; Woosley et al., 2002; Limongi & Chieffi 2006; Woosley & Heger 2007). Meyer (2005) considered a high mass ($25M_{\odot}$) star and yields of various SLNs from the resultant

supernova and suggested that SSI abundances of several SLNs, including SSI $^{60}\text{Fe}/^{56}\text{Fe}$ of 10^{-6} and $^{26}\text{Al}/^{27}\text{Al}$ of 5×10^{-5} , may be explained simultaneously using a free decay time of 1Ma with a injection mass cut of $5.5 M_{\odot}$ and a dilution factor of $\sim 4 \times 10^{-4}$ (Meyer 2005). However, this also leads to a much higher value of SSI $^{53}\text{Mn}/^{55}\text{Mn}$. This problem is circumvented by considering fall-back of material onto the collapsed core that will ensure that the stellar source will not eject most of the ^{53}Mn synthesized in the inner zone (Meyer 2005). Takigawa et al. (2008) considered a faint SN and followed a similar approach in another attempt to explain concurrently the abundance of several SLNs present in early solar system objects.

An attempt is made in this study to check if the nucleosynthesis yields from model calculations of Rauscher et al. (2002) and Limongi and Cheffi (2006) for SN can simultaneously explain the inferred SSI values for SSI $^{60}\text{Fe}/^{56}\text{Fe}$ and $^{26}\text{Al}/^{27}\text{Al}$. In Fig 5.4. yields of nuclides from the different zones, 25000 seconds after supernova event, for a $25 M_{\odot}$ star are shown based on the data of Rauscher et al. (2002).

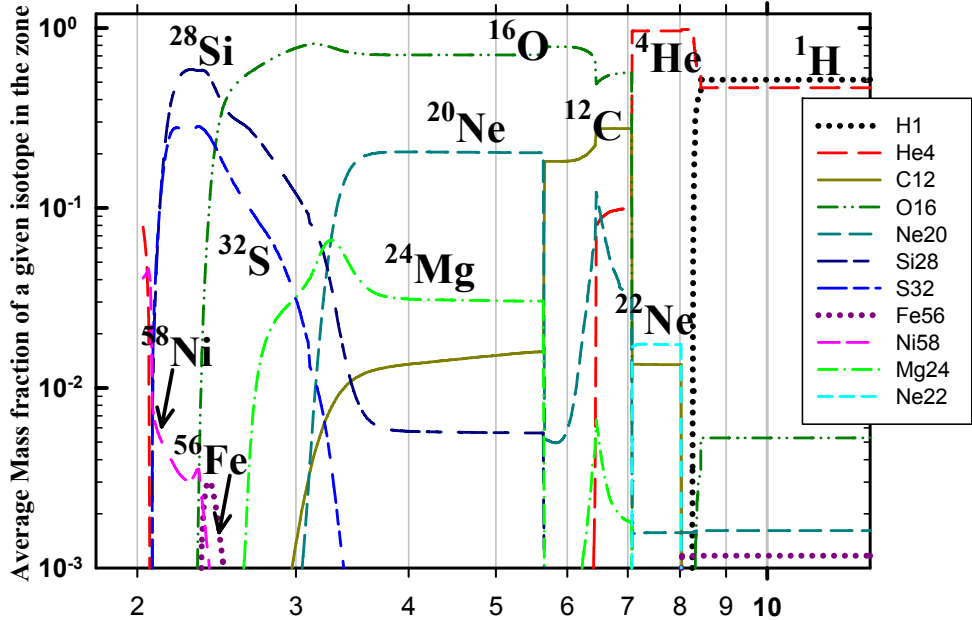


Fig. 5.4 Nucleosynthesis yields in various zones of a $25 M_{\odot}$ star based on one of the model (s25a31d) output from Rauscher et al. (2002).

Using the input from Rauscher et al. (2002) total yields for different SLNs for a $25M_{\odot}$ star with varying injection mass cut and different neutron source rate and supernova condition were obtained. These results were combined with plausible dilution factor and free decay time to check if they can concurrently explain the observed SSI abundances of various SLNs. The results obtained from one such effort, considering a specific model (s25a31d; Rauscher et al. 2002), that incorporates a particular set of reaction cross sections for the neutron source function $^{22}\text{Ne}(\alpha, n)^{25}\text{Mg}$, is shown in Fig. 5.5. It may be noted that nucleosynthesis yields from a $25M_{\odot}$ star can simultaneously explain the SSI abundances of ^{26}Al , ^{60}Fe , ^{107}Pd if we assume a free decay time of a million year along with dilution factor of 10^{-3} and a injection mass cut at $\sim 7.5M_{\odot}$. The same set of parameters can also match SSI $^{41}\text{Ca}/^{40}\text{Ca}$ within a factor of two.

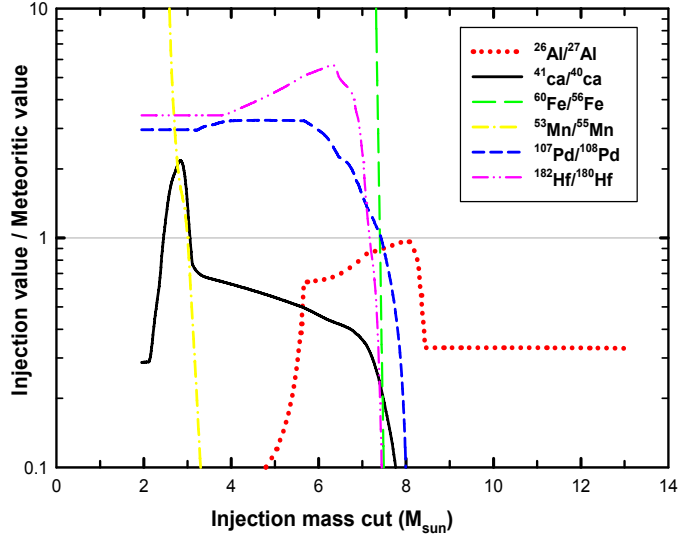


Fig. 5.5 SSI abundances for a set of SLNs, including ^{26}Al and ^{60}Fe , based on a model yields from a $25M_{\odot}$ star (Rauscher et al. 2002) compared with observed values. A good fit is obtained for ^{26}Al , ^{60}Fe and a few other SLNs.

The yields from models of Limongi and Cheffi (2006) were also considered for a similar exercise. However, their model yields do not contain data for isotopes of Pd and Hf. Hence, only abundances for ^{26}Al , ^{60}Fe , ^{41}Ca , and ^{53}Mn were evaluated for different choices of the free parameters. The calculated yields from a $35M_{\odot}$ star could explain SSI $^{26}\text{Al}/^{27}\text{Al}$ and $^{60}\text{Fe}/^{56}\text{Fe}$ if one assumes a dilution factor of 0.01, a free

decay time of 1Ma and an injection mass cut of \sim 5-8M_⊙. However, the dilution factor considered is much higher than the nominal values of one to a few times 10⁻⁴.

Thus, an intermediate mass (4-5 M_⊕) AGB star as well as massive (~25-35M_⊕) stars ending their life as supernova may be considered as plausible sources of ⁶⁰Fe. The results obtained in this study suggest a SSI $^{60}\text{Fe}/^{56}\text{Fe} > 5 \times 10^{-7}$ that would indicate a high mass supernova to be the more likely candidate. While observations of supernova occurring close to star forming regions are quite common, AGB stars have not been observed in close vicinity of star forming regions. Kastner and Myers (1994) calculated a low probability of ~1% chance of a low mass AGB star encountering a molecular cloud within a million year (Kastner & Myers 1994). Recent evaluation of this probability when one considers a intermediate mass (4-5)M_⊕ AGB star, proposed for explaining the SSI $^{60}\text{Fe}/^{56}\text{Fe}$, the value drops down further by a few order of magnitude due to the lower abundance of high mass AGB stars and also their much shorter life time (Huss et al., 2009). Thus, although it is difficult to completely rule out an intermediate mass AGB star as the source, the SSI $^{60}\text{Fe}/^{56}\text{Fe}$ obtained in this study, coupled with the very low probability of a intermediate mass AGB star contaminating a molecular cloud, makes a high mass SN the most likely source for ⁶⁰Fe, ²⁶Al and several other SLNs present in the early solar system. Nonetheless, the uncertainties in various parameters used in the calculations of isotope yields and differences in results obtained, if one adopts various SN model predictions, suggest that further refinement of stellar model is needed for better understanding the exact nature of the SN responsible for the various SLNs present in the early solar system.

5.6 Co-injection of ²⁶Al & ⁶⁰Fe into Solar System:

A delayed injection of ⁶⁰Fe into the early solar system, about 1Ma after injection of ²⁶Al, was suggested by Bizzarro et al. (2007) based on Ni and Mg isotopic studies in a suite of chondrites and early formed differentiated meteorites (Bizzarro et al., 2005; Thrane et al., 2006; Bizzarro et al., 2007). They proposed that a WR star is the source of both ⁶⁰Fe and ²⁶Al present in the early solar system with ²⁶Al introduced during the “wind” phase of the star and ⁶⁰Fe from the SN phase a million years later. Possible enrichment of ⁶⁰Fe in the protosolar cloud with contribution from many earlier

generations of SNe have also been proposed (Gounelle & Meibom 2008; Gounelle et al., 2009). This will also lead to decoupling of ^{26}Al and ^{60}Fe records in the early solar system. The results obtained in the present study provide evidence contrary to this scenario. Despite the errors associated with the inferred initial $^{60}\text{Fe}/^{56}\text{Fe}$ and $^{26}\text{Al}/^{27}\text{Al}$ at the time of formation of the chondrules, obtained in this study, one finds a reasonable correlation between them (Fig. 5.6). The expected correlation, if one assumes co-injection of these two SLNs into the early solar system, is also shown in this figure for two assumed SSI $^{60}\text{Fe}/^{56}\text{Fe}$ values, 5×10^{-7} and 1×10^{-6} . The time of formation of the chondrules, relative to CAIs, is also shown in the figure (top axis). The chondrule with highest $^{60}\text{Fe}/^{56}\text{Fe}$ in fact formed within the first million year after

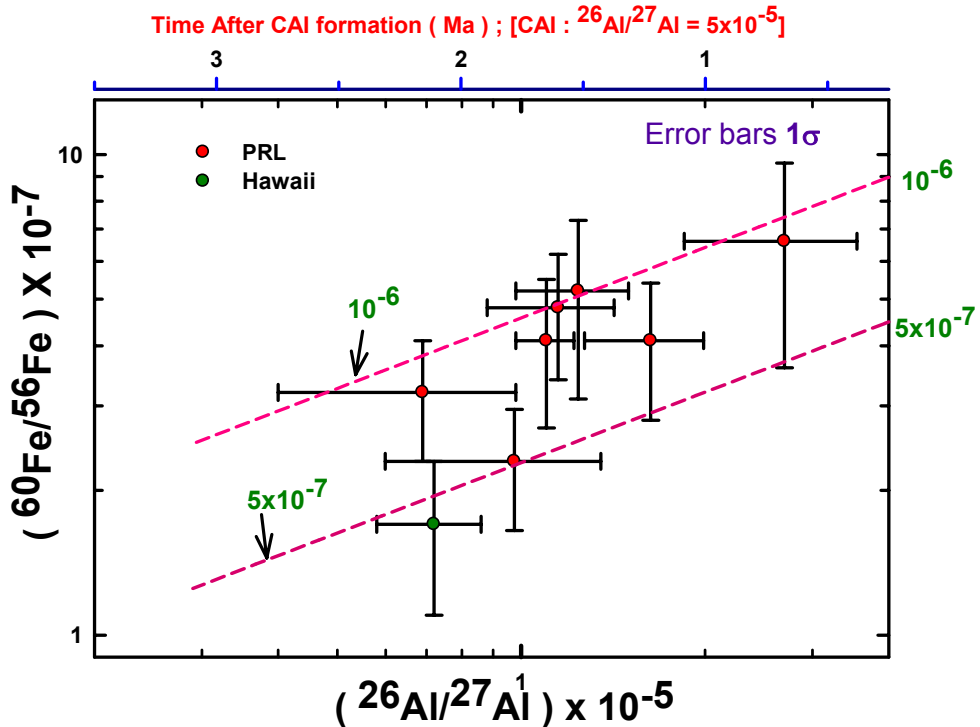


Fig. 5.6 A plot of inferred $[^{60}\text{Fe}/^{56}\text{Fe}]_i$ vs. $[^{26}\text{Al}/^{27}\text{Al}]_i$ in UOC chondrules analyzed in this study. One data point from Tachibana et al. (2007) is also included. The expected correlation if ^{60}Fe and ^{26}Al were co-injected from the same source is shown for two SSI $^{60}\text{Fe}/^{56}\text{Fe}$ values of 10^{-6} and 5×10^{-7} . Time of formation of the chondrules, relative to CAIs is also shown in the top panel

CAI formation. This data set strongly argues for co-injection of ^{26}Al and ^{60}Fe into the solar system. It may be noted here that the results of Bizzarro et al (2007) that

indicated the possibility of a late injection of ^{60}Fe relative to ^{26}Al , has been questioned (e.g., Dauphas et al., 2008) as the results could not be reproduced in experiments conducted by other groups.

In previous studies of refractory hibonite ($\text{CaAl}_{12-2x} \text{Mg}_x \text{Ti}_x \text{O}_{19}$) present within CAIs from CV3 meteorites, Efremovka and Allende, as well as isolated hibonite fragments from CM meteorite, Murchison, a correlation between presence of ^{41}Ca and ^{26}Al was established suggesting their co-injection from a single stellar source (Sahijpal & Goswami 1998; Sahijpal et al., 1998). Studies of ^{26}Al and ^{10}Be records, the later an unique product of energetic particle production, in CM hibonites showed that presence of ^{26}Al and ^{10}Be is decoupled and hence ^{26}Al cannot be a predominant product of energetic particle interactions (Marhas et al., 2002; Goswami et al., 2005). The correlation between ^{26}Al and ^{60}Fe records in chondrules observed in the present study, therefore, suggest that the three SLNs, ^{26}Al , ^{41}Ca and ^{60}Fe are co-genetic and a high mass supernova appears to be the most plausible source of these freshly synthesized nuclides that were co-injected into the protosolar cloud.

5.7 Revision in Half-Life of ^{60}Fe :

A revision of the half-life of ^{60}Fe was proposed very recently (Rugel et al., 2009). The proposed new half-life (2.62 Ma) is longer than the half-life of 1.5 Ma used in this study and needs confirmation as well as formal approval from International forum on particle data. However, this revision will not affect the conclusions regarding the stellar source of ^{60}Fe presented here. In Fig. 5.7 we superpose the expected trend lines for two SSI $^{60}\text{Fe}/^{56}\text{Fe}$ values, considering the proposed new half-life of 2.6Ma for ^{60}Fe , on the same set of data shown in Fig. 5.6. The net effect of adopting the new half-life will yield a slightly lower weighted mean SSI $^{60}\text{Fe}/^{56}\text{Fe}$ value of 5.7×10^{-7} . This value also rules out the possibility of an intermediate AGB star as the source of ^{60}Fe . Thus the conclusion drawn earlier that a high mass supernova is the most probable source of ^{60}Fe and several other SLNs present in the early solar system remains unchanged.

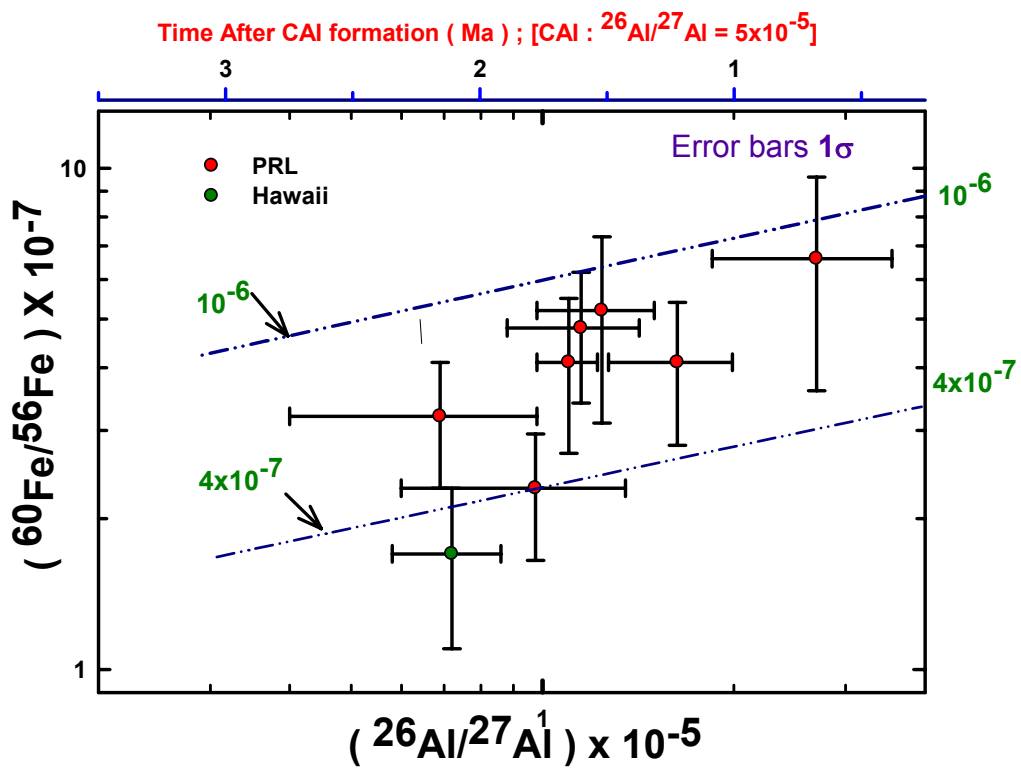


Fig. 5.7 A plot of inferred $[^{60}\text{Fe}/^{56}\text{Fe}]_i$ vs. $[^{26}\text{Al}/^{27}\text{Al}]_i$ in UOC chondrules (as in Fig. 5.6). Trend lines for two values of SSI $^{60}\text{Fe}/^{56}\text{Fe}$ are based on ^{60}Fe half-life of 2.6 Ma.

CHAPTER 6 : SUMMARY AND FUTURE PERSPECTIVE

Fossil records of ^{60}Fe and ^{26}Al have been analyzed in a selected set of chondrules from the three UOCs of low petrologic grade, Semarkona (LL3.0), Lew 86314 (L3.0) and Y-91324 (L3.1), to infer the most plausible solar system initial (SSI) abundance of ^{60}Fe . Analysis of Fe-Ni and Al-Mg isotope systematics using an ion microprobe led to identification of six chondrules from Semarkona and one chondrule from LEW86314 with resolved excess in both ^{60}Ni and ^{26}Mg from in-situ decay of ^{60}Fe and ^{26}Al , respectively, at 2σ level. In another three chondrules resolved excess was found at 1σ level. Additional seven chondrules yielded resolved excess either in ^{60}Ni or in ^{26}Mg .

Data from Al-Mg isotope systematics, particularly the inferred initial $^{26}\text{Al}/^{27}\text{Al}$ of the chondrules, provide their time of formation relative to the CAIs, characterized by the canonical $^{26}\text{Al}/^{27}\text{Al}$ value of 5×10^{-5} . This information coupled with inferred initial $^{60}\text{Fe}/^{56}\text{Fe}$ allows one to estimate the initial $^{60}\text{Fe}/^{56}\text{Fe}$ at the time of CAI formation that can be regarded as the SSI initial $^{60}\text{Fe}/^{56}\text{Fe}$. This is the first such attempt to obtain time of formation of samples analyzed for Fe-Ni isotope systematics, as in all the earlier studies of individual Fe-rich silicate, sulphide or oxide phases, plausible assumption of the time of formation of the analysed phases (objects) has to be made to infer the SSI $^{60}\text{Fe}/^{56}\text{Fe}$. The well-resolved (at 2σ level) data obtained in seven chondrules provided seven independent estimates of SSI $^{60}\text{Fe}/^{56}\text{Fe}$ values that yielded a weighted average value of $(7 \pm 1.8) \times 10^{-7}$. This may be considered as the first robust value for SSI $^{60}\text{Fe}/^{56}\text{Fe}$ reported to date. The value noted above is based on a half-life of 1.5 Ma for ^{60}Fe . A new half-life of 2.6 Ma has been proposed recently for this nuclide; if confirmed, the revised mean value for SSI $^{60}\text{Fe}/^{56}\text{Fe}$ will be $\sim 6 \times 10^{-7}$.

^{60}Fe is an unique product of stellar nucleosynthesis. Production of this highly neutron-rich nuclide is very difficult via energetic particle interactions, both due to lack of suitable targets and extremely low reaction cross section for proton or alpha particle induced reactions with a few naturally occurring neutron-rich target nuclides. Both low-mass as well as high mass stars that evolve to become AGB stars or Supernova or Wolf-Rayet star can produce ^{60}Fe . However, nucleosynthetic yield from AGB stars, even with masses of 4-5 solar masses, can match SSI $^{60}\text{Fe}/^{56}\text{Fe}$ values only up to

5×10^{-7} at best that too with very specific assumptions. Further, ^{60}Fe yield from non-exploding W-R star cannot account for SSI $^{60}\text{Fe}/^{56}\text{Fe} > 10^{-8}$. The possibility of an intermediate mass AGB star being the source of ^{60}Fe present in the early solar system also appears unlikely because of the very low probability of its association with a star forming region. Thus high mass star ending their life as supernova appears to be the most plausible source of ^{60}Fe present in the solar system. Considering model yields of ^{60}Fe from stars of various masses it is found that a SN associated with a 25-30 solar mass star can best explain the SSI $^{60}\text{Fe}/^{56}\text{Fe}$ value obtained in this study.

The possibility of co-injection of both the SLNs, ^{26}Al and ^{60}Fe , from a given stellar source is bolstered by the observed correlation between the initial $^{60}\text{Fe}/^{56}\text{Fe}$ and initial $^{26}\text{Al}/^{27}\text{Al}$ at the time of formation of the analyzed chondrules. This negates a recent suggestion for a late injection of ^{60}Fe , relative to ^{26}Al , from the same stellar source. The co-injection of these nuclides from a high mass supernova is also strengthened by the fact that one can match the SSI $^{60}\text{Fe}/^{56}\text{Fe}$ and SSI $^{26}\text{Al}/^{27}\text{Al}$ using model nucleosynthetic yields from a high mass supernova using the same set of values for a couple of free parameters, such as, the dilution factor and time interval between production of the SLNs at the stellar site and their incorporation into the first solar system solids. In fact, other SLNs present in early solar system, such as ^{41}Ca , ^{107}Pd and ^{182}Hf , may also be co-produced and injected into the protosolar cloud from the same supernova.

One of the issues not addressed specifically in this study is the question of ^{60}Fe as a plausible heat source for early thermal differentiation of planetesimals in the solar system. Given the high solar system abundance of Fe, a SSI $^{60}\text{Fe}/^{56}\text{Fe}$ value of greater than a few times 10^{-7} will make it a significant heat source, particularly after a couple of million years, when the primary heat source ^{26}Al will decay away.

This work represents the first major effort to study both the Al-Mg and Fe-Ni isotope systems to obtain a reliable value for the SSI $^{60}\text{Fe}/^{56}\text{Fe}$. Several significant results as outlined above have been obtained. However, there are quite a few areas that need further studies; these are briefly noted in the following:

1. It will be useful to expand the data base presented in this study and also to make efforts to use new generation ion probes, having order of magnitude better transmission than ims-4f, and multiple ion collectors, to reduce both the

statistical error as well as improve precision of data. This will also allow internal instrument mass fractionation correction by including ^{61}Ni in the analysis routine. If the newly proposed longer half-life of ^{60}Fe is indeed correct, the possibility of studying chondrules that formed much later than those in UOCs (e.g. in carbonaceous chondrite) could also be explored to confirm the results obtained from studies of UOC chondrules.

2. Analysis of bulk samples with both TIMS and MC-ICPMS techniques have so far not resulted in concordant results. Given the superiority of such instrument in precision, compared to ion microprobe, studies of well selected phases free from secondary perturbations will be useful.
3. Even though the revised half life of 2.6 Ma for ^{60}Fe does not affect the conclusion drawn in this paper about the stellar source of this nuclide, its effectiveness as a possible heat source during early evolution of planetesimals need to be evaluated further. A confirmation of the new half-life is also warranted as this will have implication for the model calculations performed for steady state galactic abundance of this nuclide as well as for matching SSI $^{60}\text{Fe}/^{56}\text{Fe}$ with a specific model yields of ^{60}Fe from a stellar source.
4. At present nucleosynthesis yields from low, intermediate and high mass (upto 40 solar mass) stellar sources appear to be better understood. Nonetheless, the problem of ascertaining the reaction cross section for the neutron producing reaction $[^{22}\text{Ne} (\alpha, n)^{25}\text{Mg}]$ still persists. Further, the assumptions related to mixing of freshly synthesized material between various shells, their dilution in the source region itself prior to injection and finally the mass-cut needed in SN models to ensure low ^{53}Mn in the ejected stellar material etc. need further attention. The lack of agreement between different model calculations performed independently by various groups also make a particular choice of a stellar source difficult. A comprehensive understanding of several of the above issues is essential for a better resolution of the problem of a specific stellar source for the SLNs present in the early solar system.

References :

- Alexander CMO, Barber DJ, Hutchison R. 1989. The microstructure of Semarkona and Bishnupur. *Geochimica et Cosmochimica Acta* 53: 3045-57
- Alexander CMOD, Grossman JN, Ebel DS, Ciesla FJ. 2008. The formation conditions of chondrules and chondrites. *Science* 320: 1617-9
- Amelin Y. 2006. The prospect of high-precision Pb isotopic dating of meteorites. *Meteoritics and Planetary Science* 41: 7-17
- Amelin Y, Krot AN, Hutcheon ID, Ulyanov AA. 2002. Lead isotopic ages of chondrules and calcium-aluminum-rich inclusions. *Science* 297: 1678-83
- Arnould M, Goriely S, Meynet G. 2006. The production of short-lived radionuclides by new non-rotating and rotating Wolf-Rayet model stars. *Astronomy and Astrophysics* 453: 653-9
- Arnould M, Paulus G, Meynet G. 1997. Short-lived radionuclide production by non-exploding Wolf-Rayet stars. *Astronomy and Astrophysics* 321: 452-64
- Birck JL, Allegre CJ. 1985. Evidence for the presence of Mn-53 in the early solar system. *Geophysical Research Letters* 12: 745-8
- Birck JL, Allègre CJ. 1988. Manganese-chromium isotope systematics and the development of the early Solar System. *Nature* 331: 579-84
- Birck JL, Lugmair GW. 1988. Nickel and chromium isotopes in Allende inclusions. *Earth & Planetary Science Letters* 90: 131-43
- Bizzarro M, Baker JA, Haack H, Lundgaard KL. 2005. Rapid timescales for accretion and melting of differentiated planetesimals inferred from ^{26}Al - ^{26}Mg chronometry. *Astrophysical Journal* 632

- Bizzarro M, Ulfbeck D, Trinquier A, Thrane K, Connelly JN, Meyer BS. 2007. Evidence for a late supernova injection of ^{60}Fe into the protoplanetary disk. *Science* 316: 1178-81
- Boss AP. 1998. Temperatures in protoplanetary disks. In *Annual Review of Earth and Planetary Sciences*, pp. 53-80
- Boss AP, Ipatov SI, Keiser SA, Myhill EA, Vanhala HAT. 2008. Simultaneous triggered collapse of the presolar dense cloud core and injection of short-lived radioisotopes by a supernova shock wave. *Astrophysical Journal* 686
- Boss AP, Vanhala HAT. 2000. Triggering protostellar collapse, injection, and disk formation. *Space Science Reviews* 92: 13-22
- Brearley AJ. 2005. Nebular versus parent body processing. In *Meteorites, Comets, and Planets*, ed. AM Davis, pp. 247-68. Oxford: Elsevier-Pergamon
- Busso M, Gallino R, Wasserburg GJ. 1999. Nucleosynthesis in asymptotic giant branch stars: Relevance for galactic enrichment and solar system formation. *Annual Review of Astronomy and Astrophysics*: 239-309
- Cameron AGW, Höflich P, Myers PC, Clayton DD. 1995. Massive supernovae, Orion gamma rays, and the formation of the solar system. *Astrophysical Journal* 447
- Cameron AGW, Truran JW. 1977. The supernova trigger for formation of the solar system. *Icarus* 30: 447-61
- catanzaro EJ, murphy TJ, L. GE, R. SW. 1966. Absolute isotopic abundance ratios and atomic weights of magnesium. *Journal Research National Bureau Standard* 70a: 453-8
- Chaussidon M, Gounelle M. 2006. Irradiation processes in the early solar system. In *Meteorites and the early Solar System*, ed. DS Lauretta, HY McSween Jr, pp. 323-39: Arizona university press, Tuscon (Az)
- Chaussidon M, Robert F, McKeegan KD. 2006. Li and B isotopic variations in an Allende CAI: Evidence for the in situ decay of short-lived ^{10}Be and for the

possible presence of the short-lived nuclide ^{7}Be in the early solar system. In *Geochimica et Cosmochimica Acta*, pp. 224-45

Chen JH, Papanastassiou DA, Wasserburg GJ. 2009. A search for nickel isotopic anomalies in iron meteorites and chondrites. *Geochimica et Cosmochimica Acta* 73: 1461-71

Chen JH, Wasserburg GJ. 1990. The isotopic composition of Ag in meteorites and the presence of ^{107}Pd in protoplanets. *Geochimica et Cosmochimica Acta* 54: 1729-43

Choi BG, Huss GR, Wasserburg GJ. 1999. Search for a correlation between ^{60}Fe and ^{26}Al in chondrites. In *Lunar and planetary science conference XXX*, pp. A1862. Houston

Christophe Michel-Levy M. 1968. Un chondre exceptionnel dans la meteorite de vigarano. *Bulletin of Society of France Mineralogy and Crystallography* 91: 212-4

Ciesla F. 2005. Chondrule forming processes: An overview. In *Chondrites and the Protoplanetary Disk*, ed. AN Krot, ERD Scott, B Reipurth, pp. 811-20. San Francisco: Astronomical Society of Pacific

Clayton DD. 1983. *Principle of Stellar Evolution and Nucleosynthesis*. Chicago: University of Chicago press

Connelly JN, Amelin Y, Krot AN, Bizzarro M. 2008. Chronology of the solar system's oldest solids. *Astrophysical Journal* 675

Cook DL, Clayton RN, Wadhwa M, Janney PE, Davis AM. 2008. Nickel isotopic anomalies in troilite from iron meteorites. *Geophysical Research Letters* 35

Cuzzi JN, Alexander CMOD. 2006. Chondrule formation in particle-rich nebular regions at least hundreds of kilometres across. *Nature* 441: 483-5

D'Alessio P, calvet N, Woodlum DS. 2005. Thermal structure of Protoplanetary Disk. In *Chondrites and the Protoplanetary Disk*, ed. AN krot, ERD Scott, B Reipurth, pp. 353-72. Sanfrancisco: Astronomical Society of Pacific

- Dauphas N, Cook DL, Sacarabany A, Fröhlich C, Davis AM, Wadhwa M, Pourmand A, Rauscher T, Gallino R. 2008. Iron 60 evidence for early injection and efficient mixing of stellar debris in the protosolar nebula. *Astrophysical Journal* 686: 560-9
- Davis AM, Alexander CM, O'D, Nagahara H, Richter FM. 2005. Evaporation and condensation during CAI and chondrule formation. In *Astronomical Society of Pacific*, ed. AN Krot, ERD Scott, B Reipurth, pp. 432-55. San Francisco
- Desch SJ, Ciesla FJ, Hood LL, Nakamoto T. 2005. Heating of chondritic materials in solar nebula shocks. In *Chondrites and the Protoplanetary Disk*, ed. AN krot, ERD Scott, B Reipurth, pp. 849-72. Sanfrancisco: Astronomical society of pacific
- Desch SJ, Connolly HC. 2002. A model of the thermal processing of particles in solar nebula shocks: Application to the cooling rates of chondrules. *Meteoritics and Planetary Science* 37: 183-207
- Duprat J, Tatischeff V. 2007. Energetic constraints on in situ production of short-lived radionuclei n in the early solar system. *Astrophysical Journal* 671
- Fitoussi C, Duprat J, Tatischeff V, Kiener J, Naulin F, Raisbeck G, Assuncao M, Bourgeois C, Chabot M, Coc A, Engrand C, Gounelle M, Hammache F, Lefebvre A, Porquet MG, Scarpaci JA, De Saraville N, Thibaud JP, Yiou F. 2008. Measurement of the $^{24}\text{Mg}(3\text{He},\text{p})^{26}\text{Al}$ cross section: Implication for Al26 production in the early solar system. *Physical Review C - Nuclear Physics* 78
- Galy A, Young ED, Ash RD, O'Nions RK. 2000. The formation of chondrules at high gas pressures in the solar nebula. *Science* 290: 1751-3
- Goswami JN, Marhas KK, Chaussidon M, Gounelle M, Meyer BS. 2005. Origin of Short-lived Radionuclides in the Early Solar System. In *Chondrites and the Protoplanetary Disk*, ed. AN Krot, ERD Scott, B Reipurth, pp. 485-514. San Francisco: Astronomical society of Pacific

- Goswami JN, Marhas KK, Sahijpal S. 2001. Did solar energetic particles produce the short-lived nuclides present in the early solar system? *Astrophysical Journal* 549: 1151-9
- Gounelle M, Chaussidon M, Montmerle T. 2007. Irradiation in the early solar system and the origin of short-lived radionuclides. *Comptes Rendus - Geoscience* 339: 885-94
- Gounelle M, Meibom A. 2008. The origin of short-lived radionuclides and the astrophysical environment of solar system formation. *Astrophysical Journal* 680: 781-92
- Gounelle M, Meibom A, Hennebelle P, Inutsuka SI. 2009. Supernova propagation and cloud enrichment: A new model for the origin of ^{60}Fe in the early solar system. *Astrophysical Journal* 694
- Grossman EL. 1980. Refractory inclusions in the Allende meteorite. *Annual Review of Earth and Planetary Sciences* 8: 559-608
- Grossman JN, Brearley AJ. 2005. The onset of metamorphism in ordinary and carbonaceous chondrites. *Meteoritics and Planetary Science* 40: 87-122
- Grossman L. 1972. Condensation in the primitive solar nebula. *Geochimica et Cosmochimica Acta* 36: 597-619
- Guan Y, Huss GR, Leshin LA. 2007. ^{60}Fe - ^{60}Ni and ^{53}Mn - ^{53}Cr isotopic systems in sulfides from unequilibrated enstatite chondrites. *Geochimica et Cosmochimica Acta* 71: 4082-91
- Herwig F. 2005. Evolution of asymptotic giant branch stars. In *Annual Review of Astronomy and Astrophysics*, pp. 435-79
- Hewins RH, Connolly Jr HC, Lofgren GE, Libourel G. 2005. Experimental constraints on chondrule formation. In *Chondrites and Protoplanetary Disk*, ed. AN Krot, ERD Scott, B Reipurth, pp. 286-316. San Francisco: Astronomical Society of the Pacific

Hood LL, Ciesla FJ, Weidenschilling SJ. 2005. Chondrule formation in planetesimal bow shocks: Heating and cooling rates. In *Chondrites and the Protoplanetary Disk*, ed. AN Krot, ERD Scott, B Reipurth, pp. 873-82. San Francisco: Astronomical Society of Pacific

Hudson GB, kennedy BM, Podosek FA, Hohenberg CM. 1988. *The early abundance of Pu-244 as inferred from St. Severin chondrites*. Presented at Lunar and Planetary Science conference Houston

Huss GR, MacPherson GJ, Wasserburg GJ, Russell SS, Srinivasan G. 2001. Aluminum-26 in calcium-aluminum-rich inclusions and chondrules from unequilibrated ordinary chondrites. *Meteoritics and Planetary Science* 36: 975-97

Huss GR, Meyer BS, Srinivasan G, Goswami JN, Sahijpal S. 2009. Stellar sources of the short-lived radionuclides in the early solar system. *Geochimica et Cosmochimica Acta* 73: 4922-45

Hutcheon ID, Marhas KK, Krot AN, Goswami JN, Jones RH. 2009. ^{26}Al in plagioclase-rich chondrules in carbonaceous chondrites: Evidence for an extended duration of chondrule formation. *Geochimica et Cosmochimica Acta* 73: 5080-99

Hutchison R. 2004. *Meteorites: A Petrologic, Chemical and Isotopic Synthesis*

Cambridge University press. 506 pp.

Jacobsen B. 2005. The Birth of the Solar System in a Molecular Cloud: Evidence from the Isotopic Pattern of Short-Lived Nuclides in the Early Solar System. In *Chondrites and the protoplanetary disk*, ed. AN Krot, ERD Scott, r Bo, pp. 548-56

Jeffery PM, Reynolds JH. 1961. Origin of excess ^{136}Xe in stone meteorites. *Journal of Geophysical Research* 66: 2

- Kastner JH, Myers PC. 1994. An observational estimate of the probability of encounters between mass-losing evolved stars and molecular clouds. *Astrophysical Journal* 421: 605-14
- Kita NT, Huss GR, Tachibana S, Amelin Y, Nyquist LE, Hutcheon ID. 2005. Constraints on the origin of chondrules and CAIs from short-lived and long-lived radionuclides. *Chondrites and the Protoplanetary Disk* 341: 558-87
- Kita NT, Nagahara H, Togashi S, Morishita Y. 2000. A short duration of chondrule formation in the solar nebula: Evidence from ^{26}Al in Semarkona ferromagnesian chondrules. *Geochimica et Cosmochimica Acta* 64: 3913-22
- Kita NT, Togashi S, Morishita T, Terashima S, yurimoto H. 1998. Search for ^{60}Ni excesses in MET-78008 Ureilite : An ion microprobe study. *Antartic meteorite research* 11: 103-21
- Kleine T, Munker C, Mezger K, Palme H. 2002. Rapid accretion and early core formation on asteroids and the terrestrial planets from Hf-W chronometry. *Nature* 418: 952-5
- Krot AN, Amelin Y, Bland P, Ciesla FJ, Connelly J, Davis AM, Huss GR, Hutcheon ID, Makide K, Nagashima K, Nyquist LE, Russell SS, Scott ERD, Thrane K, Yurimoto H, Yin QZ. 2009. Origin and chronology of chondritic components: A review. *Geochimica et Cosmochimica Acta* 73: 4963-97
- Krot AN, Yurimoto H, McKeegan KD, Leshin L, Chaussidon M, Libourel G, Yoshitake M, Huss GR, Guan Y, Zanda B. 2006. Oxygen isotopic compositions of chondrules: Implications for evolution of oxygen isotopic reservoirs in the inner solar nebula. *Chemie der Erde - Geochemistry* 66: 249-76
- Kurahashi E, Kita NT, Nagahara H, Morishita Y. 2008. ^{26}Al - ^{26}Mg systematics of chondrules in a primitive CO chondrite. *Geochimica et Cosmochimica Acta* 72: 3865-82
- Lattanzio JC. 1991. Stellar evolutionary models from the zero-age main sequence to the first thermal pulse. *Astrophysical Journal, Supplement Series* 76: 215-357

- Lee T, Papanastassiou DA, Wasserburg GJ. 1976. Demonstration of ^{26}Mg excess in Allende and evidence for ^{26}Al *Geophysical Research Letters* 3: 109-12
- Lee T, papanastassiou DA, Wasserburg GJ. 1977. Aluminium-26 in the early solar system- Fossil or Fule. *astrophysical Journal* 211: 107-10
- Lee T, Shu FH, Shang H, Glassgold AE, Rehm KE. 1998. Protostellar cosmic rays and extinct radioactivities in meteorites. *Astrophysical Journal* 506: 898-912
- Leya I, Halliday AN, Wieler R. 2003. The Predictable Collateral Consequences of Nucleosynthesis by Spallation Reactions in The Early Solar System. *Astrophysical Journal* 594: 605-16
- Limongi M, Chieffi A. 2006. The nucleosynthesis of ^{26}Al and ^{60}Fe in solar metallicity stars extending in mass from 11 to 120 M_\odot The hydrostatic and explosive contributions. *Astrophysical Journal* 647: 483-500
- Lugmair GW, Shimamura T, Lewis RS, Anders E. 1983. Samarium-146 in the early solar system: Evidence from neodymium in the allende meteorite. *Science* 222: 1015-8
- Lugmair GW, Shukolyukov A. 1998. Early solar system timescales according to ^{53}Mn - ^{53}Cr systematics. *Geochimica et Cosmochimica Acta* 62: 2863-86
- MacPherson GJ, Simon SB, Davis AM, Grossman L, Krot AN. 2005. Calcium-aluminum-rich inclusions: Major unanswered questions. In *Chondrites and ProtoPlanetary Disk*, ed. AN Krot, ERD Scott, B Reipurth, pp. 225-50. San Francisco
- Marhas KK, Goswami JN, Davis AM. 2002. Short-lived nuclides in hibonite grains from Murchison: Evidence for solar system evolution. *Science* 298: 2182-5
- McKeegan KD, Chaussidon M, Robert F. 2000. Incorporation of short-lived ^{10}Be in a calcium-aluminum-rich inclusion from the Allende meteorite. *Science* 289: 1334-7

Meyer BS. 2005. Synthesis of Short-lived Radioactivities in a massive star. In *Chondrites and the Protoplanetary Disk*, ed. AN Krot, ERD Scott, B Reipurth, pp. 515-26. San Francisco: Astronomical society of Pacific

Mostefaoui S, Lugmair GW, Hoppe P. 2005. ^{60}Fe : A heat source for planetary differentiation from a nearby supernova explosion. *Astrophysical Journal* 625: 271-7

Moynier F, Qing-Zhu YIN, Jacobsen B. 2007. Dating the first stage of planet formation. *Astrophysical Journal* 671

Niederer FR, Papanastassiou DA. 1984. Ca isotopes in refractory inclusions. *Geochimica et Cosmochimica Acta* 48: 1279-93

Niederer FR, Papanastassiou DA, Wasserburg GJ. 1981. The isotopic composition of titanium in the Allende and Leoville meteorites. *Geochimica et Cosmochimica Acta* 45: 1017-31

Nyquist LE, Kleine T, Shih C-Y, Reese Y. 2009a. The distribution of short-lived radioisotopes in the early solar system and the chronology of asteroid accretion, differentiation, and secondary mineralization. *Geochimica et Cosmochimica Acta* 73: 5115-36

Nyquist LE, Kleine T, Shih CY, Reese YD. 2009b. The distribution of short-lived radioisotopes in the early solar system and the chronology of asteroid accretion, differentiation, and secondary mineralization. *Geochimica et Cosmochimica Acta* 73: 5115-36

Ouellette N, Desch SJ, Bizzarro M, Boss AP, Ciesla F, Meyer B. 2009. Injection mechanisms of short-lived radionuclides and their homogenization. *Geochimica et Cosmochimica Acta* 73: 4946-62

Quitté G, Meier M, Latkoczy C, Halliday AN, Günther D. 2006. Nickel isotopes in iron meteorites-nucleosynthetic anomalies in sulphides with no effects in metals and no trace of ^{60}Fe . *Earth and Planetary Science Letters* 242: 16-25

- Rauscher T, Heger A, Huffman RD, Woosley SE. 2002. Nucleosynthesis in massive stars with improved nuclear and stellar physics. *Astrophysical Journal* 576: 323-48
- Reeves H. 1994. On the origin of the light elements ($Z < 6$). *Reviews of Modern Physics* 66: 193-216
- Regelous M, Elliott T, Coath CD. 2008. Nickel isotope heterogeneity in the early Solar System. *Earth and Planetary Science Letters* 272: 330-8
- Reynolds JH. 1960. Determination of the age of the elements. *Physical Review Letters* 4: 8-10
- Rudraswami NG, Goswami JN. 2007. ^{26}Al in chondrules from unequilibrated L chondrites: Onset and duration of chondrule formation in the early solar system. *Earth and Planetary Science Letters* 257: 231-44
- Rudraswami NG, Goswami JN, Chattopadhyay B, Sengupta SK, Thapliyal AP. 2008. ^{26}Al records in chondrules from unequilibrated ordinary chondrites: II. Duration of chondrule formation and parent body thermal metamorphism. *Earth and Planetary Science Letters* 274: 93-102
- Rugel G, Faestermann T, Knie K, Korschinek G, Poutivtsev M, Schumann D, Kivel N, Gunther-Leopold I, Weinreich R, Wohlmuther M. 2009. New measurement of the Fe60 half-life. *Physical Review Letters* 103
- Sahijpal S, Goswami JN. 1998. Refractory phases in primitive meteorites devoid of ^{26}Al and ^{41}Ca : representative samples of first solar system solids? *Astrophysical Journal* 509
- Sahijpal S, Goswami JN, Davis AM, Grossman L, Lewis RS. 1998. A stellar origin for the short-lived nuclides in the early Solar System. *Nature* 391: 559-61
- Schonbachler M, Rehkamp M, Halliday AN, Lee D-C, Bourot-Denise M, Zanda B, Hattendorf B, Gunther D. 2002. Niobium-zirconium chronometry and early solar system development. *Science* 295: 1705-8

- Scott ERD, Krot AN. 2005a. Chondrites and their components. In *Meteorites, Comets, and Planets*, ed. AM Davis, pp. 143-200. Oxford: Elsevier-Pergamon
- Scott ERD, Krot AN. 2005b. Chondritic meteorites and the high-temperature nebular origins of their components. In *Chondrites and the Protoplanetary Disk*, ed. AN Krot, ERD Scott, B Reipurth, pp. 15-53. San Francisco: Astronomical Society of Pacific
- Shu FH, Shang H, Glassgold AE, Lee T. 1997. X-rays and fluctuating x-winds from protostars. *Science* 277: 1475-9
- Shu FH, Shang H, Lee T. 1996. Toward an astrophysical theory of chondrites. *Science* 271: 1545-52
- Shukolyukov A, Lugmair G. 1993a. ^{60}Fe in eucrites. *Earth & Planetary Science Letters* 119: 159-66
- Shukolyukov A, Lugmair GW. 1993b. Live iron-60 in the early solar system. *Science* 259: 1138-42
- Srinivasan G, Sahijpal S, Ulyanov AA, Goswami JN. 1996. Ion microprobe studies of Efremovka CAIs: II. Potassium isotope composition and ^{41}Ca in the early Solar System. *Geochimica et Cosmochimica Acta* 60: 1823-35
- Srinivasan G, Ulyanov AA, Goswami JN. 1994. ^{41}Ca in the early solar system. *Astrophysical Journal* 431
- Straniero O, Chieffi A, Limongi M, Busso M, Gallino R, Arlandini C. 1997. Evolution and nucleosynthesis in low-mass asymptotic giant branch stars. I. Formation of population I carbon stars. *Astrophysical Journal* 478: 332-9
- Sugiura N, Miyazaki A, Yin Q-Z. 2006. Heterogeneous distribution of ^{60}Fe in the early solar nebula: Achondrite evidence. *Earth, Planets and Space* 58: 1079-86
- Tachibana S, Huss GR. 2003. The initial abundance of ^{60}Fe in the solar system. *Astrophysical Journal* 588

- Tachibana S, Huss GR. 2005. Sulfur isotope composition of putative primary troilite in chondrules from Bishunpur and Semarkona. *Geochimica et Cosmochimica Acta* 69: 3075-97
- Tachibana S, Huss GR, Kita NT, Shimoda G, Morishita Y. 2006. ^{60}Fe in chondrites: Debris from a nearby supernova in the early solar system? *Astrophysical Journal* 639
- Takigawa A, Miki J, Tachibana S, Huss GR, Tominaga N, Umeda H, Nomoto K. 2008. Injection of short-lived radionuclides into the early solar system from a faint supernova with mixing fallback. *Astrophysical Journal* 688: 1382-7
- Thrane K, Bizzarro M, Baker JA. 2006. Extremely brief formation interval for refractory inclusions and uniform distribution of ^{26}Al in the early solar system. *Astrophysical Journal* 646
- Timmes FX, Woosley SE, Hartmann DH, Hoffman RD, Weaver TA, Matteucci F. 1995. ^{26}Al and ^{60}Fe from supernova explosions. *Astrophysical Journal* 449: 204-10
- Trigo-Rodríguez JM, García-Hernández DA, Lugardo M, Karakas AI, Raai M, Lario PG, Manchado A. 2009. The role of massive AGB star in the early Solar System composition. *meteorit. Planet. Sci.* 44: 627-41
- Trinquier A, Birck JL, Allègre CJ, Göpel C, Ulfbeck D. 2008. 53Mn-53Cr systematics of the early Solar System revisited. *Geochimica et Cosmochimica Acta* 72: 5146-63
- Villeneuve J, Chaussidon M, Libourel G. 2009. Homogeneous distribution of ^{26}Al in the solar system from the mg isotopic composition of chondrules. *Science* 325: 985-8
- Volkening J, Papanastassiou DA. 1989. Iron isotope anomalies. *Astrophysical Journal* 347: 43-6
- Volkening J, Papanastassiou DA. 1990. Zinc isotope anomalies. *Astrophysical Journal* 358

- Wasserburg GJ, Busso M, Gallino R. 1996. Abundances of actinides and short-lived nonactinides in the interstellar medium: Diverse supernova sources for the r-processes. *Astrophysical Journal* 466
- Wasserburg GJ, Busso M, Gallino R, Nollett KM. 2006a. Short-lived Nuclei in the early Solar System : Possible AGB sources. *Nuclear Physics A* 777: 5-69
- Wasserburg GJ, Busso M, Gallino R, Nollett KM. 2006b. Short-lived nuclei in the early Solar System: Possible AGB sources. *Nuclear Physics A* 777: 5-69
- Woosley SE, Heger A. 2007. Nucleosynthesis and remnants in massive stars of solar metallicity. *Physics Reports* 442: 269-83
- Woosley SE, Heger A, Weaver TA. 2002. The evolution and explosion of massive stars. *Reviews of Modern Physics* 74: 1015-71
- Woosley SE, Weaver TA. 1995. The evolution and explosion of massive stars. II. Explosive hydrodynamics and nucleosynthesis. *Astrophysical Journal, Supplement Series* 101: 181-235
- Yin Q, Jacobsen SB, Yamashita K, Blichert-Toft J, Telouk P, Albarede F. 2002. A short timescale for terrestrial planet formation from Hf-W chronometry of meteorites. *Nature* 418: 949-52
- Young ED, Simon JI, Galy A, Russell SS, Tonui E, Lovera O. 2005. Supra-canonical $^{26}\text{Al}/^{27}\text{Al}$ and the residence time of CAIs in the solar protoplanetary disk. *Science* 308: 223-7